FLOW AND TRANSPORT IN FRACTURED GEOTHERMAL RESERVOIRS ON DIFFERENT SCALES: LINKING EXPERIMENTS AND NUMERICAL MODELS

Zur Erlangung des akademischen Grades eines

DOKTORS DER NATURWISSENSCHAFTEN (Dr. rer. nat.)

von der KIT-Fakultät für

Bauingenieur-, Geo- und Umweltwissenschaften

des Karlsruher Instituts für Technologie (KIT)

genehmigte

DISSERTATION

von

M.Sc. Robert Wolfgang Egert

aus Groß-Umstadt

Tag der mündlichen Prüfung:

23. Februar 2021

Referent: Prof. Dr. Thomas Kohl

Korreferent: Prof. Dr. Florian Amann

Karlsruhe 2021

ABSTRACT

Geothermal energy represents an important renewable energy source for the future to meet people's basic needs for heat and electricity as well as reduce dependence on fossil fuels such as oil and coal. The International Energy Agency estimates that 3.5 % of the world's energy supply can be derived from geothermal energy by 2050. The advantages of geothermal energy include the good on-demand controllability as well as the availability anywhere in the world with a small land footprint. Furthermore, geothermal energy is one of the few renewable energies that is completely capable of supplying base load and is therefore independent of strongly fluctuating environmental conditions, such as wind speed or solar radiation. The main challenge related to geothermal energy is the development of low-enthalpy reservoirs located at depths of a few kilometers. The Enhanced Geothermal System (EGS) technology is one way to do so, making low-permeability rock layers of a reservoir economically viable. EGS uses hydraulic stimulation to widen existing natural fracture systems and create new fractures, allowing effective heat exchange between the fractured reservoir rock and circulating fluids. So far, only a few pilot plants exist, such as the EGS in Soultz-sous-Forêts, France. The disadvantage of such technology is the fact that the resulting fractures represent only a very limited part of the reservoir volume and so all the natural and induced processes involved in the fluid circulation take place in a very limited space. Thus, a thorough understanding of the highly localized physical processes and interactions is a key factor for the successful, environmentally friendly, and safe operation of EGS.

Particular attention must be paid to the mutual interactions between the fracture and the circulating fluid as well as the associated transport of heat and solutes. The fracture void is often simplified as the distance between two parallel plates. In reality, however, the connections between two boreholes consist of a small-scale network of individual fractures, which in turn have a highly variable internal pore volume.

This thesis is a contribution to an improved understanding of the formation and geometric nature of preferential fluid pathways in fractured reservoirs and the associated transport processes. The main objective of the individual studies is to link experimental investigations with numerical models in order to identify and quantify the relevant partially scale-dependent physical processes in fractures.

In the **first two studies** (Chapters 4 and 5), a variety of stochastically unique granite-like fracture geometries are created. Numerical modeling is used to quantify preferential fluid pathways and their characteristics in the fracture space void under typical geothermal flow conditions employing the complex Navier-Stokes equations.

The objective of the **first study** is to quantify the spatial differences between three-dimensional and simplified two-dimensional fracture models. A compar-

ison between equivalent modeling using the Navier-Stokes equations and the local cubic law allows a prediction regarding the validity of the simplifications. Depending on the direction of flow and shearing as well as the applied boundary pressure, channels form in all fractures that comprise a large fraction of the volume flow rate. In the remaining fracture void space only minor amounts of fluid transport are observed. Within these channels, both flow laws indicate satisfactory agreement for laminar and turbulent flows (with Reynolds numbers above 1). Outside of channels, the two-dimensional simplification yields a significant overestimation of the expected flow rate, regardless of the flow regime. The **second study** quantifies the individual channels within the three-dimensional fracture concerning geometry as well as transport properties. The results reveal a strong anisotropy with respect to flow and shearing direction. Although a perpendicular orientation of flow and shearing results in a significantly improved flow field, the well-formed and straight channels have limited contact area with the surrounding rock, hindering efficient heat exchange. The situation is different when shearing and flow are aligned in parallel. Here, the channels are considerably less pronounced and also have a strongly prolonged absolute flow path and associated higher contact area.

The **third study** (Chapter 6) comprises the combination of triaxial experiments, performed on two different sandstones analogues on increasing temperature and pressure conditions, with numerical models. The objective is to predict the hydraulic and mechanical rock properties of a potential reservoir rock. The results indicate poroelastic compaction of the rock and subsequent nonlinear deformation, which can both be predicted with numerical models. The Drucker-Prager criterion allows the evaluation of the critical stress for the onset of shearing considering the three principal stresses. The study demonstrates that although small-scale changes, such as in mineralogical composition, affect the material properties of the rock, numerical and analytical models can still describe its behavior.

In the **fourth and fifth studies** (Chapter 7 and 8), the small-scale knowledge gained, and further field investigations are used to develop a model of the large-scale flow regime in the fractured Soultz-sous-Forêts reservoir. In the **fourth study**, a structural model of the Soultz reservoir is developed and the flow regime along fractures between individual wells is determined using numerical models. By linking this model to experimental data from several circulation as well as tracer tests, the flow regime can be quantified even in regions of the reservoir distant from the wellbores. Besides, a geological structure can be identified that hydraulically separates the GPK3 and GPK4 wells but establishes a fault-parallel connection to the flow regime of the Upper Rhine Graben. In the **fifth study**, the sensitivity of the production temperature with respect to different operational framework conditions (injection temperature and flow rates) is investigated using the previously developed hydraulic model.

KURZFASSUNG

Die Erdwärme stellt eine wichtige erneuerbare Energiequelle der Zukunft dar, um den Grundbedarf der Menschen an Wärme und Strom zu decken und die Abhängigkeit von fossilen Brennstoffen wie Erdöl und Kohle zu verringern. Die Internationale Energiebehörde schätzt, dass bis zum Jahr 2050 3,5 % der weltweiten Energieversorgung durch Geothermie erfolgen können. Die Vorteile der Geothermie liegen dabei in der guten bedarfsabhängigen Regulierbarkeit sowie der uneingeschränkten weltweiten Verfügbarkeit bei gleichzeitig geringem Flächenbedarf. Darüber hinaus ist die Geothermie als eine der wenigen erneuerbaren Energien vollständig grundlastfähig und damit unabhängig von stark wechselnden Umwelteinflüssen, wie Windstärke oder Sonneneinstrahlung. Die größte Herausforderung bei der Geothermie liegt in der Erschließung von Niederenthalpie-Lagerstätten, die in Tiefen von einigen Kilometern liegen. Eine Möglichkeit hierzu stellt die Technologie des Enhanced Geothermal Systems (EGS) dar, die geringdurchlässige Gesteinsschichten eines Reservoirs wirtschaftlich nutzbar macht. Bei EGS werden durch hydraulische Stimulation bestehende natürliche Kluftsysteme erweitert und neue Klüfte geschaffen und so ein effektiver Wärmeaustausch zwischen dem geklüfteten Reservoirgestein und zirkulierenden Fluiden ermöglicht. Bisher gibt es allerdings nur wenige Pilotanlagen, wie z.B. in Soultz-sous-Forêts, Frankreich. Der Nachteil dieser Technologie ist, dass die so entstandenen Klüfte nur einen sehr kleinen Teil des Reservoirvolumens darstellen und sich alle an der Fluidzirkulation beteiligten natürlichen und induzierten Prozesse auf engstem Raum abspielen. Das grundlegende Verständnis der hochlokalisierten physikalischen Prozesse und Wechselwirkungen stellt somit den Schlüsselfaktor für einen erfolgreichen, umweltverträglichen und sicheren Betrieb von EGS dar.

Ein besonderes Augenmerk muss auf die gegenseitigen Wechselwirkungen zwischen der Kluft und dem zirkulierenden Fluid sowie dem damit verbundenen Transport von Wärme und gelösten Stoffen gelegt werden. Die Kluftöffnung wird oft vereinfacht als der Abstand zwischen zwei parallelen Platten dargestellt. In Wirklichkeit bestehen die Verbindungen zwischen zwei Bohrungen jedoch aus einem kleinräumigen Netzwerk einzelner Klüfte, die wiederum ein stark veränderliches inneres Porenvolumen aufweisen.

Die vorliegende Arbeit trägt zu einem besseren Verständnis der Entstehung und geometrischen Beschaffenheit von bevorzugten Fluidwegsamkeiten in geklüfteten Reservoiren sowie der damit verbundenen Transportprozesse bei. Das übergeordnete Ziel der einzelnen Studien ist eine Verknüpfung experimenteller Untersuchungen mit numerischen Modellen, um die relevanten, teilweise skalenabhängigen physikalischen Prozesse in Klüften zu identifizieren und quantifizieren.

In den ersten **beiden Studien** (Kapitel 4 und 5) werden eine Vielzahl von stochastisch einzigartigen granitähnlichen Kluftgeometrien erstellt. Anschließend

werden numerische Modelle entwickelt, um die präferentiellen Fluidpfade und deren Eigenschaften im Klufhohlraum unter geothermie-typischen Strömungsbedingungen und unter Verwendung der komplexen Navier-Stokes-Gleichungen zu quantifizieren.

Das Ziel der **ersten Studie** ist die Quantifizierung von räumlichen Unterschieden zwischen den dreidimensionalen und den vereinfachten zweidimensionalen Kluftmodellen. Ein Vergleich zwischen äquivalenten Modellierungen mittels der Navier-Stokes-Gleichungen und dem lokalen kubischen Gesetz erlaubt eine Vorhersage über die Gültigkeit dieser Vereinfachungen. In Abhängigkeit von Fließ- und Scherrichtung sowie dem angelegten Druckgradienten bilden sich in allen Klüften Kanäle aus, die einen großen Teil des Volumenstroms umfassen, während im Rest der Kluft nur geringe Anteile an Fluidbewegung zu beobachten sind. Innerhalb dieser Kanäle zeigen beide Fließgesetze eine gute Übereinstimmung sowohl für rein laminare als auch turbulente Strömungen (mit Reynolds-Zahlen deutlich über 1). Außerhalb von Kanälen ergibt sich unabhängig vom Fließregime für die zweidimensionale Vereinfachung eine deutliche Überschätzung des zu erwartenden Volumenstroms. In der **zweiten Studie** werden die einzelnen Kanäle innerhalb der dreidimensionalen Kluft hinsichtlich ihrer Geometrie sowie Transporteigenschaften quantifiziert. Die Ergebnisse zeigen eine starke Anisotropie hinsichtlich der Fließ- und Scherrichtung. Obwohl eine senkrechte Ausrichtung von Strömung und Scherung zu einem deutlich verbesserten Durchfluss führt, haben die gut ausgebildeten und geraden Kanäle nur eine begrenzte Kontaktfläche mit dem umgebenden Gestein und behindern somit einen effizienten Wärmeaustausch. Anders ist dies bei einer parallelen Ausrichtung von Scherung und Strömung. In diesem Fall sind die Kanäle deutlich weniger ausgeprägt und haben zudem einen stark verlängerten absoluten Fließweg und damit verbundene höhere Kontaktfläche.

Die **dritte Studie** (Kapitel 6) umfasst die Verknüpfung von Triaxialexperimenten, durchgeführt an zwei Sandsteinenderivaten mit steigenden Temperatur- und Druckbedingungen, mit numerischen Modellen. Ziel ist eine Vorhersage der hydraulischen und mechanischen Gesteinseigenschaften eines potentiellen Reservoirgesteins. Die Ergebnisse zeigen eine poroelastische Kompaktion des Gesteins sowie anschließende nichtlineare Deformation, welche beide mit numerischen Modellen vorhergesagt werden können. Das Drucker-Prager-Kriterium ermöglicht die Bewertung der kritischen Scherspannung unter Berücksichtigung der drei Hauptspannungen. Die Studie zeigt, dass kleinstskalige Veränderungen, wie die mineralogische Zusammensetzung, zwar die Materialeigenschaften des Gesteins beeinflussen, numerische und analytische Modelle dessen Verhalten dennoch beschreiben können.

In der **vierten und fünften Studie** (Kapitel 7 und 8) werden die kleinskalig gewonnen Erkenntnisse sowie weiterführende Felduntersuchungen dazu genutzt, um ein Modell des großräumigen Strömungsregimes im geklüfteten Reservoir von Soultz-sous-Forêts zu entwickeln. In der **vierten Studie** wird ein Strukturmodell des Soultz-Reservoirs entwickelt und das Strömungsregime entlang von Klüften zwischen den einzelnen Bohrungen mittels numerischer Modelle bestimmt. Durch die Verknüpfung mit den experimentellen Daten mehrerer Zirkulations- sowie Tracerversuche kann das Strömungsregime in bohrlochfer-

nen Bereichen des Reservoirs quantifiziert werden. Darüber hinaus kann eine geologische Struktur identifiziert werden, die die Bohrungen GPK3 und GPK4 zwar hydraulisch separiert, allerdings störungsparallel eine Anbindung an das Fließregime des Oberrheingrabens herstellt. In der **fünften Studie** wird auf Grundlage des zuvor entwickelten hydraulischen Modells die Sensitivität der Produktionstemperatur hinsichtlich verschiedener operativer Rahmenbedingungen (Injektionstemperatur und Fließraten) untersucht.

CONTENTS

1

INTRODUCTION

Human activities cause climate change forcing global warming of the earth. According to the Intergovernmental Panel on Climate Change (IPCC), by 2017 the annual mean temperature has already risen by over 1 °C compared to the pre-industrial age. Without change, an increase of more than 3 °C is expected by the end of the century, which will lead to extreme weather events and climate conditions such as severe heat waves or storms (Tollefson, 2018). The global warming is considered to be a result of the emission of greenhouse gases and its accumulation in the earth's atmosphere. The anthropogenic emission of carbon dioxide is identified as the main cause of environmental pollution. It is therefore generally accepted that its emission has to be reduced or completely eliminated. The German government has outlined framework conditions for nationwide greenhouse gas-neutral energy production from 2050 onwards (BMUB, 2016). The IPCC has developed different scenarios of how the climate and temperature will change if no more CO_2 is emitted into the atmosphere from 2055 onwards to limit the maximum temperature increase to 1.5 °C (Figure 1.1, IPCC, 2018). What they all have in common is that the burning of fossil fuels must be stopped and the change to clima-neutral renewable energy is indispensable.

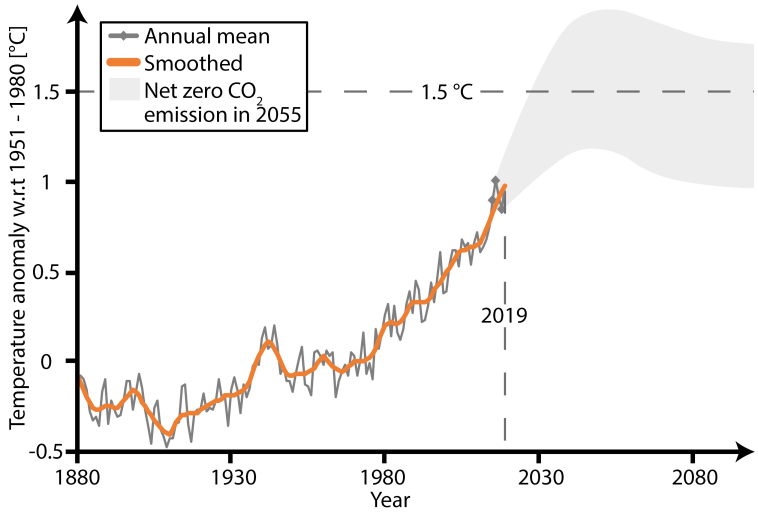

Figure 1.1: Observed annual global mean surface temperature (GMST) up to 2019 after GISTEMP Team (2020) with the likely rise temperature until 2100 when CO_2 emissions reach net zero in 2055 while net non-CO_2 radiative forcing is already reduced after 2030 (IPCC, 2018)

In order to cover the worldwide energy demand, a mix of different renewable energies is necessary. Photovoltaics and wind turbines can cover a large peak load depending on environmental influences (solar radiation, wind speed, etc.), while hydropower and geothermal energy can also cover base load demands. A great advantage of geothermal energy is the ability to fully control the processes involved and the decentralized use through the worldwide availability of terrestrial heat while requiring less space. This makes it possible to place geothermal power plants close to end consumers, such as cities and industries.

In the last ten years, the global installed capacity of geothermal power plants has increased by about 30 % to a total capacity of 12 700 MWe in 2017. An annual electric production of 86 TW h is reported for 2017 (IEA, 2019), which is still far from the plans for 2050 (1000 TW h yr^{-1}, IEA, 2017). In order to still reach the set targets, the annual increase in installed capacity must be significantly raised. However, geothermal energy must become much more attractive for investors by minimizing initial investments and geological risks. On the one hand, in a few countries with preferred geothermal conditions and low geological risks (e.g. Iceland, El Salvador or the Philippines), a large part of the power generated is already covered by geothermal energy. On the other hand, in large parts of the world, such as Central Europe, the natural conditions are rather unfavorable and prototyping is not progressing fast enough. While missing temperatures can be compensated by higher drilling depths, these areas often lack the necessary high permeabilities within the reservoir rock to be able to produce sufficient quantities of fluid. In order to make the transition to renewable energies and geothermal energy production possible in these areas as well, the concept of the Enhanced Geothermal System (EGS) was developed (Genter et al., 2010; Gérard et al., 2006).

1.1 ENHANCED GEOTHERMAL SYSTEMS

The concept of EGS describes the utilization of low permeable but already fractured reservoir rocks as subsurface heat exchange for geothermal energy production. It is based on creating an artificial fluid flow between two or more boreholes along an existing fracture and fault network (Figure 1.2). The natural permeability of the network is thereby increased by thermal, hydraulic or chemical stimulation measures to such an extent that higher flow rates allow an economically viable operation (Huenges, 2016). Most common is hydraulic stimulation by creating a high fluid overpressure of several MPa in the reservoir to overcome the shear strength of existing fractures (Schill et al., 2017).

First research projects were started in the 1970's with the hot dry rock (HDR) project at Fenton Hill, New Mexico, USA. In contrast to EGS, the HDR concept creates new fractures through massive hydraulic stimulation (Jung, 2013). The first research projects in Europe began in 1987 with the French/German project at Soultz-sous-Forêts, France. Over a period of more than 25 years, scientific data was collected by generations of researchers before the power plant was finally transferred to economic operation (Mouchot et al., 2018). Several other commercial EGS projects were influenced by the Soultz research. While the importance

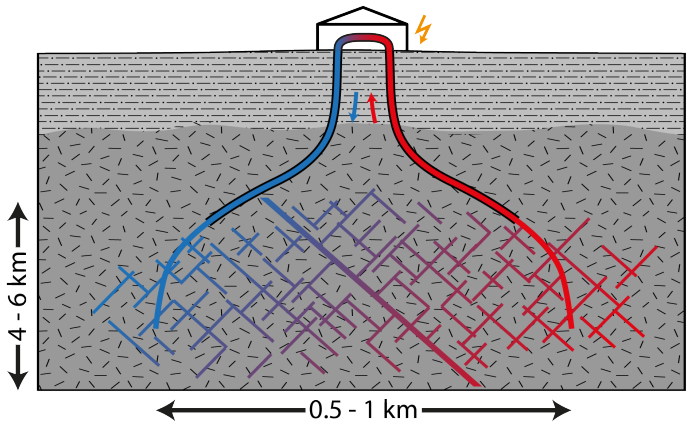

Figure 1.2: Sketch of an Enhanced Geothermal System. Heat energy is extracted from the subsurface using a production well (red). The chilled fluid is reinjected through another well back into the reservoir (blue). Within the reservoir the fluid circulation is realized through a network of fractures.

of the surrounding rock is rather subordinate, the detailed description of the fault and fracture network is of fundamental importance for the success of an EGS.

1.2 FAULT AND FRACTURE NETWORK

Fault zones are lithologically heterogeneous and complex discontinuities of the upper crust mainly consisting of an ultracataclastic core framed by a damaged zone of intensively fractured host rock and the original protolith (Choi et al., 2016). Under tectonic stress, shear processes take place mostly in the core, while only small amounts of displacement are observed in the surrounding damage zone (Faulkner et al., 2010). Depending on the internal structure and the tectonic and alteration history, the fault zone can act both as a hydraulic conduit or barrier or as a combined conduit-barrier (Caine et al., 1996) with fractures either open or sealed by alteration products (Barton et al., 1995; Meller et al., 2014). If these fault zones are located in low-permeable rocks, such as the Buntsandstein or granite of the Upper Rhine Graben, they have a strong influence on the local natural and also induced groundwater dynamics (Stober and Bucher, 2015).

Depending on the internal structure of the fault, a large number of fractures can form within the damage zone, acting as preferential flow paths (Aydin, 2000; Barton et al., 1997). The length, orientation, interconnection, and density of these fractures networks are key parameters for the description of the hydraulic conditions and the flow field within a geothermal reservoir (Berkowitz, 2002). However, not only the fracture network, but also each individual fracture can vary in its geometrical and hydraulic properties (Zimmerman and Bodvarsson, 1996). Tectonic processes, such as shear displacement, lead to rough fracture surfaces with locally varying apertures (Auradou et al., 2006). Mineral reactions, on the other hand, can lead to a sealing of the fractures (Meller et al., 2014; Schmidt et al., 2017). In order to be able to draw conclusions about the efficiency of a geothermal system, it is necessary to understand not only these rock-related

parameters, but also the interaction with the physical processes occurring within these fractures during power plant operation.

1.3 MULTISCALE MODELING

In a geothermal reservoir coupled thermo-hydro-(geo-)mechanical-chemical (THMC) processes of different spatial and temporal scales take place and create highly nonlinear dependencies between each other. It is therefore only rarely possible to trace natural as well as anthropogenic changes back to a single origin and to consider it independently and isolated from all other physical processes. In the highly dynamic fractured reservoirs, this problem is even more important because not only the interaction between the porous matrix and the fluid must be considered, but also the interaction of the individual fractures with both the fluid and the surrounding host rock (Berre et al., 2019; Tsang et al., 2015). For a sustainable and productive power plant operation these multiphysical and -scale interdependencies must be fully understood (Fox et al., 2013).

Theoretical assumptions and laboratory experiments can only cover these geological questions in their entirety, because they are fixed in space and time. Only the result of the THM-coupled processes can be measured and visualized. Therefore, various numerical applications have been developed in recent years that deal with the nonlinear coupling of such complex processes (Cacace and Jacquey, 2017; Gholami Korzani et al., 2020; Kohl et al., 1995; Taron et al., 2009; Watanabe et al., 2017). Numerical simulations allow the systematic investigation of complex multiphysical problems in a reasonable amount of time and money, taking into account large time and length scales as well as complex geometries (O'Sullivan et al., 2001; Pruess, 1990). The knowledge gained in this way (together with further experimental investigations) allows the development of numerical models for the prediction of geothermal reservoirs with regard to their performance and potential commercial and ecological risks (Dussel et al., 2016; Jacquey et al., 2016; O'Sullivan and O'Sullivan, 2016).

1.4 STRUCTURE OF THE THESIS

The possibilities and opportunities described above also raise questions regarding the limitations of numerical flow models and the importance of the scale of observation for each process. Exactly at this point the motivation for this dissertation arises, which I would like to introduce in the following. In accordance with the previously described possibilities offered by numerical models, this thesis aims to extend the knowledge of the multiphysical and multiscale processes leading to the formation and hydraulic feedback of preferential fluid pathways, e.g. in faults and fractures. Furthermore, their interaction with the surrounding porous host rock and the transport of solutes and heat associated with the fluid flow will be considered. For this purpose, experimental data obtained by laboratory and field experiments will be analyzed with respect to their informative value. The knowledge gained will be used to describe the complex and dynamic nature of geological processes in natural fractured reservoirs. The focus will

lie on the transferability of small to medium-scale laboratory investigations to large-scale reservoirs by numerical models.

Furthermore, I will point out three major questions, that I try to answer with this thesis: 1) Which processes are crucial for the assessment of the flow regime within a fractured reservoir? Are these processes dependent in time and space and how can we transfer them into numerical models without the risk of oversimplification? 2) Is it possible to scale laboratory results to large-scale models and which boundary conditions (e.g. geological heterogeneities or nonlinear interactions) have to be considered to ensure transferability? 3) Can we quantify the performance of such highly dynamic natural systems such as geothermal reservoirs and predict future behavior with sufficient accuracy? I answer these questions by transforming experimental data of different scales into complex numerical models.

Chapter 2 presents the fundamental equations and underlying assumptions for the different thermal, hydraulic and (geo-)mechanical processes used in this thesis. In addition, the mutual couplings of these processes in the fluid and solid phase of the fractured rock are given. In a short overview, the basics of the finite element method (FEM), the applications MOOSE (Permann et al., 2020), and TIGER (Gholami Korzani et al., 2020), and the corresponding generation of (un)structured meshes are explained. In Chapter 3, the temporal and spatial scale-dependence of geologic processes and the associated changes in effective material properties are discussed. Approaches towards numerical upscaling are briefly described.

Stochastic analysis of 3D Navier-Stokes flow on self-affine fracture surfaces

The first study (Chapter 4) is on the topic of small-scale hydraulic processes in fractured rock and is thus an ideal starting point for further investigations (such as the associated transport of solutes and temperature). Thirty unique and tortuous fracture geometries are used to study the effects of different pressure gradients and flow directions on the formation of preferential fluid pathways and expected flow rates. I attempt to analyze and identify the spatial differences between the fully-3D Navier-Stokes equations (NSE) and 2D local cubic law (LCL) solutions in terms of local flux, pressure gradient, and velocity. It can be shown that the complexity of natural fractures leads to anomalous flow fields with coexisting linear and nonlinear flow components even at low flow rates. The more ideal parabolic flow field, which is mainly formed along the identified channels, causes less deviations from the LCL, while areas away from these channels show a strongly nonlinear behavior even for Reynolds numbers (Re) $\ll 1$. In Chapter 5, the identified channels are further evaluated with respect to their length, volume, connectivity and continuity. The study focuses on the effective hydraulic parameters of rough fractures, such as the heat exchange surface and the fluid volume taking place in the transport of solutes. These parameters differ significantly from a) the parallel plate approach and b) the entire fracture area, since large parts of the volume flow are located in small parts of the fracture.

Triaxial testing and hydraulic–mechanical modeling of sandstone reservoir rock in the Upper Rhine Graben

Chapter 6 focuses on the hydro-mechanical behavior of two different sandstone types from the Upper Rhine Graben exposed to compaction under confined and drained conditions. The study has two main focuses: 1) the investigation of the nonlinear poro-elastic behavior of the low-permeable reservoir analogs with respect to their hydraulic properties (porosity and permeability) and 2) the irreversible deformation and failure strength of the sample with respect to the confinement in a reservoir. The calibration of the numerical results is done by different small-scale laboratory tests, which were performed on a significant amount of different samples to determine the critical material properties. The results show that a poro-elastic model can predict stress-strain-relation with increasing compaction with high accuracy. The compaction-induced porosity changes are well captured and used for calculating the permeability-changes with a Kozeny-Carman-like permeability model. The failure strength for both types of sandstone with increasing confining pressure is evaluated using a overstress plasticity law and a three-dimensional Drucker-Prager-like yield envelope (Drucker and Prager, 1952). The study emphasizes that micro-scale differences (e.g. mineral content) can lead to different material properties and hydro-mechanical behavior, but that these rocks can still be described on a meso-scale with the same analytical and numerical models.

Implications on large-scale flow of the fractured EGS reservoir Soultz inferred from hydraulic data and tracer experiments

In Chapter 7, I leave the laboratory scale and analyze the hydraulic and transport properties of the EGS in Soultz-sous-Forêts, France. The study focuses on the precise numerical modeling of the natural and anthropogenic-induced flow field in the discrete faults and fractures. For this purpose, 13 permeable fractures are identified from a variety of geological and geophysical input data in order to extend an existing discrete fracture matrix model (DFM) according to Held et al. (2014) with this information as well as to calibrate the flow dynamics by means of various long-term circulation experiments. This hydraulic field is subsequently used to establish a novel transport modeling approach for the simulation of high-resolution tracer experiments in the reservoir-scale and to quantify the interconnections of individual wells along a fracture network. The simulation confirms the strong heterogeneity of the reservoir and highlights the importance of a potential fractured zone, hydraulically separating the reservoir in a northern and southern section. For Chapter 8 the previously described hydraulic model is used to investigate different operation scenarios of the power plant with respect to their thermo-hydraulic sustainability. In a 60-year prediction model, the expected production temperatures are examined as flow rates and reinjection temperatures are changed from the current case.

2

FUNDAMENTAL PROCESSES IN THE RESERVOIR ROCK

Enhanced Geothermal Systems consist of different features representing different scales and dimensions, namely the porous rock matrix, faults- and fractures, wellbores, and a geothermal fluid (Figure 2.1). All these features can transport or insulate the stored heat. The fluid is generally referred to simply as a single-phase liquid, which is permissible at the pressures of several MPa prevailing in the reservoir. The various faults and fractures can act, as previously described, as hydraulic conductors or barriers. The wellbores are drilled to access the reservoir fluid in the target formation and for reinjection of the cooled fluid.

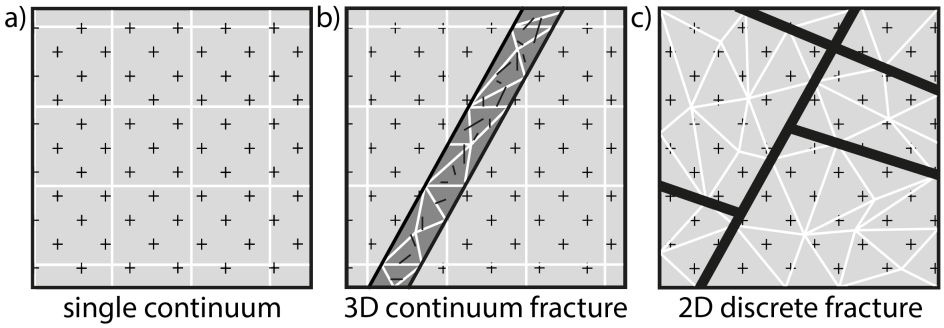

Figure 2.1: Different approaches describing the representative elementary volumes of matrix and fracture. a) As a single continuum, e.g. like pure porous media, b) as multiple continua, where the fracture is represented in 3D, c) as mixed dimensional porous media and lower-dimensional discrete fractures.

According to Bear (1988), these individual features are regarded as a composition of multiple representative elementary volumes (REV), the 3D 'porous media', 2D (or rarely 3D) 'discrete fractures', and 1D 'wellbores'. Each REV consists of averaged material properties that are related to pore-scale quantities of the entire domain. The physical processes within and between these REVs must be considered numerically. Porous media are generally assumed to be the average of the micro-scale highly heterogeneous rock matrix, taking into account the permeability of both the porous rock matrix and small-scale rock fractures (Watanabe et al., 2017). An extension is the dual-continuum model, where e.g. faults or fractures are represented as a separate medium with distinctly different material properties and its geometrical information. Discrete fractures represent macro-scale features, which are of explicit importance on the scale of observation (Berre et al., 2019). However, hydraulic barriers and shearing of fracture surfaces cannot be represented with lower-dimensional discrete features. In geology, no

clear distinction can be made between these forms of representation, so that they can coexist and the interaction between fractures and fracture networks with dynamic processes in the domain has to be considered (Adler et al., 2012).

In the following chapter, the basic equations for the concept of continuum mechanics and involved thermal, hydraulic, and mechanical (THM) processes and its mutual couplings in the porous media and fractures are summarized. For a detailed overview and its derivation, the corresponding literature is listed in each subchapter. Chemical processes, like water-rock-interaction or reactive transport, are beyond the scope of this thesis. In this context, I refer to the work of Nitschke (2017) and Schmidt (2019), for example.

2.1 GEOMECHANICAL PROCESSES

2.1.1 *Elastic deformation*

The geomechanical processes taking place in the earth's crust can be distinguished mainly into elastic and plastic deformation and subsequent brittle and creep failure. The following introduction is based on the work of Fjar et al. (2008), Jaeger et al. (2007) and Zoback (2011). The deformation is measured as strain and leads to stresses in the interior of the rock. Stress is defined as the force per area acting parallel or perpendicular to the three spatially different surfaces of a volume of rock. The stress tensor combines the resulting three unique vectors into a single second-order stress tensor σ_{ij} consisting of 9 components with $i, j = 1, 2, 3$. The first index designates the direction of the surface normal, the second index the direction in which the stress acts. The diagonal entries of the stress tensor are called normal stresses σ_{ij}, the remaining shear stresses τ_{ij} (Figure 2.2). Due to the balance of momentum conservation, the stress tensors must be symmetric, which reduces the number of independent components to 6. Thus, the stress tensor is defined:

$$\sigma = \begin{pmatrix} \sigma_{xx} & \tau_{xy} & \tau_{xz} \\ \tau_{xy} & \sigma_{yy} & \tau_{yz} \\ \tau_{xz} & \tau_{yz} & \sigma_{zz} \end{pmatrix} \tag{2.1}$$

The stress tensor can be simplified even more by calculating its eigenvalues, leading to the principal stresses σ_1, σ_2 and σ_3, which yields the orientation in the former coordinate system:

$$\sigma = \begin{pmatrix} \sigma_1 & 0 & 0 \\ 0 & \sigma_2 & 0 \\ 0 & 0 & \sigma_3 \end{pmatrix} \tag{2.2}$$

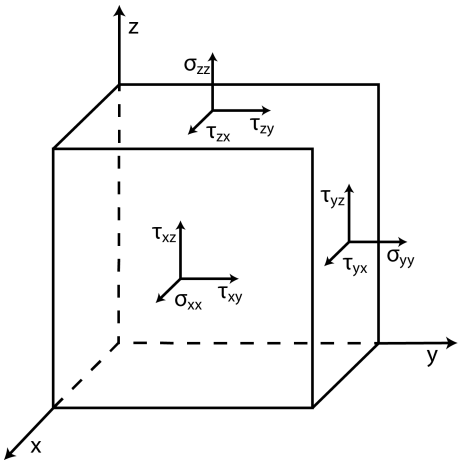

Figure 2.2: The stress tensor components acting on the volume planes.

Conventionally these stresses are in descending order:

$$\sigma_1 > \sigma_2 > \sigma_3 \tag{2.3}$$

with σ_1 as the maximum principal stress. In rock mechanics conventionally $\sigma > 0$ means compression and $\sigma < 0$ means tension (Fjar et al., 2008).

Mechanical stress leads to a displacement field u, which can be expressed by the second-order strain tensor:

$$\epsilon_{ij} = \frac{1}{2}\left(\frac{\partial u_i}{\partial x_j} + \frac{\partial u_j}{\partial x_i}\right) \tag{2.4}$$

If a linear elastic material is considered, the relation between the stress tensor σ and strain tensor ϵ is given by Hooke's law, where C_{ijkl} is the symmetric stiffness tensor (Jaeger et al., 2007):

$$\sigma_{ij} = C_{ijkl}\epsilon_{kl} \tag{2.5}$$

For an isotropic medium, like a rock matrix is, the stiffness tensor can be expressed as:

$$C_{ijkl} = \lambda\delta_{ij}\delta_{kl} + G(\delta_{ik}\delta_{jl} + \delta_{il}\delta_{jk}) \tag{2.6}$$

where δ_{ij} represents the Kronecker delta. Leading to the generalized form of Hooke's law for isotropic media:

$$\sigma_{ij} = 2G\epsilon_{ij} + \lambda\epsilon_{kk}\delta_{ij} \tag{2.7}$$

Where λ and G are the Lamé parameters, G is also known as the shear modulus. The further important elastic parameters are known as bulk modulus

K, Young's modulus E and Poisson's ratio ν. If at least two moduli are known, the others can be calculated as follows, where dV and dP are the change in sample volume and pressure (Zoback, 2011):

$$K = -V\frac{dP}{dV} = \lambda + \frac{2}{3}G \tag{2.8}$$

$$E = G\frac{3\lambda + 2G}{\lambda + G} \tag{2.9}$$

$$\nu = \frac{\lambda}{2(\lambda + G)} \tag{2.10}$$

2.1.2 *Thermo-poroelastic coupling*

A geothermal reservoir is a porous medium, so it consists of a skeleton of solid phase and intermediate void space also known as porosity. This pore space is saturated with e.g. geothermal brine or hydrocarbons. The fluid ensures that the pores cannot simply be compacted and thus acts as a tensile force within the rock. Terzaghi (1943) made the first theoretical assumptions in this respect, introducing the concept of effective stress $\sigma_{ij}^{'}$ as the coupling between the absolute stress σ_{ij} and the pore pressure P_f. Biot (1956) further modified this assumption to take into account the compressibility and bulk modulus of the rock. The Biot's coefficient α is a function of the drained bulk modulus of the porous medium (Carroll and Katsube, 1983):

$$\sigma_{ij}^{'} = \sigma_{ij} - \alpha P_f \tag{2.11}$$

The coupling of T, H, and M also has spatial effects on the pore skeleton. A single rock body expands linearly and uniformly in all directions with increasing temperature and pore pressure. If the deformation of the solid is prevented, e.g. by the surrounding rock, stresses arise. These lead to a change in the pore volume or porosity by compressing the rock skeleton with increasing pore pressure or by expanding the solid phase with increasing temperature (Jaeger et al., 2007):

$$\Delta\phi = (1 - \phi)(\beta_s \Delta P_f - \lambda_s \Delta T + \Delta\epsilon_{vol}^{el}) \tag{2.12}$$

where ϕ is the porosity, $(\beta_s \Delta P_f)$ is related to the compression of the solid phase due to the pore pressure and $(\lambda_s \Delta T)$ is related to the thermal expansion of the matrix due to rising temperatures and ϵ_{vol}^{el} is the change in volumetric strain due to elastic deformation.

2.1.3 *Rock failure*

Generally, rock masses are assumed to be in frictional equilibrium and faults tend to be balanced (Zoback, 2011). Failure or fracturing occurs if due to changes in the stress regime, a certain threshold of shear stress τ is exceeded. The most simple failure criterion is the criterion after Coulomb (1773), which considers the maximal and minimal principal stresses. The minimum frictional stress as the criterion for failure is a product of the normal stresses multiplied by a coefficient of friction μ. It is assumed that intact rock masses have a certain strength even if normal stresses are absent, which is known as cohesion S_0. The absolute failure strength is therefore calculated as follows:

$$|\tau| \geq S_0 + \mu\sigma \tag{2.13}$$

For crustal rocks, like granite or sandstone, the coefficient of friction is typically assumed to be in the order of 0.85 (Byerlee, 1978), for clay and weak fault zones μ can be decreased to 0.2 (Tembe et al., 2009). More complex failure criteria have been developed, which partly take into account the intermediate principal stress and also other rock-typical parameters (Zoback, 2011). The most common and time- and material-independent criterion is introduced by Drucker and Prager (1952), which also sets deviatoric and volumetric mean stresses in a linear relationship. Plastic (and thus irreversible) deformation must increasingly be considered in the transition zone between elastic deformation and the failure of the rock body. The onset of plastic deformation is strongly material-dependent and is generally described by a yield criterion. For a mathematical consideration of these two factors (Drucker-Prager criterion and plastic deformation) please refer to Chapter 6.

2.2 HYDRAULIC PROCESSES

2.2.1 *Fundamentals of fluid flow*

Fluid flow is governed by the principle of mass balance and momentum conservation and in the case of a viscous Newtonian fluid, such as water, generally described by the Navier-Stokes equations (NSE). In the case of laminar flows and incompressible fluid, both in the porous medium and in the fracture, this equation can be simplified to the generally known Darcy Law. A detailed derivation, as well as theoretical basics, are presented in the works of Bear (1988), Istok (1989) and Lukaszewicz and Kalita (2016), so that I limit myself to the equations used and further analyzed in this work.

Incompressible and steady-state fluid flow is governed by the following Navier-Stokes equation and mass conservation (Bear et al., 1993):

$$\rho(\boldsymbol{u}\nabla)\boldsymbol{u} = -\nabla P + \mu\nabla^2\boldsymbol{u} + \boldsymbol{f} \tag{2.14}$$

$$\nabla\boldsymbol{u} = 0 \tag{2.15}$$

where ρ is the fluid density, P is total pressure, $\boldsymbol{u}$ is velocity vector, $\boldsymbol{f}$ the body force vector (e.g. gravitational acceleration) and μ is dynamic fluid viscosity. The left-hand side in Equation 2.14 covers the inertial term, while the right-hand side can be described by the viscous and body forces.

For stationary and laminar flow conditions, this equation simplifies to the Stokes equation, neglecting inertial forces:

$$0 = -\nabla P + \mu \nabla^2 \boldsymbol{u} \tag{2.16}$$

If it is assumed that the viscous resisting force is linearly related to the velocity, a second-order permeability tensor can be introduced as a proportionality parameter:

$$0 = -\nabla P + \boldsymbol{k}_{ij}^{-1} \mu \boldsymbol{u} \tag{2.17}$$

In the case of isotropic porous media, the off-diagonal elements of this tensor are zero and the diagonal terms are all equal ($k = k_{ii} = k_{jj} = k_{zz}$), which leads to the generally known equation for single-phase fluid flux (Whitaker, 1986), also known as Darcy Law (Darcy, 1856):

$$\boldsymbol{q} = \frac{\boldsymbol{k}}{\mu}(-\nabla P + \rho^l \boldsymbol{g}) \tag{2.18}$$

where $\boldsymbol{q}$ is the Darcy flux and $\boldsymbol{k}$ is the permeability, which is typically measured in laboratory or field experiments.

2.2.2 *Fracture flow*

Besides porous rocks, the Darcy equation can also be applied to flow in open fractures assuming them as pair of smooth parallel plates (Louis, 1967). The permeability in a fracture is calculated as (Bear et al., 1993):

$$\boldsymbol{k} = \frac{a^2}{12} \tag{2.19}$$

where a is the fracture aperture. This leads to a cubic relationship between the volumetric flow rate Q and the aperture a ($Q \propto a^3$, Snow, 1965). The cubic law (CL) is the most common approximation for fluid flow in fractures. However, fractures cannot be represented by a parallel plate model of constant spacing. Tectonic processes, such as shearing of two opposing fracture surfaces (Auradou et al., 2005) or hydrothermal alteration (including dissolution and precipitation processes, Meller et al., 2014) lead to laterally highly variable apertures, which are averaged for the CL (Witherspoon et al., 1980). Nevertheless, the expected flow rate is often significantly overestimated compared to laboratory experiments (Brown, 1987).

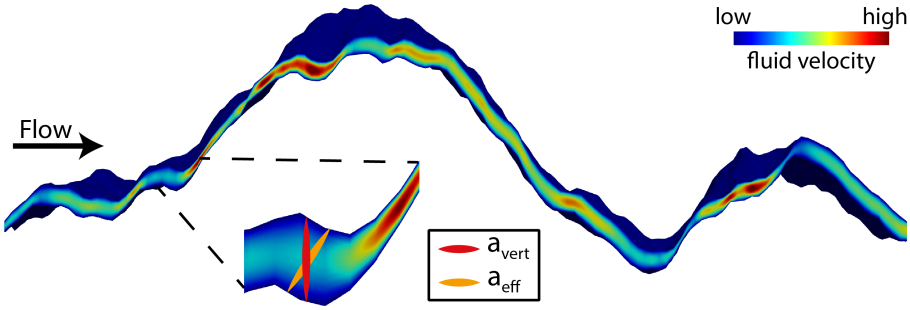

Figure 2.3: Cross section through a rough and sheared fracture geometry. The color scale represents the local velocities determined by flow modeling using the Navier-Stokes equations and a pressure gradient from left to right. In an enlarged section, two common types of aperture definition, calculated either perpendicular to the global (red) or local (yellow) median plane are shown.

The local cubic law (LCL) is a significant extension of the classical CL, taking into account local apertures and pressure gradients (Nicholl et al., 1999). Since the LCL is a cubic function of the aperture, the computed hydraulic field is very sensitive to a proper definition of the aperture. The most common definition uses a mechanical aperture a_{vert} measured perpendicular to the entire fracture median plane (Brown, 1989). This definition often yields an overestimation of the flow rate, so the determination of a hydraulic aperture is recommended (Cheng et al., 2020). Common approaches are the calculation of an effective aperture a_{eff} perpendicular to the local median plane (Figure 2.3, Ge, 1997) or using (empirical) modification parameters to account for various geometric effects such as surface roughness or tortuosity (Konzuk and Kueper, 2004; Wang et al., 2015). Positive changes in the aperture can occur when a fracture is pressurized, e.g. with hydraulic stimulation. Due to missing reservoir measurements, changes in aperture caused by the elastic response as well as by shearing are generally described by empirical models, which have been evaluated and verified by laboratory data (Chen et al., 2000; Schrauf and Evans, 1986). The most common models are described by Willis-Richards et al. (1996) and Barton et al. (1985).

The simplified approach of the CL and LCL is only valid for laminar flows in smooth fractures, whereas for turbulent flow conditions, as shown in Figure 2.3, the NSE (Equations 2.14 and 2.15) must be solved inevitably. However, since this is very computationally expensive, different empirical turbulent flow laws have been developed, e.g. the Forchheimer (Frih et al., 2008) or the Missbach law (Elsworth and Goodman, 1986). The transition from laminar to turbulent flow conditions is generally determined utilizing the dimensionless Reynolds number (Re), which is a measure for the occurrence of inertial effects:

$$Re = \frac{vd\rho}{\mu} \tag{2.20}$$

where v is the fluid velocity, d is the characteristic length of the medium, e.g. in fractures the aperture or in porous media the grain size. A transition from laminar to turbulent flow conditions follows from $Re > 1$ in fractured rock

(Brush and Thomson, 2003; Zimmerman et al., 2004) or above 40 in porous media (Bear, 1988; Scheidegger, 1974).

2.2.3 *Fluid properties and thermo-hydraulic coupling*

The thermo-hydraulic coupling is achieved by changes in the thermodynamic material properties (e.g. density, viscosity, and compressibility) of the fluid and phase in relation to the p-T-state of the system and is generally characterized by the equation of state (EOS) (Ramey et al., 1974). The EOS of geothermal fluids can be reduced to two main processes: vapor-liquid equilibrium and aqueous/non-aqueous (two-phase) (Nusiaputra, 2017). Over many years, many different physical and analytical EOS have been developed with increasing accuracy in terms of material properties and nonlinear feedbacks. A derivation exceeds the focus of this thesis, so for the EOS common in geothermal systems reference is made to the work of Redlich and Kwong (1949), Peng and Robinson (1976), Smith and Chapman (1983), and Wagner and Pruß (2002).

2.3 TRANSPORT PROCESSES

Transport processes are used to describe the spatial changes of heat or solutes, such as salts, tracers, or contaminants, in the geothermal reservoir. Depending on the type of transported medium and background material, three processes are involved and summarized in Equation 2.21: Advection, diffusion, and dispersion. The Darcy velocity realizes the coupling between the pressure field and the advective term of the transport equation. In the following, the processes that are important for this thesis are described, a detailed review can be found in the monographs of Bear and Cheng (2010) and Diersch and Kolditz (1998):

$$b\frac{\phi\delta C}{\delta t} + b(-\nabla.\boldsymbol{D_m}\nabla C + \boldsymbol{q}\nabla.C) = Q \tag{2.21}$$

where C is the variable of interest; ϕ is the porosity; $\boldsymbol{D_m}$ is the sum of molecular dispersion $\boldsymbol{D_{ij}}$ and isotropic diffusion D. The dispersion tensor $\boldsymbol{D_{ij}}$ is dependent on Darcy velocity and longitudinal a_L and transversal dispersivity a_T, which generally describes the mixing around maximum due to different hydraulic or mechanical effects (Bauget and Fourar, 2007) and defined as follow (Istok, 1989):

$$\boldsymbol{D_{ij}} = (a_L - a_T)\frac{\boldsymbol{vv}}{|v|} + (a_T|v|) \tag{2.22}$$

where $|v|$ is the magnitude of the fluid velocity vector. Diffusion is only of minor importance for solute transport but of major importance for heat transport, especially in host rocks with low conductivity.

This general form of the equation can be used for the transport of conservative solutes, such as non-reactive tracers. The energy balance law is a special form

of the transport equation, neglecting dispersion effects (Gholami Korzani et al., 2020):

$$b\rho c_p \frac{\delta T}{\delta t} + b(-\boldsymbol{\lambda}\nabla.\nabla T + \rho^l c_p^l \boldsymbol{q}\nabla.\boldsymbol{T}) = Q \tag{2.23}$$

where $\rho^l c_p^l$ is the effective heat capacity of the porous media, $\boldsymbol{\lambda}$ is the effective thermal conductivity tensor and c_p^l the specific heat capacity of the fluid only. Both can be calculated as the mean value of each phase weighted by the volumetric fraction:

$$\rho c_p = n\rho^l c_p^l + (1-n)\rho^s c_p^s \tag{2.24}$$

$$\lambda = n\lambda^l + (1-n)\lambda^s \tag{2.25}$$

2.4 NUMERICAL IMPLEMENTATION

2.4.1 *Finite element method*

The governing nonlinear equations are solved numerically with the finite element method (FEM) for spatial discretization and the finite difference method (FDM) for temporal discretization. The FEM was chosen because it allows the creation and modeling of complex and unstructured geometries. In general, in FEM all geometric objects are represented by a mesh consisting of nodes and connecting elements, which can be 0D vertices, 1D lines, 2D triangles, or quadrangles, and 3D tetrahedra, hexahedra, or pyramids (Figure 2.4). Mixing of the dimensions is possible and as already described in chapter 2 necessary for studying EGS (Watanabe et al., 2017). For the implementation of continuity conditions of variables at the interface between porous media and fractures, it is necessary to locate fracture elements along the edges of porous media elements and ensure that both types of elements share the same nodes (Segura and Carol, 2004).

In FEM physical laws for spatial and temporal problems are represented by partial differential equations (PDEs). An analytical solution is often not possible; therefore, an approximation must be found utilizing different discretization models. These discretization models correspond to the numerical solution function, which is used to solve an approximation of the PDE for a real problem. This function is iterated until the real solution is found with sufficiently high accuracy. The solution of coupled problems follows the portioned approach, whereby each process is first iterated individually before a global and often nonlinear solution converges with sufficient precision (Kolditz et al., 2015). Especially when coupling complex physics with different temporal and spatial scaling, as in the EGS, several interconnected issues have to be considered to achieve a solution with high accuracy (Kohl et al., 1995). Examples include the selection of the spatial discretization adopted, the time-stepping scheme and integration, iterative solvers, and preconditioners.

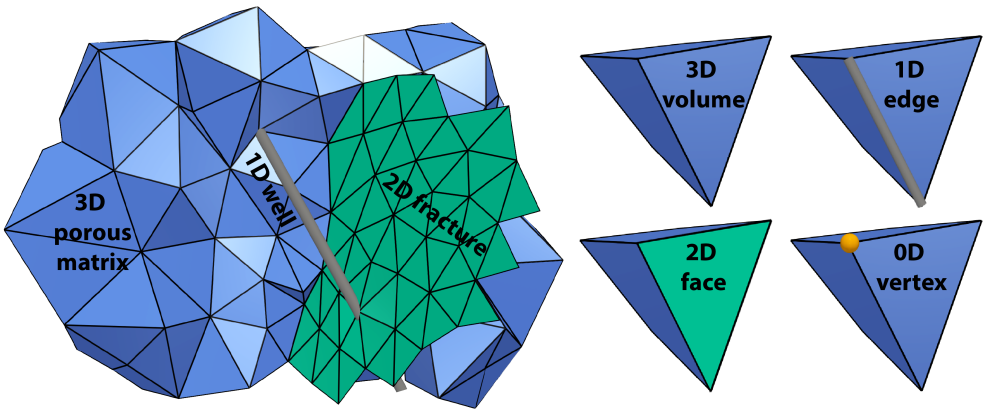

Figure 2.4: Schematic representation of the approach for modeling a fractured reservoir by superimposing lower and higher dimensional elements: 0D vertex (source/sinks), 1D edge (well paths), 2D face (fractures and simplified faults), and 3D elements (porous media).

2.4.2 *Moose*

The PDEs are solved using the object-oriented numerical framework MOOSE (Multiphysics Object Oriented Simulations Environment) developed at the Idaho National Laboratory (Gaston et al., 2009; Permann et al., 2020). MOOSE offers a flexible and massive parallel (including both MPI and multi-threading) platform to solve fully coupled multi-physical and multi-scale problems using Galerkin FEM in a fully implicit manner. It uses state-of-the-art libraries, such as the libMesh library (Kirk et al., 2006), which was developed at the University of Austin in Texas for parallel FEM capabilities or a variety of scalable parallel, direct, nonlinear, and linear solvers (PETSc, Hypre or Trilinos) (Balay et al., 2016). This flexibility allows us to deal with realistic scenarios including complex geometries as well as nonlinear and coupled physics while maintaining computational efficiency.

The MOOSE platform is based on a strictly hierarchical and modular design, enabling users with limited knowledge of physics to work out complex problems numerically (Gaston et al., 2009). The modeling and parameterization are carried out employing an input file. In the first step a 'mesh' is defined, and either a simple geometric shape is generated, or a complex mesh is linked or modified. The heart of each file are the 'kernels', which each represent a part of the physics and can be used independently or coupled. Similarly, the 'boundary conditions' (BCs) are handled internally, which represent constraints for the respective problem. Common BCs are of the Dirichlet or Neumann type. The 'materials' block contains all material properties (e.g. density, Young's modulus, thermal conductivity) necessary for the solution of the respective problem. The parameterization can be done for the whole model, but also for subsets or even locally resolved. Finally, settings for the execution of the modeling, such as the type of solver or time-stepping, are defined in the 'executioner'.

2.4.3 *Tiger*

The equations presented and used in this thesis are integrated into the MOOSE-based open-source application TIGER (THMC sImulator for GEoscientific Research) (Gholami Korzani et al., 2020). TIGER is developed at KIT, by the author of this thesis among others, for the efficient and optimized modeling of thermo-hydro-mechanical-chemical processes within anisotropic porous and fractured media ranging from small-scale single fractures to fully-coupled geothermal reservoirs. TIGER is developed as a modular toolkit to be able to integrate new application-dependent functions, e.g. physical processes, equation of state, customized specific boundary conditions, relatively easily. TIGER and some simple benchmarks are available under GNU General Public License version 3.0 as GitHub repository (https://github.com/MGK-Lab/tiger).

3

SCALE-DEPENDENCE IN GEOLOGICAL PROCESSES

In some cases, the change of scale is efficient and easy to perform, while the influence of geological processes can vary considerably both in spatial and temporal scale. Some macroscopic phenomena may have their origin in microscopic, yet scalable effects, while others may achieve their structure at the macroscopic scale itself or be a combination of different scales. A further level of complexity arises when these processes influence each other across scales. When applying scaling laws, it is hence important to validate them with physical observations (Allègre et al., 1982). In the following, the physical processes and rock properties in the fractured medium will be considered with respect to their scale-dependence and upscaled dynamics. In addition, general upscaling approaches and their limitations are discussed.

In Chapter 2 the concept of the 'representative elementary volume' (REV) is introduced. This concept is the most common way to overcome scale-dependence in connection with geoscientific questions and to allow an upscaling from micro to macro-scale. It is assumed that the scale of the problem to be solved is significantly larger than the length scale of the physical processes involved or rather that these processes are scale-invariant. The element, e.g. a geological unit, can thus be 'homogenized' by determining an effective material property consisting of the weighted average of the smaller-scale heterogeneous rock properties (Dagan et al., 2013). While field equations, such as mass conservation,

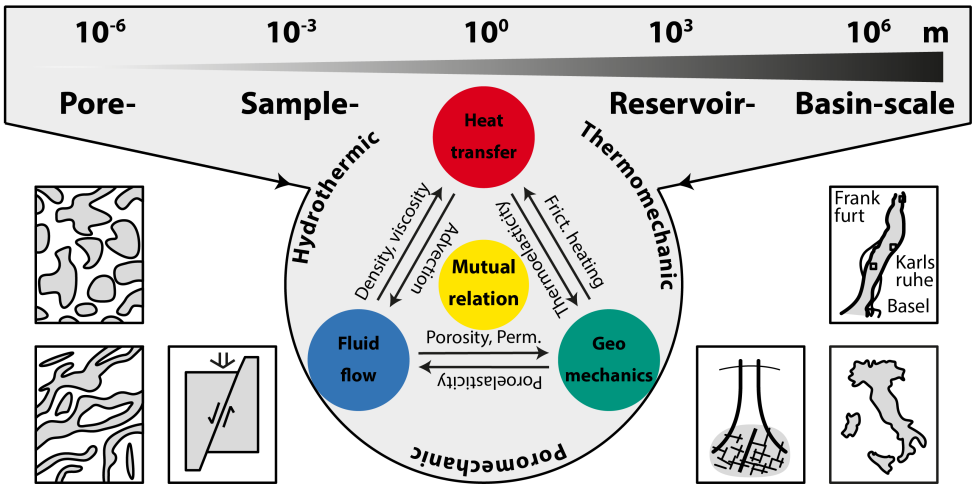

Figure 3.1: Sketch of the different scales and mutual couplings with examples.

thus remain identical, the experimentally determined parameters involved in the constitutive equations, e.g. Hooke's or Fourier's law, are modified depending on the scale of observation (Cushman et al., 2002). In the case of fractured reservoirs, it is of crucial importance from which extent fractures are represented as explicit and discrete elements, since these have a significant influence on the thermal, hydraulic, and mechanical rock properties (Jackson et al., 2000). The following chapters will therefore examine the scale-dependence of fractures and fracture networks and examine the effects of geometrical upscaling with respect to constitutive laws and parameters in more detail.

3.1 SPATIAL SCALE-DEPENDENCE

The smallest possible scale of observation is represented by the individual fracture surfaces or the grains and pore spaces of porous rock. Natural fracture surfaces, e.g. of granitic rocks, are rough and exhibit scale-invariance over a wide range of wavelengths (Méheust and Schmittbuhl, 2003), so they can be defined by mathematical functions (Brown, 1989; Brown et al., 1995). Schmittbuhl et al. (1993) showed that any rough surface can be described as an isotropic self-affine fractal in which a subregion of the surface is statistically identical to the entire surface with the local height changes represented by the roughness or Hurst-coefficient H. The topography has therefore a 2D Fourier spectrum with an amplitude that scales as power-law with an exponent of $-2(1+H)$. From the rough wall follows the definition of the fracture aperture, which describes the separation between opposing surfaces. Méheust and Schmittbuhl (2003) showed the self-affinity of fracture apertures up to a certain mismatch length scale. Corresponding fluctuations occur above this threshold and the aperture can no longer be described in a pure geometrical sense. Instead, the effective permeability depends on the specific process (e.g. fluid flow or solute transport) (Silliman, 1989; Tsang, 1992). The most common aperture definitions are already discussed in Chapter 2.2.1.

Now I leave the actual laboratory-scale because a rock usually consists of a multitude of fractures of variable density, length, orientation, and aperture, which are more or less well connected (Allègre et al., 1982). These systems, independent of their origin (shear, tensile) are usually characterized in terms of frequency distribution and geometry using power-law exponential distributions and/or fractal dimension (Berkowitz et al., 2000; Bour, 2002), e.g. in the form of:

$$n(l)dl = cl^{-a}dl \tag{3.1}$$

where a is a power-law exponent, typically in the range between 1.5 and 3.5, and c a normalization constant like the fracture length space (Afshari Moein et al., 2018). The advantage is that the approach is scale-invariant and thus not subjected to any characteristic quantity. The disadvantage is that data are rarely available over more than two orders of magnitude, and lower and upper physical limits may lead to uncertain or meaningless results (Bonnet et al., 2001; Mandelbrot, 1982). The lower limit is assumed to be the limit of resolution

to observe short-scale fractures (truncation) and the upper limits are major fractures and faults, which can just be incompletely sampled (censoring), or local lithological changes, e.g. in sedimentary beds (Torabi and Berg, 2011). While the frequency and length of fractures described above are rather theoretical, these scale effects also have practical implications for material properties that must be considered. Laboratory studies help to identify the fundamental scale effects, but oversimplification in the upscaling can lead to non-representative statements about the heterogeneous reservoir (Amann et al., 2018).

3.1.1 *Hydraulic effects*

Fluid flow in EGS is mainly governed by the effective aperture and resulting permeability of the individual fractures as well as interconnection of the complex and heterogeneous fracture network, while the host rock is treated as a homogeneous porous medium (Sposito, 2008). Qian et al. (2007) were able to show experimentally an asymptotic increase of effective permeability with fracture length for a single fracture. Clauser (1992) was able to show the increase of the permeability of crystalline rock with increasing experimental scale based on laboratory and field studies at the KTB site and a stabilization of permeability at the regional scale indicating an upper threshold. Neuman (1994) generalized the data of Gelhar (1994) and Clauser (1992) to fit a power-law distribution with increasing length scale. Recent experiments (recovery-, cross-hole-, and inflow tests) carried out in the Grimsel underground research laboratory in Switzerland also confirm this hypothesis (Martinez-Landa and Carrera, 2005). Figure 3.2 shows mean permeabilities obtained from various laboratory and large-scale studies in fractured rocks (Clauser, 1992; Guimerà et al., 1995; Hanor, 1993; Hsieh, 1998; Hsieh et al., 1985; Illman, 2006; Kiraly, 1975; Martinez-Landa and Carrera, 2005; Rovey and Cherkauer, 1995). The reason for this scaling effect is often mentioned as the scale variance of complex geological features such as pores, micro-and macro-fractures, and major fault zones. These features can only be considered if they are fully exposed within the area of observation. Therefore, large-scale features cannot be captured in small-scale laboratory analyses.

3.1.2 *Mechanical effects*

The mechanical properties of an unmated rock are only subject to a minor scale-dependence but depend on its mineral composition. A natural rock, however, has a fissurization that leads to a significant reduction in the stiffness and strength of the entire rock body (Guéguen and Boutéca, 2004). Barton and Choubey (1977) proposed the usage of a Joint Wall Compression Strength (*JCS*) instead of Unconfined Compressive Strength (*UCS*), which takes into account the effects of rock weathering and cracking. Heuze (1980) collected and analyzed rock strength and friction data for different kinds of rock samples and scales. The author was able to show a decreasing strength for almost all rocks up to a certain cut-off length, but that this trend is not present on a larger scale. Bandis et al. (1981) were also able to demonstrate a strongly nonlinear decreasing trend of the peak

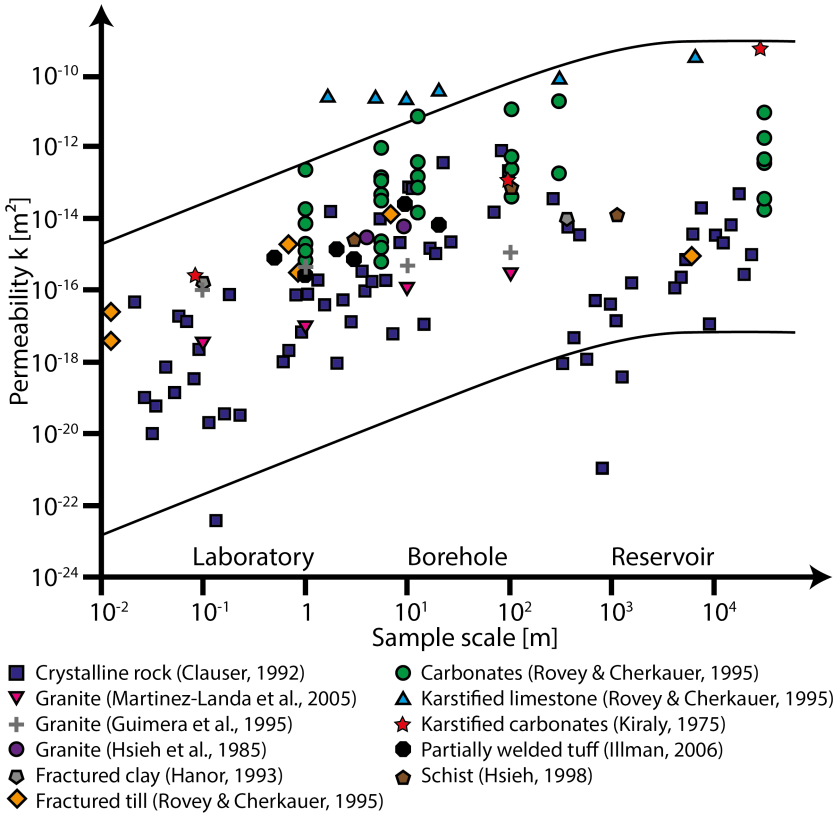

Figure 3.2: Variation of permeability as a function of sample size for different types of fractured rocks (modified after Azizmohammadi and Matthäi, 2017; Clauser, 1992; Illman, 2006).

strength with increasing fracture length on the laboratory scale experimentally. This is explained by the decreasing influence of local asperities with increasing overall sample length (Barton, 2016). The results indicate the presence of a REV in the meso- to macroscale range and show that material contrasts caused by geological heterogeneity on the reservoir scale significantly exceed the scale effects (Egert et al., 2018).

3.1.3 *Transport-related effects*

The dynamics of the transported species are mainly influenced by the hydraulic properties of the fractured medium (e.g. permeability). Another, albeit smaller, scale-dependence arises from dispersion, which is a measure of the internal mixing of tracer or heat due to different geometrical (and thus scale-dependent) effects (Icardi et al., 2019). Dispersion comprises various superimposing and mutually influencing spatial and temporal effects, making it a complex material parameter and making isolated analysis difficult (Bodin et al., 2003a,b). On the local scale, the Taylor-Aris dispersion dominates, which represents the mixing due to the parabolic velocity profile within fractures and thus gains importance with increasing velocity (Aris, 1956; Horne and Rodriguez, 1983). Along a single fracture, its roughness and locally varying apertures lead to a heterogeneous

velocity field and increasing mixing. This has been confirmed both experimentally (Dronfield and Silliman, 1993) and numerically (Moreno et al., 1988). Based on stochastic calculations, Gelhar et al. (1992, 1993) could show that this local hydrodynamic dispersion asymptotically approaches the maximum if the correlation length of the fracture is reached for ten times. At the reservoir scale, as in fracture networks, this microdispersion is superimposed by the strong velocity contrasts of the individual fluid pathways (Schwartz et al., 1983). Analogous to the individual fractures, an asymptotic approach to a maximum threshold value for increasing transport distance can be found numerically (Zhao et al., 2010) and experimentally (Guihéneuf et al., 2017). Tsang et al. (1988) concluded, that it is suitable to use a statistically homogeneous system (e.g. for aperture, permeability) if the transport dimensions are significantly larger than the spacing between the channels belonging to a fracture. A scale-dependence on diffusion into the surrounding matrix exists less for solute than for heat transport. Klepikova et al. (2016) showed numerically that a localization of fluid in preferential channels generates a scale-dependence in heat exchange with the matrix.

3.2 TEMPORAL SCALE-DEPENDENCE

Directly connected to the above processes and often not separable is the temporal scale-dependence. Temporal scale-dependence arises as a consequence of fracture nucleation and growth as well as poroelastic and water-rock-interaction processes that lead to changes in the physical properties of the reservoir rock. In contrast to the spatial dependence, the different temporal dependencies can cover a broad range of periods and be of natural or induced origin. For example, Cowie et al. (1995) were able to show numerically that the temporal formation of fractures follows a fractal scaling. With increasing time and decreasing strain-rate, smaller fractures are created. In geothermal reservoirs, changes in pore pressure and temperature propagate with increasing production time to further distances from the boreholes and lead to changes in porosity and permeability due to poroelastic coupling (Han and Dusseault, 2003; Walder and Nur, 1984).

Water-rock-interaction and reactive transport describe the formation, dissolution, and transformation of mineral phases, which lead to changes in the rock material properties (e.g. permeability and stiffness). In fractured geothermal reservoirs, hydrothermal alteration, as well as mineral reactions along the fracture surfaces can lead to a change of the effective aperture with increasing temporal scale (Li et al., 2008; Schmidt et al., 2017). While the dissolution of minerals can increase fracture permeability, the precipitation of secondary minerals decreases the expected fracture flow rate (Meller et al., 2014).

3.3 NUMERICAL UPSCALING

REV is the most common approach to upscale material properties in numerical modeling in heterogeneous (fractured) porous media, but it is not strictly correct due to the scale-invariance of fractures (Panfilov, 2000). It is better to refer to an equivalent grid-block, in which the material parameter is effectively averaged

over the whole block of interest (Guéguen et al., 2006). Other methods include numerical upscaling, asymptotic expansion as well as effective medium techniques including various deterministic or statistical approaches (Akber Hassan and Jiang, 2012; Cushman et al., 2002). However, all upscaling methods have two things in common: the analytical form of the coarse-scale equation and the way the associated parameters are determined in the coarse-scale model (Gerritsen and Durlofsky, 2005). Farmer (2002) introduces the term 'two-stage upscaling' and defines different groups of approaches, where the former stands for the local or global scale of the experiment and the latter for the calibration method.

3.3.1 *Local methods*

Local upscaling methods derive the equivalent rock property of a coarse grid block by the fine-scale results within the coarse model and provide reliable results especially for smooth parameter variations (Guéguen et al., 2006). Local-local methods include the physical measurement of local rock properties using laboratory and simulated experimental results and transferring them to the coarser grid-cell in larger meshes. By using independent experiments with different boundary conditions, the effective properties of a coarser grid cell can be defined numerically. For example, no-flow and sealed-side or flux boundary conditions can be used to determine the effective permeability tensor of a porous media (Hornung, 1997). A major disadvantage of this method is that these methods only provide exact results in the 1D case, whereas three-dimensional cases or discontinuities create large inaccuracies. Hou and Wu (1997) recommend numerical oversampling to increase accuracy. Local-global methods are rarely applied and use the global coarse-scale information (e.g. boundaries) for an extended local calculation of the material property (Akber Hassan and Jiang, 2012). Typically, these methods iterate between the upscaled properties and global variables until self-consistency is achieved (Chen et al., 2003).

3.3.2 *Global methods*

Global methods intend to solve the equations on the entire fine grid of the large-scale model and to estimate the boundary conditions which have to be applied on coarse grids (Guéguen et al., 2006). Global-local methods provide meaningful results if a good approximation to a solution for the entire global fine-scale model can be achieved. In practice, it represents a first approximation rather than a practical method (Farmer, 2002). Global-global methods are the computationally most demanding group of upscaling approaches. They try to minimize the difference between the fine and coarse solution by global functions (e.g. least-square fitting or global norms) (Christie and Blunt, 2001).

4

STOCHASTIC 3D NAVIER-STOKES FLOW IN SELF-AFFINE FRACTURE GEOMETRIES CONTROLLED BY ANISOTROPY AND CHANNELING

This chapter is published in Geophysical Research Letters 48.9, doi: 10.1029/2020GL092138.

ABSTRACT

This study presents a probabilistic analysis of 3D Navier-Stokes (NS) fluid flow through 30 randomly generated sheared fractures with equal roughness properties (Hurst exponent = 0.8). The results of numerous 3D NS realizations are compared with the highly simplified local cubic law (LCL) solutions regarding flow orientations and regimes. The transition between linear and nonlinear flow conditions cannot be described with a generally valid critical Reynolds number (Re_{crit}), but rather depends on the individual fracture's void geometry. Over 10 % reduction in flow is observed for increased global Re (> 100) due to the increasing impact of nonlinear conditions. Furthermore, the fracture geometry promotes flow anisotropy and the formation of channels. Flow perpendicular to the shearing leads to increased channeling and fluid flow ($\sim$ 40 % higher) compared to flow parallel to the shearing. In the latter case, dispersed flow and irregular flow paths cause a reduction of LCL validity.

PLAIN LANGUAGE SUMMARY

The movement of fluid and heat through fractured rocks is massively affected by the void space of the contributing fractures and the velocity of the fluid. The opposing offset of the two fracture surfaces creates complex and variable void geometries. A calculation of the expected flow rates is very difficult. In most studies, simplifications are adopted neglecting these complex features by using a plane surface and assuming that the flow is taking place smoothly. We therefore simulate the real flow using the three-dimensional fracture void space and compare the results with simpler two-dimensional models. It can be demonstrated that the difference between the two types of simulations depends not only on the local simplification but also on the flow direction within the fractures and that the difference increases with higher flow velocities. If the fractures are not considered as a whole continuum but on the local scale, preferential fluid pathways or channels are formed in which most of the flow takes place. Depending on the flow direction, channels are more or less pronounced. We can

show that in well-developed channels the differences between the calculation methods are much smaller than in the other parts of the domain.

4.1 INTRODUCTION

The investigation of fluid flow regimes in naturally fractured rock is crucial for assessing the performance of underground operations. While disposal of nuclear waste or tunnel construction aims for a tight subsurface (Tsang et al., 2015), highly permeable structures (e.g. fractures and faults) are essential for reservoir operations, such as enhanced oil recovery (Berkowitz, 2002) and geothermal energy production (Murphy et al., 1981). High flow velocities with Reynolds numbers (Re) > 10 can occur in these reservoirs, especially in fractures and near-wellbore areas (Kohl et al., 1997; Liu et al., 2016). The flow regime is controlled by the complexity of the internal fracture morphology (i.e. roughness) and the interaction and intersection of different fractures (structural complexity). Therefore, hydraulic quantification is typically resolved using simplified numerical approaches, e.g. assuming smooth parallel plates and linear flow laws (Egert et al., 2020).

The classical cubic law (CL) relationship assumes the fracture void space (aperture) as the volume confined by parallel plates (Witherspoon et al., 1980), whereas geological processes, such as shearing of rough opposing surfaces (Auradou et al., 2005) or mineral reactions (Schmidt et al., 2017), lead to laterally variable fracture apertures. The local cubic law (LCL) accounts for these heterogeneities in local aperture distribution and the resulting pressure gradients (Zimmerman and Bodvarsson, 1996). Since LCL is a cubic function of local apertures resulting from an arbitrary roughness distribution, the computed flow rate is highly sensitive to the proper definition of these apertures: an aperture vertical to the overall fracture plane is commonly used (Brown, 1989), while the effective aperture takes into account local surface tortuosity (Ge, 1997). Other authors proposed further modifications to account for different geometrical effects (Konzuk and Kueper, 2004; Wang et al., 2015). However, all LCL-based approaches still have two major limitations: a) the fracture is simplified to a 2D geometry (Marchand et al., 2020), and b) the Darcian-type LCL is assumed to be valid only for sub-laminar flow (Zimmerman et al., 2004). A critical Re (Re_{crit}) for considering nonlinear effects is under discussion and spans from < 1 to > 10 (Cunningham et al., 2020). The Navier-Stokes equations (NSE) provide a general basis to overcome these limitations and cover complex hydraulic conditions (linear and nonlinear) in the fracture, but due to their high computational effort, they are mainly for single fractures (Javadi et al., 2014; Li et al., 2016).

In the pre-stressed underground, the breaking up of intact rock and the subsequent shear displacement create highly variable fracture void spaces and introduce directionality into a previously non-directional geometric problem. Interconnected pathways of larger voids can form, which enable a higher flow and associated advective transport of solutes and heat in channels in the direction of the overall pressure gradient (Klepikova et al., 2020; Moreno and Tsang, 1994). Depending on the relative orientation of pressure gradient and stress field, these

channeling effects can either promote or reduce the fluid flow (Lang et al., 2018). The ratio of the flow between the two extreme cases, where the flow is oriented perpendicular or parallel to the shearing, is called flow anisotropy (FA) (Auradou et al., 2006). Besides laboratory experiments (Gentier et al., 1997; Rasmuson and Neretnieks, 1986), FA was also investigated numerically (Koyama et al., 2006; Mallikamas and Rajaram, 2005; Marchand et al., 2020). Investigations were mostly limited to linear flow conditions, while nonlinear effects were only briefly addressed (Liu et al., 2020). To the authors' knowledge, no study has investigated the role of shear-dependent and flow rate-dependent channeling processes in a statistically relevant set of fractures and concerning the validity of the LCL. A quantitative analysis of the prevailing processes can only be performed in a spatially resolved manner.

The primary goal of this stochastic study is to assess the individual flow and surface effects causing the overestimation of the LCL and flow anisotropy. Particular attention is paid to the formation of channels and their dynamic changes during the transition to nonlinear flow regimes. For this purpose, 840 individual realizations (30 fractures, 7 pressure gradients, 2 flow laws, and 2 directions) are simulated, and local differences between the fully 3D Navier-Stokes and 2D local cubic law solutions are quantified in terms of local flow rate and velocity. The significant number of individual fractures can be used to infer the range of uncertainty in large-scale reservoir models.

4.2 METHODOLOGY

4.2.1 *Rough surface and sheared fracture generation*

A fracture surface can be created either by scanning a real surface or by numerically generating surface morphologies represented by fractal geometries following self-affine properties with isotropic correlation functions (Brown, 1995). In this study, a set of 30 random unique surfaces with a granite-typical Hurst roughness exponent of $H = 0.8$ (Schmittbuhl et al., 1993) are created using the workflow described by Méheust and Schmittbuhl (2001). The generated surfaces have a resolution of 128×128 nodes corresponding to a size of 20×20 cm to guarantee high accuracy with reasonable computational effort. The maximum surface amplitude is limited to 30 mm. Shearing is introduced by offsetting the fracture upper surface by one row of nodes in x-direction causing a sliding-up (Auradou et al., 2006). Maintaining at least one contact point results in a locally varying inter-surface void space (Figure 4.1a). In order to focus on the impact of the complex void geometry on channeling processes, mechanical effects, such as fracture frictional behavior or deformation of the void space, which can alter the local flow regime (Blöcher et al., 2019) and induce further uncertainties, are neglected.

While the resulting 3D fracture void geometry will be directly transformed into a 3D mesh for the Navier-Stokes simulations, it is reduced to a 2D mesh for the LCL model including calculated local apertures. For the modeling presented here, an aperture distribution is used which has neither directional nor direct

roughness dependencies. Following the approach of Ge (1997), an effective aperture a_{eff} is calculated, which is the distance between the bottom and top surfaces as surface normal to the local middle plane.

4.2.2 *Governing equations*

Incompressible and steady-state fluid flow is governed by the Navier-Stokes equations (Bear and Cheng, 2010):

$$\rho(\boldsymbol{u} \cdot \nabla)\boldsymbol{u} = -\nabla P + \mu \nabla^2 \boldsymbol{u} + \boldsymbol{f} \tag{4.1}$$

$$\nabla \cdot \boldsymbol{u} = 0 \tag{4.2}$$

where ρ, P, $\boldsymbol{u}$, $\boldsymbol{f}$, and μ denote the fluid density, the total pressure, the velocity, and body force vector (e.g. the gravitational acceleration), and the dynamic fluid viscosity, respectively. For 3D problems, the equations form a set of four fully coupled partial differential equations solved for local pressure and velocity components. A simplified solution is to assume linear flow conditions and neglect the nonlinear inertia forces leading to the LCL (Nicholl et al., 1999):

$$\nabla(\frac{a_i^3}{12\mu})\nabla P = 0 \tag{4.3}$$

where a_i is the local aperture.

4.2.3 *Numerical modeling*

The numerical simulations (LCL and NS) are carried out with the finite element open-source application TIGER (THMC sImulator for Geoscience Research) (Gholami Korzani et al., 2020). The code is based on the MOOSE framework (Permann et al., 2020) and designed for solving thermo-hydraulic-mechanical-solute transport problems in geothermal reservoirs at different scales and dimensions. For the LCL simulations, an XY-extended FE mesh is used, which consists of four-node quadrilateral elements. The local effective aperture is represented as spatial-dependent material property. Nonlinear flow is realized via the Navier-Stokes module (Peterson et al., 2018). The simulations are performed using a structured 3D FE Mesh consisting of $127 \times 127 \times 10$ hexahedrons created using Gmsh (Geuzaine and Remacle, 2017). Pressure-stabilized Petrov-Galerkin stabilization is applied to the equal-order elements for directly solving the PDEs. Top and bottom surfaces of the 30 unique fractures are transferred to a base mesh in such a way that it reflects their natural rough-walled and sheared fractures. A mesh sensitivity analysis was performed to avoid uncertainties regarding the discretization.

The further parameterization is done similarly for both kinds of simulations. A constant pressure of $0.01, 0.1, 1, 5, 10, 20$, and $50\,\mathrm{Pa}$ is applied to the inlet

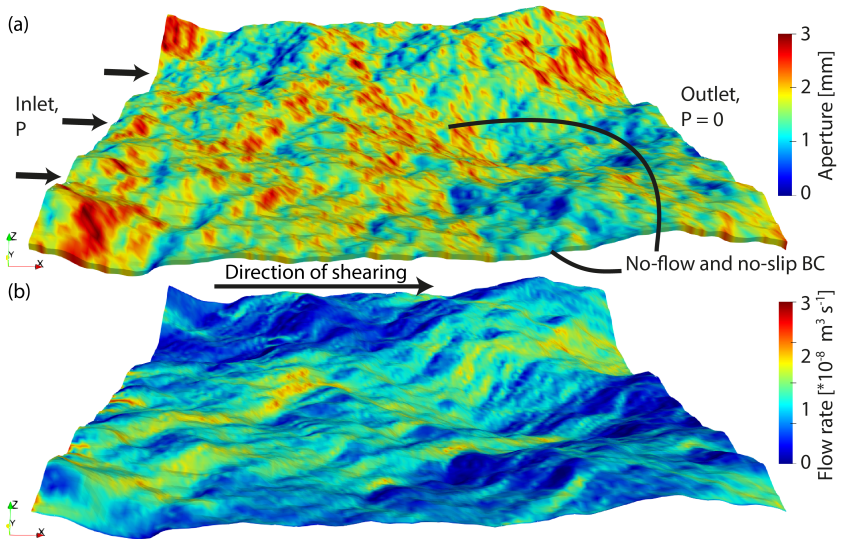

Figure 4.1: a) Calculated vertical apertures projected onto the resulting 3D fracture void space. The boundary conditions and the direction of shearing are shown. b) Flow rates for a realization with a boundary pressure of 10 Pa and flow parallel to the shearing. Flow is rather localized in distinct channels.

boundary in the direction of flow, while the outlet boundary is fixed to zero pressure. Elsewhere no-slip boundary conditions are applied. Fluid density and viscosity are set constant at 10^3 kg m^{-3} and 10^{-3} Pa s, respectively. All simulations are carried out for the two flow laws (LCL and NS) and the extreme cases of an overall pressure gradient parallel and perpendicular to the shearing, leading to a total of 840 realizations.

4.3 RESULTS

4.3.1 *Fracture flow*

The fluid flow in the NS simulations is evaluated at each fractures' outlet to be able to consider both small-scale local disturbances as well as fracture-wide flow effects. The results outlet flow rates Q_{NS} are obtained from the mean velocities multiplied by the cross-sectional areas and are shown as a function of the mean vertical fracture apertures $\overline{a}$ in Figure 4.2. Since the surface generation algorithm imposes a Gaussian roughness distribution the mean apertures $\overline{a}$ range between 1.2 and 2.5 mm with an accumulation of around 1.7 mm. For flow parallel to the shearing (red colors), Q_{NS} and Re match a cubic trend ($Q_{NS} \in \overline{a}^3$) which agrees with the observations of Witherspoon et al. (1980), while for flow perpendicular to the shearing (blue colors), increasing pressure gradients cause deviation from the cubic trend. $Re = 220$ and $Q_{NS} = 4.4 \times 10^{-5}$ m^3 s^{-1} are reached for maximum simulated pressure gradients of 250 Pa m^{-1}. In the case of flow perpendicular to the shearing, the determined flow rate is higher for all cases with a mean $FA = 1.44(\pm 0.14)$ (Figure 4.2b).

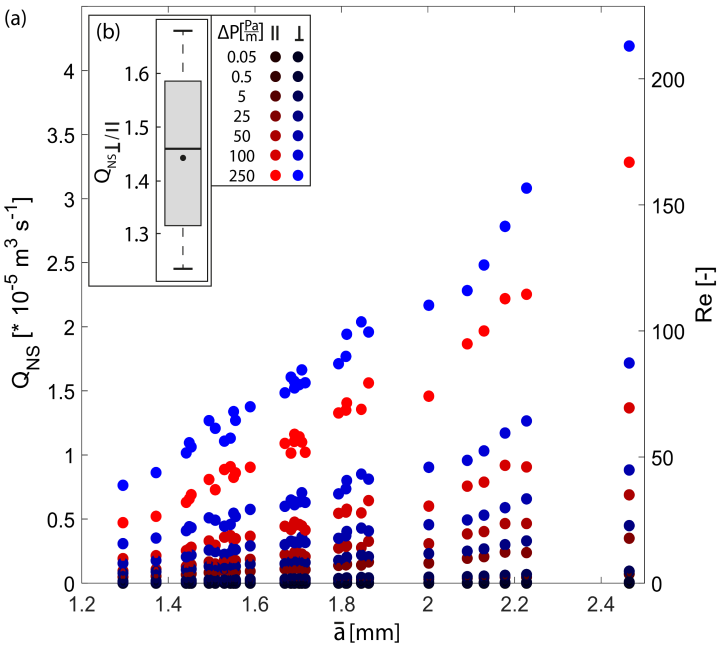

Figure 4.2: a) Q_{NS} and Re as function of $\bar{a}$. Each column represents one of the 30 unique fracture geometries. Red colors indicate $\parallel$ and blue $\perp$-flow to the shearing direction, and lighter colors indicate larger pressure gradients. b) Boxplot of the FA.

4.3.2 *The transition from linear to nonlinear flow*

The nonlinear effects along the fracture plane are analyzed by comparing the normalized flow rate $Q_{NS}normalized$ (Figure 4.3a):

$$Q_{NS}normalized = \frac{\frac{Q_{NS}}{\Delta P}}{(\frac{Q_{NS}}{\Delta P})_{Re\sim 0}} \tag{4.4}$$

where ΔP is the global pressure gradient. Nonlinear effects arise at $Re > 1$, while at $Re = 100$, they already lead to a decrease of flow by $5\,\% - 10\,\%$, correlating well with the findings of Brush and Thomson (2003). The dispersion of the results increases strongly with increasing nonlinearity, especially for the parallel case.

In addition to the nonlinear effects, LCL and NS solutions already differ initially in laminar conditions (Figure 4.3b). For flow parallel to the shearing, the initial bulk overestimation of the LCL is about $9\,\% - 19\,\%$, which is consistent with previous observations (Al-Yaarubi et al., 2005; Nicholl et al., 1999). For flow perpendicular to the shearing, the mean overestimation is around $1\,\% - 9\,\%$. The significant differences between the NS simulations are the consequence of the extended travel distance between inlet and outlet (of more than 10 %), which leads to reduced local pressure gradients and enhances the anisotropy compared to pure LCL investigations (Marchand et al., 2020).

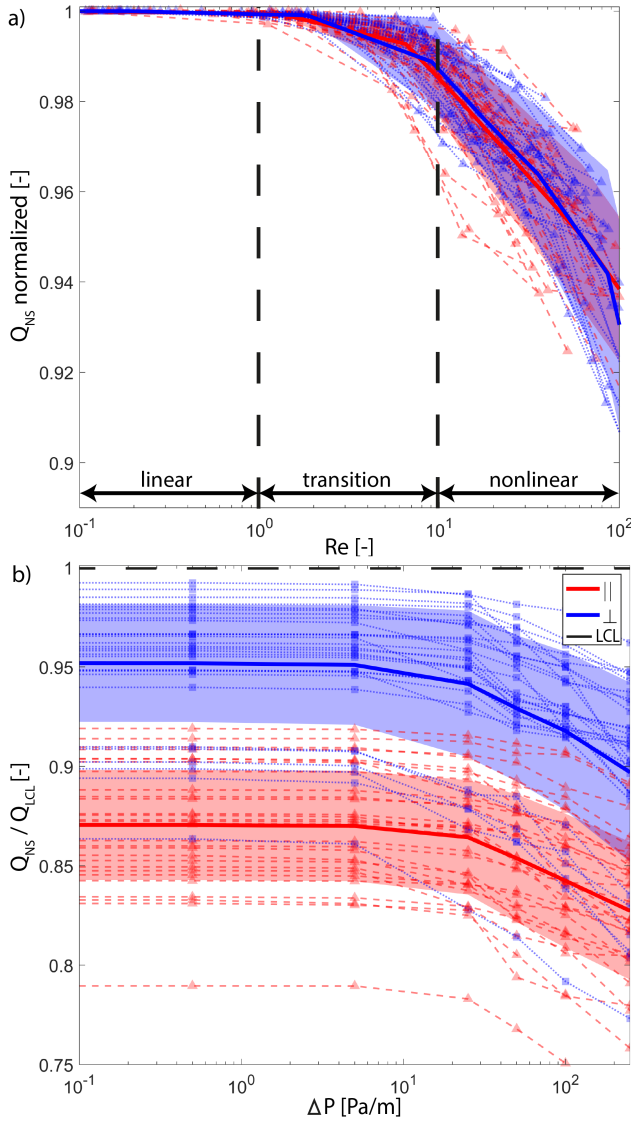

Figure 4.3: Comparison of the Navier-Stokes realizations flow rates to a) the flow rate with $Re \sim 0$ b) the LCL. Red indicates $\|$-flow and blue $\perp$-flow. Individual results are plotted as well as the mean value at each ΔP and the 95 %-confidence intervals. All NS realizations show a reduced flow rate compared to LCL and increasing nonlinear effects starting from $Re = 1$.

In Figures 4.2 and 4.3, the results are evaluated as the sum of the total flow through the fracture geometry, while Figure 4.1b depicts a fluid flow that is concentrated on small-scale fluid pathways. For further evaluation of the local validity of the LCL, we identify and separately analyze two flow domains, the channel sweeping domain, where the flow is concentrated in channels, and the surface sweeping domain, where a more dispersed flow is prevailing in off-channel areas.

4.4 DISCUSSION

4.4.1 *Channel identification*

Channels are defined as continuous spatial features where large portions of the entire domain flux are concentrated. Various approaches have been developed to compare the extent of channeling using the LCL-based flow and effective permeability either deterministically (Watanabe and Kolditz, 2015) or statistically (Le Goc et al., 2010; Moreno and Tsang, 1994). However, given the linear relationship Q and ΔP, these LCL-based studies cannot account for locally increasing nonlinear effects and resulting changes in the extent and localization of channeling within an individual fracture geometry. Within the scope of the present work, we tested several variables (e.g. aperture and velocity) and thresholds (e.g. 50 and 75 % of the total flow) for their applicability to different fractures and pressure gradients. Inspired by the study of Knudby and Carrera (2005), flow paths are identified as channels where the upper quartile of the flow rate is localized. Subsequently, the effects of channeling are compared over a large number of realizations.

Based on the previously defined frameworks, a multi-stage post-processing concept is developed to identify and later quantify the individual channels within the studied realizations using MATLAB and the results of the NS simulations (Figure 4.1). Channel identification is an iterative process. All nodes are sorted in descending order in terms of their local flow rate. Starting from the highest flow rate, channel nodes are marked and their nodal flow rates are added up until 25 % of the mesh's entire flow is localized within channels. Subsequently, the skeletonized channel network is extracted and further evaluated for its connectivity. The connectivity is checked by setting up a 3×5 nodes sampling window in the direction of the pressure gradient, which assigns nodes with two or more connections to a unique channel. Since channels are defined as a coherent and continuous structure, background noise, and poorly connected nodes (node row of less than 10 % of the mesh side-length) are removed (Figure 4.4).

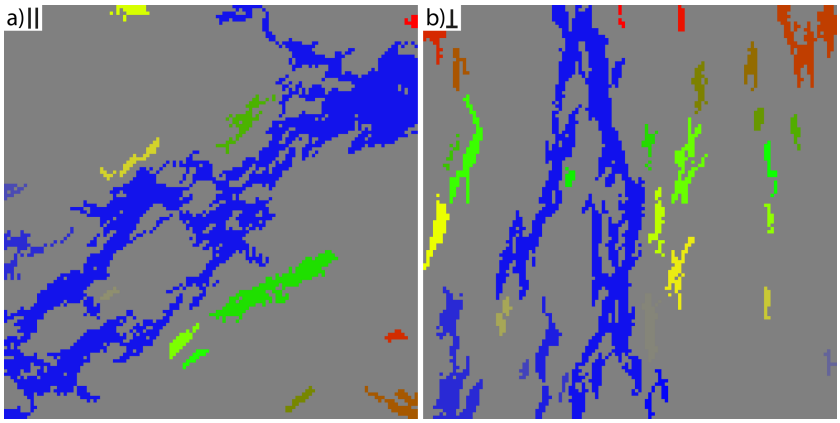

Figure 4.4: The identified channels, for shearing in x-direction and a) ||-flow, the realization is identical with Figure 4.1 and b) ⊥-flow. Each color corresponds to a single identified channel.

Figure 4.4 exemplifies the identified channels and resulting flow characteristics for the two extreme cases of flow parallel (Figure 4.4a) and perpendicular (Figure 4.4b) to shearing. A perpendicular orientation of shearing and flow leads to strong localization and formation of well-connected and continuous channels. In contrast, flow parallel to the shearing causes less localization and poorer connectivity characterized by high velocities in these regions and significantly increased flow impedance (Auradou et al., 2006). The resulting FA is more pronounced for smaller $\overline{a}$, as the probability of well-connected channels in the parallel extreme case increases with larger $\overline{a}$.

4.4.2 *Spatial assessment of the LCL accuracy*

The LCL with a local effective aperture is one of the most common flow laws adopted for computing fractured rock hydraulics. Nevertheless, its applicability is often determined at the fractures' outlet, leading to the conservative conclusion that the LCL is only valid for $Re \ll 1$. However, the presented analyses show that the local Re can vary within one order of magnitude for a single realization depending on whether the local Re is calculated within or off a channel. Therefore, the global error is broken down into a local error, which is mathematically described by:

$$\delta(x,y) = \frac{Q_{NS}(x,y) - Q_{LCL}(x,y)}{Q_{NS}(x,y)} \tag{4.5}$$

where $Q_{NS}(x,y)$ and $Q_{LCL}(x,y)$ are the volumetric flow rate calculated with the NSE and LCL, respectively. The volumetric flow rate is obtained from the mean velocity multiplied by the crossectional area.

In Figures 4.5a and 4.5b, the relative errors are shown as a function of the local Re for one individual realization considering flow parallel and perpendicular to the shearing. The mean error increases nonlinearly towards low flow rates and small apertures, indicating that the aperture correction according to Ge (1997) has a higher validity in channeled structures, while surface effects cause significantly increased local errors. In the identified channels (high Q and Re) the local error is negligibly small so that LCL and NS predict the same local flow rate. The small-scale results show a slight directional dependence on the overall trends. The mean error for flow perpendicular to the shearing is reduced and single nodes even show an underestimation by the LCL.

A similar picture emerges if this analysis is extended for a significant number of different fractures and pressure gradients. Based on statistically identical surfaces (same Hurst roughness exponent and shearing) the differences between NS and LCL are quantified in terms of their uncertainties and variability with respect to the tectonic setting. While the differences in the identified channels remain constant, it increases significantly for the surface sweeping areas with increasing pressure gradients, and the stronger local nonlinearity results in an increased overall error (Figures 4.5c and 4.5d). Channeling thus becomes more pronounced with increasing flow rate. Since inertial effects are prevalent for surface sweeping, less void space is required to localize 25 % of the entire domain

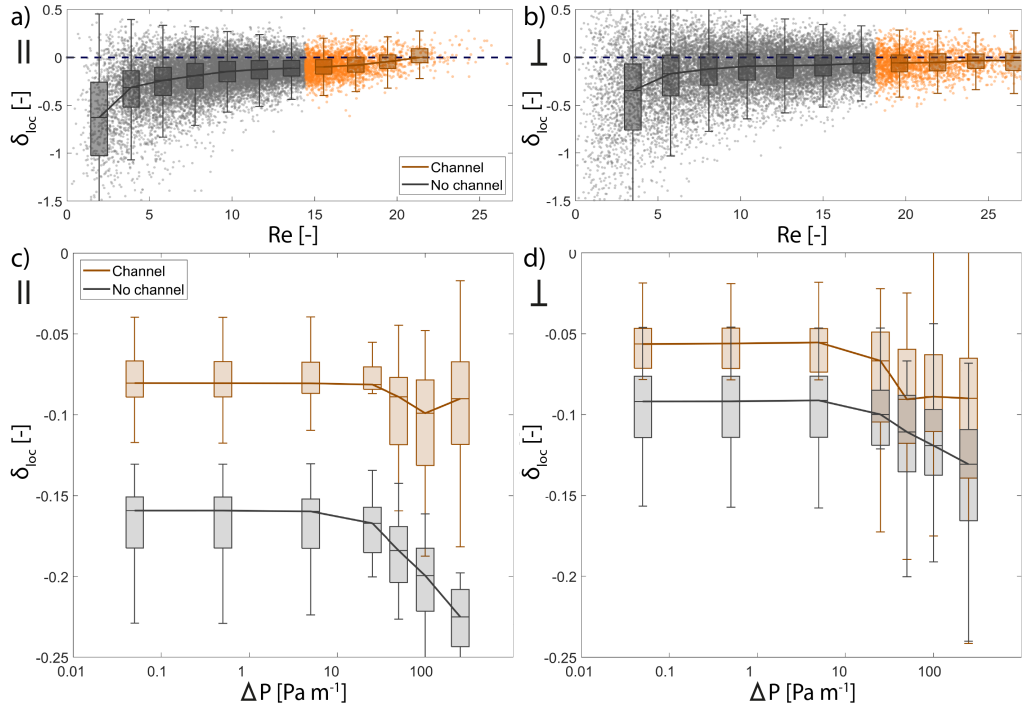

Figure 4.5: Top: Relative error plotted against the Re for the individual nodes of a single realization for a) $\|$-flow (same as Figures 4.1 and 4.4) and b) $\perp$-flow with a $\Delta P = 50\,\mathrm{Pa\,m^{-1}}$. Orange indicates the identified channel nodes. Bottom: c) and d) Median of the relative error plotted for all realizations as a function of ΔP. Orange indicates channels while grey represents the error located in the surface regions. The identified channels generally tend to have less difference between local cubic law (LCL) and Navier-Stokes (NS) and fewer nonlinear effects (values closer to 0).

flow. For higher Q and Re, the overall results tend to show higher variability and standard deviation.

The described differences, both purely laminar and incipient nonlinearity, can be traced back to the internal velocity field. In the channel sweeping, a parabolic shape is maintained, i.e., the basic assumption of the LCL, while it deviates significantly from this ideal shape for the surface sweeping domains. Here, complex internal void geometries such as contact spots, asperities, and local roughness cause transverse flows, eddy currents, or stagnant water zones that simply cannot be considered in 2D fracture models (Zou et al., 2017). Cunningham et al. (2020) showed experimentally on a mated fracture that the Re_{crit} to consider nonlinear effects decreases with increasing local complexity of the fracture void geometry. Thus, both decreasing apertures and an increase in relative aperture fluctuations cause enhanced inertial effects. Our realizations confirm the presented relationship between Re_{crit} and relative surface roughness.

Transferred to sheared fractures and resulting anisotropic flow, a parallel orientation of shearing and flow favors the formation of irregular and highly tortuous channels with increased viscous friction. This process causes both, a decrease in the observed flow rate and an increased sensitivity to nonlinear effects (reduced Re_{crit}). In contrast, with a perpendicular orientation of shearing

and flow, well-developed and smooth channels result in reduced geometry dependence with significantly higher LCL accuracy and reduced nonlinear effects at the same flow rate. In such a complex environment (in terms of individual geometry and internal flow field), it is therefore difficult to introduce a generally valid correction factor for the LCL and growing nonlinearities, as described for example by Wang et al. (2020) or used in the well-known Forchheimer equation (Chen et al., 2015). However, with respect to geothermal reservoirs, this also implies that a typical normal stress regime, with vertically oriented and displaced fracture surfaces, favors the formation of channel sweeping for horizontal flow between two wells (Lang et al., 2018). Strong channeling increases the range of validity of the LCL at higher Re ($< 10\,\%$ deviation for $Re \sim 100$) but could cause reduced effective heat exchange within the reservoir (Guo et al., 2016). An additional strike-slip component would however lead to more dispersed surface sweeping and thus reduces the reliability of LCL predictions.

4.5 CONCLUSION

Originally focused on the impact of higher Re on flow through self-affine fracture geometries under various shear displacements, our stochastic analysis of 3D Navier-Stokes flow reveals the importance of local complexity on the spatial validity of the LCL and explains contradicting observations of different studies. In fracture void geometries, the definition of a single critical Re (e.g. $Re_{crit} = 1$) is not sufficient to describe the flow regime and associated processes; an additional spatial analysis is crucial. The initial Gaussian aperture distribution is not reflected in the local flow regimes; instead, the character of the flow could vary between the two extreme cases, a rather focused channel sweeping or a rather dispersed surface sweeping, resulting from the orientation of flow and shearing. Channel sweeping, typically favored by flow perpendicular to the shearing, is characterized by highly localized channels with an ideal parabolic velocity field. A weak dependence on the relative roughness and tortuosity of the fracture results in accurate LCL prediction ($< 10\,\%$ overestimation) and mostly linear flow occurring even at $Re \sim 100$. In contrast, local geometrical complexity in the dispersed surface sweeping entails increased frictional and inertial effects resulting in increasing differences between NSE and LCL ($> 15\,\%$). The small-scale stochastic nature of our study allows us to infer the range of uncertainty in large-scale fluid flow phenomena.

ACKNOWLEDGMENTS

This study is part of the Helmholtz topic 'Geothermal Energy Systems' in the program 'Renewable Energies'. We thank the EnBW Energie Baden-Württemberg AG for supporting geothermal research at KIT and the 'Deutsche Forschungsgemeinschaft' (DFG) for granting the 'F4aT'-project (grant: INST121384/201 − 1). We acknowledge support by the KIT-Publication Fund of the Karlsruhe Institute of Technology. The authors would like to thank the editor and the two anonymous reviewers for their constructive comments. Publicly available software is

used to generate the individual surfaces and fracture geometries and to perform the numerical simulations. The algorithm for generating the rough surfaces is explained in Méheust and Schmittbuhl (2001). The numerical simulations are carried out using the MOOSE-based (Permann et al., 2020) open-source simulator TIGER (Gholami Korzani et al., 2020) and can be reproduced using the parametrization provided in the methodology section. Exemplary results of a Navier-Stokes realization (as shown in Figure 4.1), with the corresponding input file can be accessed through: http://doi.org/10.5281/zenodo.4621333.

5

SPATIAL CHARACTERIZATION OF CHANNELING PROCESSES IN SELF-AFFINE ROUGH-WALLED FRACTURES IN THE TRANSITION TO A NONLINEAR FLOW REGIME

This Chapter is in preparation for submission.

ABSTRACT

Quantifying spatially resolved fluid flow in fractures is of crucial importance for the successful reservoir development, e.g. in Enhanced Geothermal Systems. In this study, a workflow for modeling and characterizing preferential flow paths in rough-walled shear fractures is proposed. A set of 30 rough-walled self-affine fractures with identical roughness (Hurst exponent $= 0.8$) is stochastically generated. 420 realizations of the flow modeling are performed employing the nonlinear Navier-Stokes equations (NSE) and a set of boundary conditions capturing the transition from linear to nonlinear flow regimes. Moreover, the consideration of two extreme cases of flow directions, perpendicular as well as parallel to the shearing, allows us to provide information on fractured reservoirs. The particularity of this approach is the combined statistical analysis of the geometry and transport properties of fluid paths in the three-dimensional fractured void space under typical geothermal flow conditions. In a perpendicular orientation of flow and shearing, large portions of the volume flow rate are localized in a few well-formed channels. In contrast, parallel to the shearing, a complex pattern of individual tortuous channels develop and larger parts of the fracture domain are subject to active flow. Increasing nonlinear effects are seen primarily outside these channels, suggesting that anomalous flow may prevail in irregular fracture structures (e.g., contact areas or asperities). In the parallel case, this leads to an enhancement of channeling processes resulting in less affected volume and a shortening of the main flow path, while in a perpendicular orientation nonlinear effects are only of minor importance. The small-scale flow regime of both extreme cases tends to converge with increasing flow rate.

5.1 INTRODUCTION

Hydraulic properties of naturally fractured rocks are of key importance for assessing the performance of various kinds' geologic-related projects. Applications such as the disposal of nuclear waste or tunnel construction aim for low fluid flow and thus low permeabilities (Tsang et al., 2015). On the other hand, high

flow rates and permeabilities are of crucial importance for many applications, such as enhanced oil recovery (Berkowitz, 2002) or geothermal energy production (Murphy et al., 1981). However, since existing fractures rarely allow the necessary flow rates by nature, permeability is enhanced by thermal, hydraulic, or chemical stimulation (Evans, 2005; Schill et al., 2017). The resulting Enhanced Geothermal Systems (EGS) form complex systems of faults and fractures with resulting complex hydraulic behavior that can only be represented in a limited and simplified way in geological and numerical models (Sausse et al., 2010). It is, therefore, all the more important to represent both the individual structures and the fluid flow with a high degree of accuracy in numerical modeling to be able to make statements about the heat exchange surface, solute transport as well as mineral solutions and precipitation (Egert et al., 2021a).

In contrast, the fluid flow in large-scale fracture models is often represented by highly simplified assumptions. The most common approach, cubic law (CL), assumes fractures as smooth parallel plates with a constant void space in between (Witherspoon et al., 1980). The local cubic law (LCL) accounts for local void space changes but raises the uncertainty of the aperture calculation (Zimmerman and Bodvarsson, 1996). Common approaches assume an aperture perpendicular to the overall (Brown, 1989) or local fracture middle plane (Ge, 1997) or empirically account for roughness effects (Cheng et al., 2020; Konzuk and Kueper, 2004). All LCL-based models introduce two types of uncertainties. First, the fracture geometry is reduced to 2D, causing an underestimation of geometrically induced flow effects. Secondly, the Darcian-type LCL is only valid for laminar flow and low Reynolds numbers ($Re \ll 1$) (Brush and Thomson, 2003; Zimmerman et al., 2004). Both limitations pose problems for the analysis of high-resolution fluid flow e.g. in karstified systems (Lloyd et al., 1996) or fractured reservoirs during geothermal energy production and stimulation (Chen et al., 2015; Kohl et al., 1997). The solution of the nonlinear Navier-Stokes equations (NSE) allows to circumvent these limitations, but they are rarely used due to high computational complexity (Al-Yaarubi et al., 2005; Javadi et al., 2010; Liu et al., 2020). Egert et al. (2021b) were able to demonstrate the need for solving the NSE to consider both the three-dimensional fracture void space and growing nonlinear effects in the small-scale fracture-internal flow field by comparing NSE and LCL. This small-scale flow field is not homogeneously distributed, but rather preferential fluid pathways or channels form within fracture geometries, resulting in a spatially varying coincidence between the two flow laws.

These preferential fluid pathways are the results of two processes taking place in the earth's crust. Tectonic stresses lead to the formation of new fractures as well as the shearing of existing opposing surfaces. Hydrothermal alteration and mineral reactions lead to variable filling in the fracture (Meller et al., 2014). Both processes create more or less connected void spaces both within these fracture networks and along with individual fractures, where fluids can flow more easily in the direction of the pressure gradient (Moreno and Tsang, 1994). The effect is generally known as channeling and defined as the spatial concentration of fluid flow along preferential hydraulic pathways over long distances through geologic systems with heterogeneous internal structure (Tsang and Tsang, 1987). It has been observed in small-scale laboratory experiments on individual surfaces

(Auradou et al., 2006) and also in field-scale fracture networks (Guihéneuf et al., 2017; Tsang and Neretnieks, 1998). As a result, both geometric and transport properties are no longer generally valid for the entire fracture domain but must be determined for these networks of individual channels. This concerns not only the channel length and width but also the flow-wetted surface, flow-through volume, and solute mixing processes (Figueiredo et al., 2016). Different approaches have been developed to characterize the extent of channeling in experiments (Klepikova et al., 2020) or numerically (Watanabe et al., 2015).

Numerically, these approaches focus either on the geometric and statistical description of the channeling processes or the effects on the flow-related transport in various spatial scales (Renard and Allard, 2013). Ronayne et al. (2008) inverted for the statistical properties of an aquifer-system taking into account channeling. Maillot et al. (2016) evaluated the connectivity of channels in a discrete fracture network. Le Goc et al. (2010) uses effective permeabilities and momentum analysis for the stochastic description of channel distributions on different mathematically-generated aperture fields and 2D discrete fracture networks. Knudby and Carrera (2005) compared several statistical-, flow- and transport-related indicators for their applicability to identify the connectivity of channels on a single surface. Bruderer-Weng et al. (2004) analyzed the multifractal spectrum of the flow field to quantify the effect of channeling on the dispersion of tracer. Marchand et al. (2020) evaluated the geometrical properties of channels with respect to the shear displacements of the opposing fracture surfaces. Tang et al. (2019) evaluated the channeling characteristics and transport-related properties in pore-scale heterogeneous media. In this way, several different indicators and approaches have been investigated, with all studies being limited to simple and planar 2D geometries, small flow rates, and linear flow laws. The importance of nonlinear and geometric effects concerning channeling has been addressed (Liu et al., 2020; Siena et al., 2019), but has not been further investigated so far.

As a consequence of the formation of preferential fluid pathways, flow anisotropy arises, which describes the ratio of the volume flow when a fracture has flowed through parallel or perpendicular to the shearing direction (Auradou et al., 2001). Besides laboratory experiments (Gentier et al., 1997; Rasmuson and Neretnieks, 1986), flow anisotropy was also investigated numerically. The direct link between the effect of channeling and flow anisotropy could be confirmed in small-scale experiments (Silliman, 1989) and numerically at the reservoir scale with respect to the local stress field (Lang et al., 2018). However, it has not yet been investigated how the geometric properties (e.g., volume, area, connectivity) of these channels can be quantified in the three-dimensional void geometry and how these channel characteristics change in the transition from laminar to turbulent flow conditions and with respect to the extreme cases described as flow anisotropy.

The objective of the current study is therefore to design a universally applicable workflow concerning the identification and quantification of small-scale fluid pathways in the fracture void space. Furthermore, the extent of the channeling processes regarding different flow constraints, e.g. pressure gradient and flow directions, is quantified, and the effects on heat and solute transport are discussed. In a first step, a variety of unique rough surfaces are created and

subsequently sheared to generate fractures. Then, the local flow field within the three-dimensional fractures is determined by directly solving the Navier-Stokes equations and considering different flow boundary conditions and directions. Using a multi-stage workflow, the individual channels are identified, and suitable indicators are presented to describe the geometrical as well as flow- and transport-related characteristics in the transition from laminar to turbulent flow regime. Finally, the application of the workflow and the different channeling indicators to the large number of unique fractures and realizations allows an upscaling of the knowledge gained here to effective properties of fractured geothermal reservoirs.

5.2 METHODOLOGY

5.2.1 *Sheared fracture generation*

A large number of statistically generated and unique fracture geometries are required for probabilistic determination of the different channel characteristics. The individual surface can be described either by scanning a real fracture surface or by numerically generating surfaces following mathematical functions (Brown et al., 1995). In the study presented, it is assumed that the fracture surfaces can be represented by fractal geometries that follow self-affine properties with isotropic correlation functions (Méheust and Schmittbuhl, 2001). The probability density function p_d is defined as:

$$p_d(\Delta h, \Delta \boldsymbol{r}) = \lambda^H p_d(\lambda^H \Delta h, \lambda \Delta \boldsymbol{r}) \tag{5.1}$$

where λ is an arbitrary scaling factor, H is the Hurst roughness exponent, Δh and $\Delta \boldsymbol{r}$ are the difference in height and distance respectively (Méheust and Schmittbuhl, 2001). Every generated surface is unique, as each is based on a distribution extracted from a white noise generator. A roughness exponent of $H = 0.8$ is used (Figure 5.1), which is often observed for natural fractures in granitic rock (Schmittbuhl et al., 1993). The generated rough surfaces have a resolution (m x n) of 128×128 nodes resulting in a size of 20×20 cm and a total node number N of 16 384. The maximum surface amplitude is limited to 3 cm. A total of 30 different surfaces are generated and analyzed to obtain statistically reliable results.

In the geothermal context, freshly fractured surfaces with well-connected void space and good hydraulic conductivity are of interest. These voids are created when initially well-mated fracture surfaces are sheared against each other under natural or artificially-induced tectonically stresses (Egert et al., 2018). To introduce this shearing into the numerical models, the rough surface is doubled. The lower surface is fixed, and the upper surface is raised and horizontally displaced by one row of nodes. The upper surface is lowered until at least one contact point between the two opposing surfaces is established, leading to a locally varying void space. The shear displacement is considered small compared to the entire fracture length ($< 1\,\%$) and no deformation or

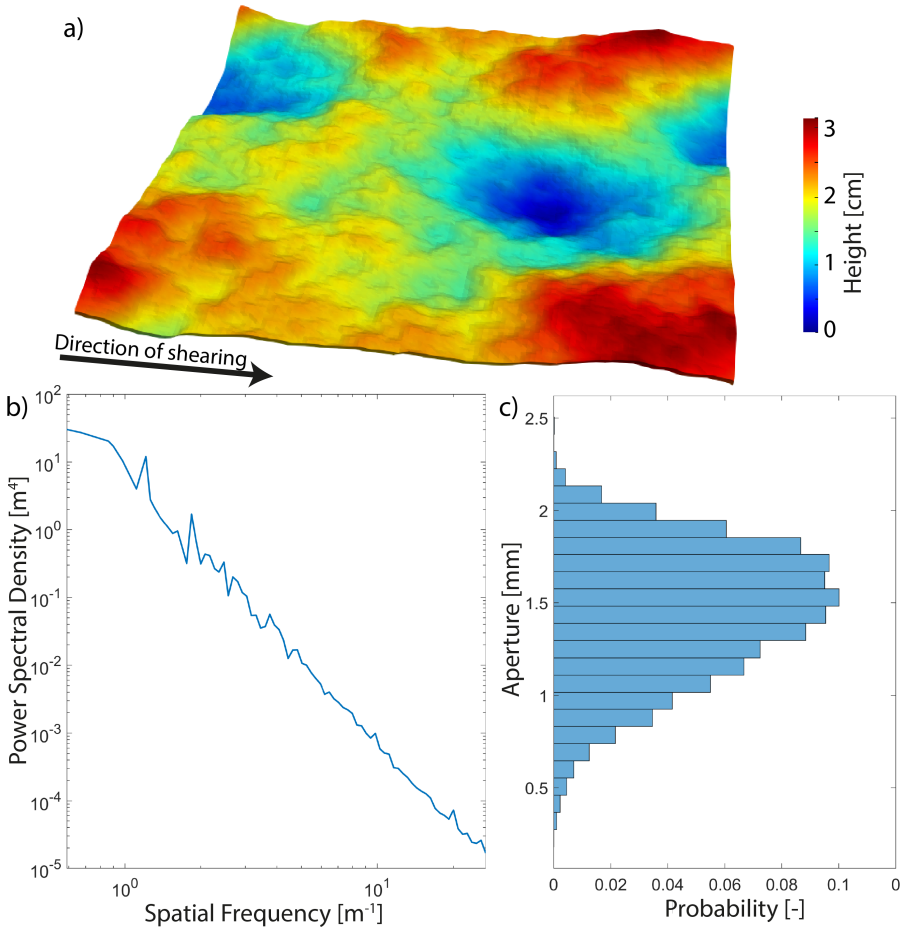

Figure 5.1: a) Example of a generated fracture after shearing and lowering. The surface roughness exponent $H = 0.8$ and the upper surface is sheared to the right. b) Power spectral density of the surface topography; c) Boxplot of the effective aperture for the shown fracture.

rotation is assumed, as the study investigates the nonlinear effects on the channel formation in a developing fracture in the space of rigid approximation.

While the resulting three-dimensional rough-walled fractures can be used for the NS simulations, an aperture must be calculated to transfer the resulting velocities into a volumetric flow rate and to be able to apply the LCL. Since a mechanical or vertical aperture a_{vert} leads to an overestimation of the flow rates (Wang et al., 2015), the effective aperture a_{eff} is introduced (Ge, 1997). To gain a_{eff}, the local median $m(x, y)$ is established and the median curve has to be calculated as follows:

$$m(x, y) = \frac{h_{bot}(x, y) + h_{bot}(x, y)}{2} \tag{5.2}$$

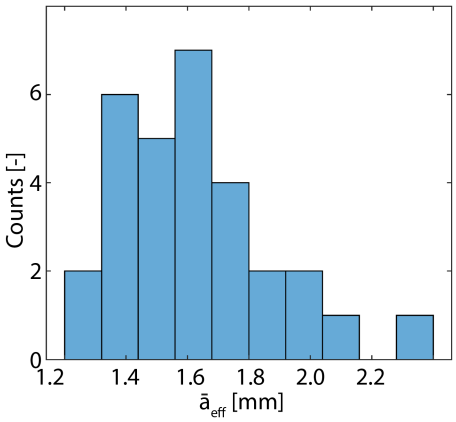

Figure 5.2: Mean effective aperture distribution of the 30 rough-walled fractures.

where $h_{bot}(x,y)$ and $h_{top}(x,y)$ denote the height of the local bottom and top surface. Subsequently, the slope of the local median plane $\boldsymbol{\nabla m(x,y)}$ is calculated and the normal vector $\boldsymbol{n(m)}$ can be obtained:

$$\boldsymbol{\nabla m(x,y)} = \begin{pmatrix} \frac{m(x+1,y)+m(x-1,y)}{2\Delta x} \\ \frac{m(x,y+1)+m(x,y-1)}{2\Delta y} \\ 0 \end{pmatrix} = \begin{pmatrix} m_x \\ m_y \\ 0 \end{pmatrix} \tag{5.3}$$

$$\boldsymbol{n(m)} = \begin{pmatrix} m_x \\ 0 \\ m_y \end{pmatrix} \tag{5.4}$$

The effective aperture a_{eff} is defined as the distance of h_{bot} and h_{top} intersecting the point $m(x,y)$ and using the normal vector $\boldsymbol{n(m)}$:

$$a_{eff}(x,y) = dist(BT) \tag{5.5}$$

where B and T denote the intersection of the bottom and top surface with $\boldsymbol{n(m)}$(Figure 5.1). a_{eff} range between 0 and 3 mm and are slightly reduced compared to a_{vert}. The mean aperture $\overline{a}_{eff}$ is calculated to compare across the different meshes and to compute the variability in the local aperture distribution. Figure 5.2 shows that $\overline{a}_{eff}$ ranges between 1.2 and 2 mm, with some outliers to higher mean apertures.

5.2.2 *Flow governing equations*

Incompressible and steady-state fluid flow is governed by the Navier-Stokes equations (NSE) and the mass conservation equation (Bear and Cheng, 2010):

$$\rho(\boldsymbol{u}\nabla)\boldsymbol{u} = -\nabla P + \mu\nabla^2\boldsymbol{u} + \boldsymbol{f} \tag{5.6}$$

$$\nabla \boldsymbol{u} = 0 \tag{5.7}$$

where ρ is the fluid density, P is total pressure, $\boldsymbol{u}$ is velocity vector (u,v,w) and μ is dynamic fluid viscosity. For three-dimensional problems, the equations form a set of four fully coupled partial differential equations (PDEs) governing the velocity components and the local pressure. NSE are the most accurate approach to simulate fluid flow in rough-walled fractures, but due to their high nonlinearity computationally expensive and difficult to handle. A more straightforward solution of NSE is to neglect the nonlinear inertial term leading to the Stokes equation. This simplification is just permissible for small Reynolds numbers ($Re \ll 1$), where the viscous term predominates the inertial term (Brush and Thomson, 2003). Vertical integration of the Stokes equation results in the local cubic law (LCL), which is a measure of the volumetric flow rate as a linear function of the pressure gradient with the cube of the overall aperture (Brown et al., 1995). The LCL is often applied to flow in the fracture scale.

5.2.3 *Numerical modeling*

The generated fractures can be used directly for finite element modeling (FEM) with the NSE by projecting them onto a three-dimensional mesh. For this purpose, a cuboid structured mesh consisting of $128 \times 128 \times 11$ hexahedra is created using the software Gmsh (Geuzaine and Remacle, 2017). The nodes of the mesh are subsequently deformed so that the previously created fracture surfaces represent the top and bottom face of the mesh and the nodes in between have a constant vertical spacing. The previously calculated apertures can serve as material-dependent input parameters for the vertical scaling within the simplified LCL calculations.

The numerical simulations are carried out with a finite element open-source application called TIGER (THMC sImulator for Geoscience Research) (Gholami Korzani et al., 2020). The code is based on the MOOSE (Multiphysics Object-Oriented Simulation Environment) framework (Permann et al., 2020) and designed for solving thermo-hydro-mechanical-solute transport problems in geothermal applications on different spatial and temporal scales. Nonlinear flow is realized via the Navier-Stokes module (Peterson et al., 2018). Each 3D realization is solved in parallel on an HPC system using Newton's method combined with the parallel direct solver SuperLU_dist at each linear iteration (Li and Demmel, 2003). Pressure-Stabilized Petrov Galerkin (PSPG) method is introduced to avoid instabilities arising from unstable element pairs and allow the usage of equal-order discretization in incompressible Navier-Stokes modeling (Hughes et al., 1986). The maximum mesh size is determined by a mesh sensitivity analysis to achieve highly accurate convergence with reasonable computational effort. By uniformly refining an initially $16 \times 16 \times 1$ element mesh, no improvement could be achieved at a vertical resolution of 8 elements (Figure 5.3). Dirichlet-type boundary conditions (BC) are applied in the direction of the overall pressure gradient (parallel and perpendicular to the shearing), with $p = 0.01, 0.1, 1, 5, 10, 20,$

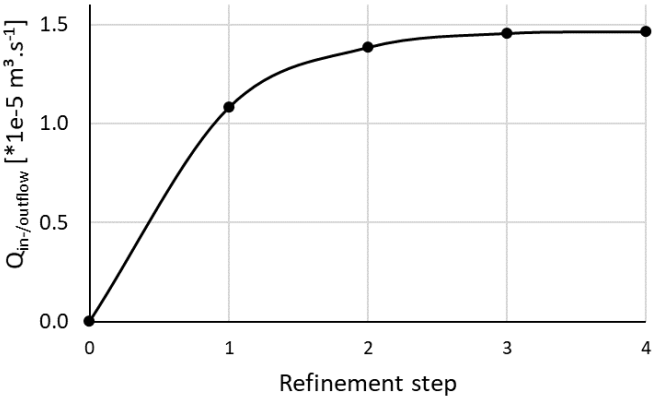

Figure 5.3: Results of the mesh sensitivity analysis by uniformly splitting a three-dimensional fracture mesh. Step 0 refers to a mesh with $16 \times 16 \times 1$ elements.

and 50 Pa at the inflow and $p = 0$ at the outflow boundary. The different BCs provide a transition of the flow regime from sub-laminar to fully turbulent. The remaining surfaces in the 3D modeling represent no-slip BC. Water is chosen as fluid with a viscosity $\mu = 0.001\,\mathrm{Pa\,s}$ and a density $\rho = 1000\,\mathrm{kg\,m^{-3}}$, respectively. A PSPG stabilization parameter ($a = 0.001$) is set to avoid pressure-induced oscillations.

5.3 CHANNELING

5.3.1 *Identification workflow*

Generally, channeling is defined as the spatial concentration of fluid flow, but there is no universal criterion or threshold on how quantify this process. Therefore, starting from the numerical flow simulation, an iterative multi-step workflow (Figure 5.4a) is developed to identify individual channels within a given flow-through medium based on different input variables. The individual steps of the workflow, from the fracture generation (Figure 5.4b) to the identified channels, are vividly illustrated using a base case, a 3D NS realization, and the volume flow as a critical variable (Figure 5.4).

In the first step, the critical variable (e.g., localized flow Q, Figure 5.4c) is identified, and the first guess for a threshold, here a local flow rate threshold Q_t, is made. For all nodes N, nodes i with $Q_i > Q_t$ are marked as channel nodes and it is checked if the main criterion (e.g. 35 % of the entire mesh flow rate located in the marked nodes, see Figure 5.4d) is fulfilled. If this is not the case, the threshold value is continuously reduced, and the workflow is iterated again over the entire mesh. If true, the skeletonized channel network is extracted, and the connectivity between the identified channels is further evaluated. This is done by setting up a 3×5 sampling window, which assigns nodes with two or more connections to the same unique channel (Figure 5.4e). Since a channel is defined as a coherent and continuous structure, the next step is to remove background noise in the form of channels that are poorly connected (less than 10 % of the

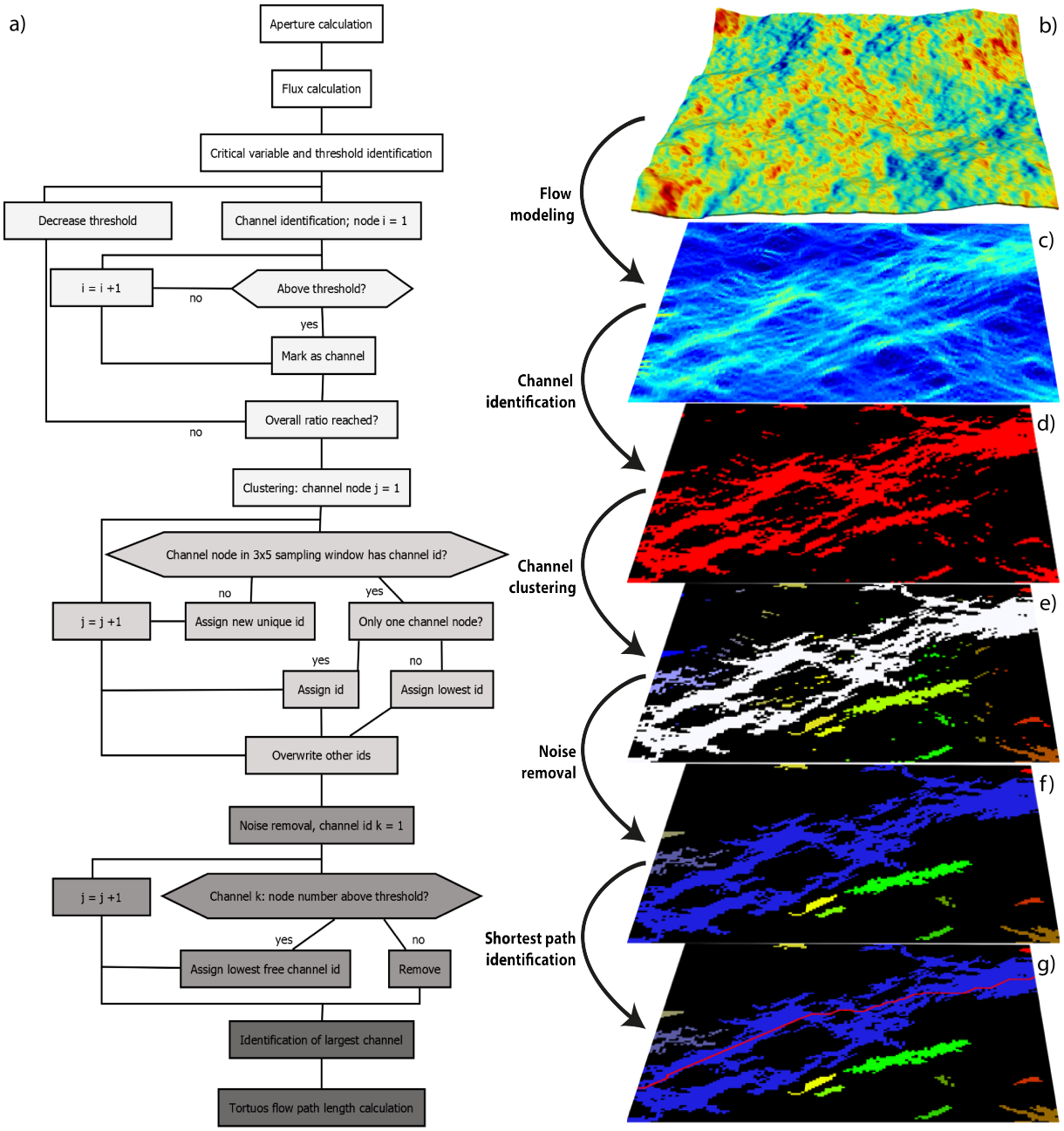

Figure 5.4: a) Workflow from aperture calculation to the channel identification; b-g) The different steps of the multi-stage filter concept for channel identification and the resulting figures for $R_{chan} = 0.35$. b) 3D morphology of the fracture and the local aperture. v) The calculated flow rates of the 3D Navier-Stokes solution. d) Identified and skeletonized channel nodes. e) Assigned channels with their ID. f) Channels after background noise removal. g) The red line indicates the 3D shortest connection from left to right.

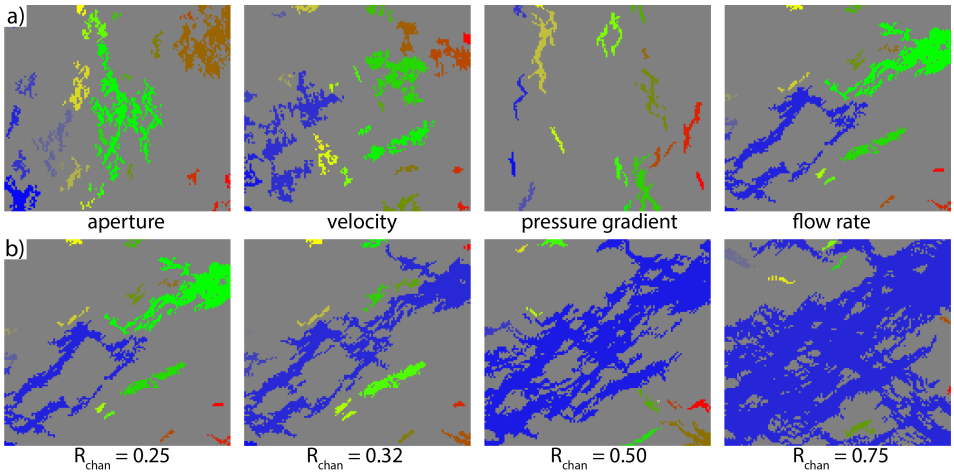

Figure 5.5: a) Tested critical variables for channel criterion with a ratio of 25 %. b) Different channeled flow ratios R_{chan}. All variables are tested with the same realization for flow and shearing oriented parallel and a pressure gradient of 50 Pa m^{-1}.

fracture length l_{frac}, Figure 5.4f). In the final step, the longest ongoing channel is identified and the length of the fully-tortuous flow path is evaluated using Dijkstra (1959) shortest path algorithm. This path length considers all geometrical effects, including both the local roughness and the geometric tortuosity caused by the undulating surface (Figure 5.4g). An evaluation of the streamlines was rejected because it is based on velocity data but does not consider information about the volumetric flow rates.

Once an identification workflow is established, a critical variable must be identified to detect and quantify channeling processes in terms of flow geometry and regime. While this criterion should be rather simple and general, it must allow the identification of the flow backbone. Although it is common to use the variable of main interest, the volumetric flow rate (or the recalculated effective permeability), as a critical variable (Le Goc et al., 2010), several other variables (aperture, velocity, flux, pressure gradient, participation ratio) have been tested for their applicability to different flow constraints. Figure 5.5a shows the identified channels exemplified for a single realization with a boundary pressure gradient of 50 Pa m^{-1}, a threshold ratio of 25 %, and different tested variables.

The volumetric flow rate, as a combination of flux and aperture, gives the most promising results and is therefore retained. While a minimum flux threshold Q_t for fracture networks is quite obvious (is flow along a fracture?) (Maillot et al., 2016), an absolute value for Q_t in combination with single fractures or porous media is not useful. However, universal applicability in all types of flow-through media and the ability to compare between different realizations can only be achieved by keeping the ratio of flow localized in the channels (R_{chan}) constant:

$$R_{chan} = \frac{Q_{chan}}{Q_{tot}} \tag{5.8}$$

with:

$$Q_{tot} = \sum_{i=1}^{N} Q_i \tag{5.9}$$

$$Q_{chan} = \sum_{i=1}^{N} Q_i \{Q_i \geq Q_t\} \tag{5.10}$$

where Q_i is the integrated local flow volume, Q_{chan} the amount of flow localized in channels, Q_{tot} the entire domain flow.

5.3.2 *Geometric threshold identification*

Once the critical variable has been determined, an appropriate threshold must be identified. As introduced in the previous chapter, there is no common R_{chan}^{crit} for the identification of channeling. An approach describes the use of a specific percentile of the nodal flow rate as a critical limit for channel identification (Knudby and Carrera, 2005; Marchand et al., 2020). Although simple, the criterion depends on the arbitrary choice of the threshold. Rather than a deterministic threshold, we seek a statistical characteristic that captures the extent of channeling and can also be used simultaneously to compare the channel properties with the onset of nonlinear flow conditions. Inspired by the rather statistical indicators of Le Goc et al. (2010) and the application-related indicators of Marchand et al. (2020), we discuss two geometric characteristics of channels in more detail and afterwards define an R_{chan}^{crit}. How do the interconnected transport volume and heat exchange area of the channels change with increasing R_{chan}?

Addressing this question, both properties must be defined first. The effective transport volume $V1$ of the identified channels as a function of the channeled flow R_{chan} is determined by Equation 5.11

$$V1(R_{chan}) = \frac{1}{V_{tot}} \sum_{i=1}^{N} V_i \{Q_i \geq Q_t\} \tag{5.11}$$

where $V1$ is the normalized channel volume, V_{tot} is the entire fracture volume, V_i is the element volume. The heat exchange area or more general, the flow-wetted surface $A1$, of the identified channels as a function of the channeled flow R_{chan} is determined by Equation 5.12 and considers, that a fracture is confined by two opposing surfaces:

$$A1(R_{chan}) = \frac{1}{2A_{tot}} \sum_{i=1}^{N} (A_i^{top} + A_i^{bot}) \{Q_i \geq Q_t\} \tag{5.12}$$

where $A1$ is the normalized channel half area. A_{tot}, A_i^{top} and A_i^{bot} are the entire 3D fracture surface area, the element top, and bottom area, respectively.

In the case of homogeneous flow through the entire fracture (e.g., the parallel plate approach), a linear relationship exists between the flow ratio R_{chan} and the channeled volume/area with $V1 = V_{pp}$ and $A1 = A_{pp}$. $V1$ and $A1$ are biased towards smaller values when the flow rate contrast within the fracture increases. With increasing channeling also, the distance between the identified flow paths increases. The inverse ($V1^{-1}$) is a measure of the average distance between highly conductive areas. Hence, it is not the absolute values of $V1$ and $A1$ that are of interest, but the distance to the parallel plate model, as the non-channeled extreme case calculated as $V_{pp} - V1$ and $A_{pp} - A1$. Figure 5.6a shows $V_{pp} - V1$ as a function of R_{chan} for all realizations with a constant pressure gradient of $50\,\mathrm{Pa\,m^{-1}}$ and the two extreme cases of the orientation of flow and shearing oriented parallel (red) and perpendicular (blue).

All realizations, regardless of the flow direction, show a strongly localized flow, where the effective flow-through volume represents only a small part of the total fractures' void space. Nevertheless, differences between the two extreme cases of flow directions exist. In a perpendicular orientation of flow and shearing, large portions of the fluid are localized in a few channels and the results show dependence on the original geometry in the form of a large dispersion. This extreme case of highly localized flow and minimal volume is therefore defined as channel sweeping. A parallel orientation of flow and shearing leads to a significantly lower degree of channeling, and large portions of the fluid are distributed over large fracture volumes. Moreover, the results are homogeneously distributed and show no dependence on the initial fracture geometry. Surface sweeping is thus the dominant process.

Similarly, Figure 5.6b shows $A_{pp} - A1$ as a function of R_{chan} for all realizations with a constant pressure gradient of $50\,\mathrm{Pa\,m^{-1}}$ and the two extreme cases of the orientation of flow and shearing oriented parallel (red) and perpendicular (blue). Localized flow preferentially follows regular geometries of least resistance, thus tortuous domains of the entire fracture with large surface area tend to be in the surface sweeping domain, and contrasts between flow directions are less pronounced than for $V1$. Consequently, as the level of channeling increases, $A1$ is strongly negatively biased.

Now we come back to the question of a suitable threshold value for R_{chan}^{crit}. As R_{chan} is not uniform but varying between 0 and 1 (see Figure 5.6), we look for a statistical critical R_{chan}^{crit} above which channeling is fully captured within our analysis. Starting with a strong increase, a value $R_{chan} = R_{chan}^{crit}$ can be identified from which $V1$ and V_{pp} run parallel and the difference is not further increased. The gradient of $(V_{pp} - V1)$ tends towards zero:

$$\Delta(V1 - V_{pp}) = 0 \tag{5.13}$$

For a parallel orientation of shearing and flow a critical flow ratio $R_{chan}^{crit} = 0.32$ can be identified. This value is therefore applied equally to all realizations for the following investigation of the nonlinear channeling characteristics.

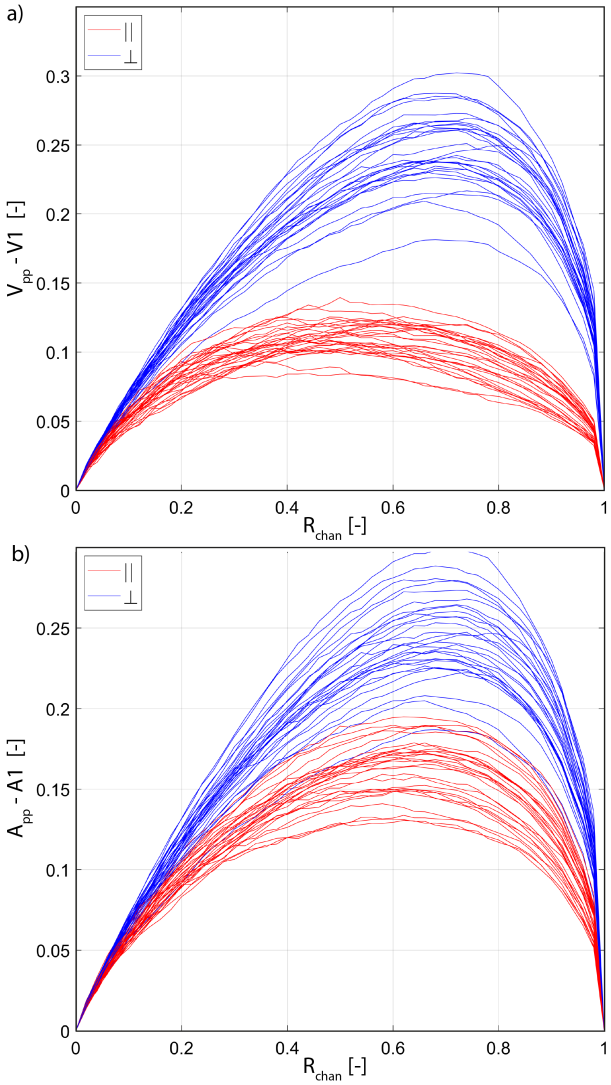

Figure 5.6: a) Difference between the localized channel volume $V1$ and the volume of the non-channeled parallel plate approach V_{pp} as function of the amount of localized flow ratio R_{chan}. b) Difference between the localized channel half-area $A1$ and the area of the non-channeled parallel plate approach A_{pp} as function of the amount of localized flow ratio R_{chan}.

5.3.3 *Channel indicators*

The two previously introduced indicators $V1$ and $A1$ describe the channeling process as a whole, but no statement can be made about the distribution of the channels within the fracture domain and the connectivity and continuity of the individual channels with respect to the flow regime The interconnection and connectivity of the channel network are further evaluated by identifying the main flow path within each realization (Figure 5.4g). Using the shortest path theory, the two flow-based indicators $C1$ and $C2$ are developed to describe the flow path in the three-dimensional space. The combined interconnection and

continuity indicator $C1$ is the normalized channel length with respect to the fracture length:

$$C1(R_{chan}) = \frac{dist(p_{start}, p_{end})}{l_{frac}} \{Q_i \geq Q_t\} \tag{5.14}$$

where $C1$ is the normalized distance dist between the start point p_{start} and endpoint p_{end} of the main channel and l_{frac} is the fracture length in the direction of the global pressure gradient. $C1 \geq 1$ indicate channels that can be traced in the direction of the pressure gradient throughout the fracture. A maximum value of $C1 = \sqrt{2}$ is reached when the main flow path is diagonally connected through the fracture.

The continuity indicator $C2$ is not a measure of the absolute channel length within the fracture but describes the real and three-dimensional continuity of the main flow path within each realization. Therefore, channel tortuosity $C2$ is determined as the shortest connection within the extreme points of the main channel (red line in Figure 5.4g) and calculated:

$$C2(R_{chan}) = \frac{path(p_{start}, p_{end})}{dist(p_{start}, p_{end})} \{Q_i \geq Q_t\} \tag{5.15}$$

where $C2$ is the normalized and $path(p_{start}, p_{end})$ the absolute length of the 3D tortuous flow path along the local median plane $m(x, y)$ and in the direction of the overall pressure gradient. Indicator $C2$ can take only values greater than 1, where $C2 = 1$ means that the channel suffered no topological height changes. A high $C2$ is a measure of the reduced pressure gradient within the fracture.

5.4 NONLINEAR CHANNEL CHARACTERISTICS

5.4.1 *Pressure-dependence*

The channeling characteristics of all realizations are evaluated based on critical flow ratio $R^{crit}_{chan} = 0.32$. The use of seven pressure gradients between $0.05\,\mathrm{Pa\,m^{-1}}$ and $250\,\mathrm{Pa\,m^{-1}}$ ensures mean $Re \ll 1$ up to $Re = 220$ (Egert et al., 2021b), which allows the quantification of nonlinear effects on channeling processes in the transition from linear to nonlinear flow regimes. In the first step, the changes in the geometrical indicators $V1$ and $A1$ are presented. Then, two indicators describing the channel continuity and interconnection ($C1$ and $C2$) are further investigated. Figure 5.7a depicts indicator $V1$ as a function of the global pressure gradient and with respect to the flow direction. Mean and standard deviation are report in Table 5.1.

A perpendicular orientation of flow and shearing results in channel sweeping. Depending on the initial fracture geometry, $V1$ is between 12 and 18 %. Increasing nonlinear effects do not lead to a change of the mean value, only to an increase of the overall variance. In contrast, surface sweeping dominates with a parallel orientation of flow and shearing. The results exhibit an initial volume between 20 and 23 %, which is rather independent of the chosen fracture geometry. Upon

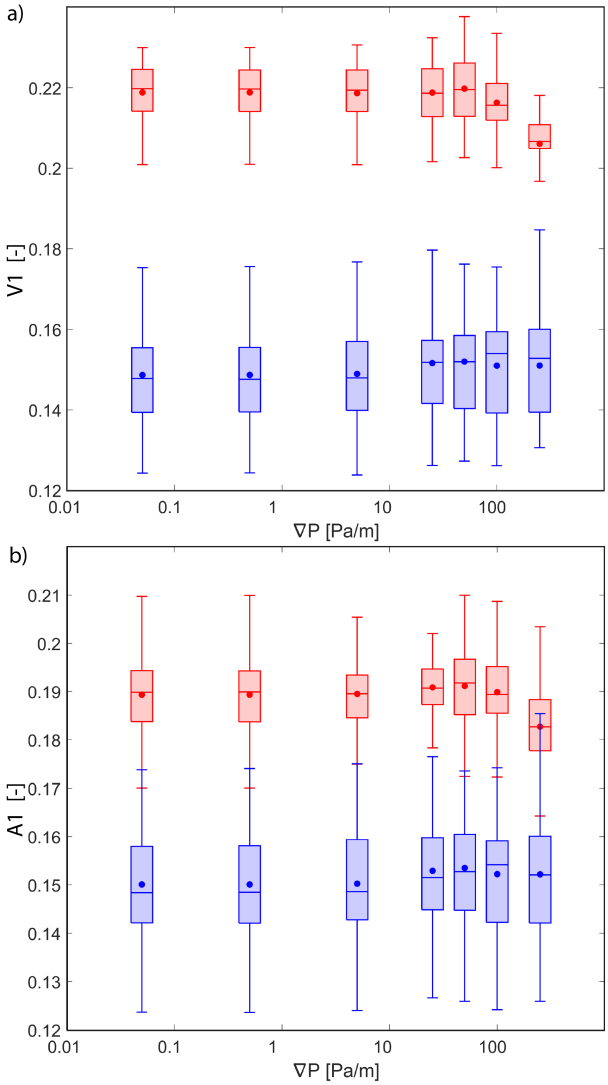

Figure 5.7: Normalized a) channel volume ($V1$) and b) channel area ($A1$) for flow parallel (red) and perpendicular (blue) to the direction of shearing as a function of the pressure gradient.

increasing pressure gradient, nonlinear effects cause increased localization of flow within channels. A lower channel volume ($-1\,\%$ for a pressure gradient of $250\,\mathrm{Pa\,m^{-1}}$) is required to localize a certain given volumetric flow rate. Siena et al. (2019) showed comparable trends with shrinking channel size in porous media and increasing Re in the transitional regime ($Re = 1 - 10$). Egert et al. (2021b) were able to demonstrate that nonlinear effects are pronounced outside flow channels, while in the channels an ideal flow field and a higher LCL validity are more likely to be preserved even at high flow rates. Indicator $A1$ has similar trends as $V1$ (Figure 5.7b). A perpendicular orientation of flow and shearing results in a flow-wetted surface between 12 and 18 %, which is only slightly affected by increasing flow rates. The mean area remains constant, but the variance of the results increases. Once flow and shearing are oriented parallel, $A1$ between 17 and 21 % is observed. Nonlinear effects cause a reduction of $A1$

from 19 to 18 % and the more pronounced channeling leads to less dispersion of the results.

The continuity of the channels is analyzed with the aid of $C1$ and $C2$. Figure 5.8a depicts the resulting continuity indicator $C1$ with respect to the global pressure gradient and for flow and shearing oriented perpendicular (blue) or parallel (red). The averages and standard deviations of the statistical indicator $C1$ are shown in Table 5.1. A perpendicular orientation of flow and shearing results in well-formed and straight channels that exhibit continuity throughout the fracture with $C1 \cong 1$ regardless of the initial sheared geometry. This may imply that the channels are close to percolation and straight through the fracture or that the channels are oriented diagonal and shortened. The transition to nonlinear flow regimes results in slightly increased channeling and an associated increase in mean continuity. In the case of parallel orientation of flow and shearing, $C1$ exhibits a strong dependence on the fracture geometry, being a function of the occurrence of interconnected permeable structures. $C1$ ranges between 50 and 120 %, indicating that both, poorly connected and short channels ($C1 < 1$), and connected but diagonal channels ($C1 > 1$) exist. As the pressure gradient increases, $C1$ tends towards 1, thus short channels show improved continuity, whereas already existing long channels form a straighter path due to an improved interconnection. A similar directional dependence of the continuity was also shown by Marchand et al. (2020), although a two-dimensional analysis using effective apertures leads to more homogeneous results.

Figure 5.8b depicts the continuity indicator $C2$ as a function of the global pressure gradient and with respect to the direction of flow. The averages and standard deviations of the statistical indicator $C2$ are summed in Table 5.1. A perpendicular orientation of flow and shearing results in a uniform tortuosity between 105 and 110 %. An increase in the pressure gradient leads only to a slight decrease in tortuosity within the already straight channels. A different situation occurs with a parallel orientation of flow and shearing. An initial high tortuosity of more than 115 % indicates a strongly prolonged path length within the fracture void geometry. This path length is caused by the poor interconnection of large void spaces and higher local pressure gradients, which means that the path of least resistance is often not direct. As the pressure gradient increases, the channels become more independent of the local fracture geometry, allowing enhanced channeling effects to provide more direct connections, and decreasing $C2$.

The determined indicators can be compared not only against the pressure gradient but also with each other. A comparison of the geometric indicators $V1$ and $A1$ reveal the two dominant regimes of channel and surface sweeping, respectively, in the form of two separated clusters (Figure 5.9a). Channel sweeping (blue) has an identical $A1V1^{-1}$ ratio whose absolute value depends solely on fracture geometry. In the case of dominant surface sweeping (red), the $A1V1^{-1}$ ratio is shifted toward the volume and has significant dispersion. As the flow rates increase, the $A1V1^{-1}$ ratio changes towards unity, both clusters tend to converge, and the influence of channel sweeping increases. The combination of both indicators is thus a measure of the proportion between the dominant

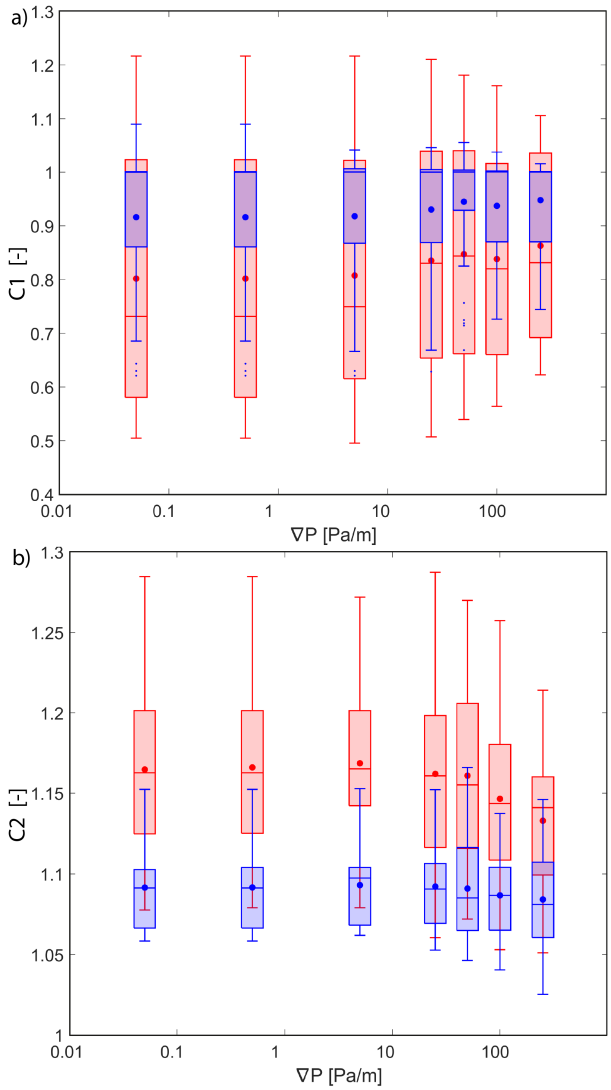

Figure 5.8: Normalized a) channel length ($C1$) and b) channel tortuosity ($C2$) for flow parallel (left) and perpendicular (right) to the direction of shearing as a function of the pressure gradient.

	$\parallel$				$\perp$			
∇P	0.05 Pa m^{-1}		250 Pa m^{-1}		0.05 Pa m^{-1}		250 Pa m^{-1}	
	$\overline{x}$	$\overline{\sigma}$	$\overline{x}$	$\overline{\sigma}$	$\overline{x}$	$\overline{\sigma}$	$\overline{x}$	$\overline{\sigma}$
$V1$	0.22	0.01	0.2	0.01	0.15	0.01	0.15	0.01
$A1$	0.19	0.01	0.18	0.01	0.15	0.01	0.15	0.01
$A1V1^{-1}$	0.86	0.03	0.89	0.04	1	0.01	1	0.02
$C1$	0.8	0.23	0.86	0.17	0.92	0.14	0.95	0.09
$C2$	1.16	0.06	1.13	0.04	1.09	0.03	1.08	0.03

Table 5.1: Mean and standard deviation for the identified indicators with respect to the flow direction, pressure gradient, and critical channeling threshold.

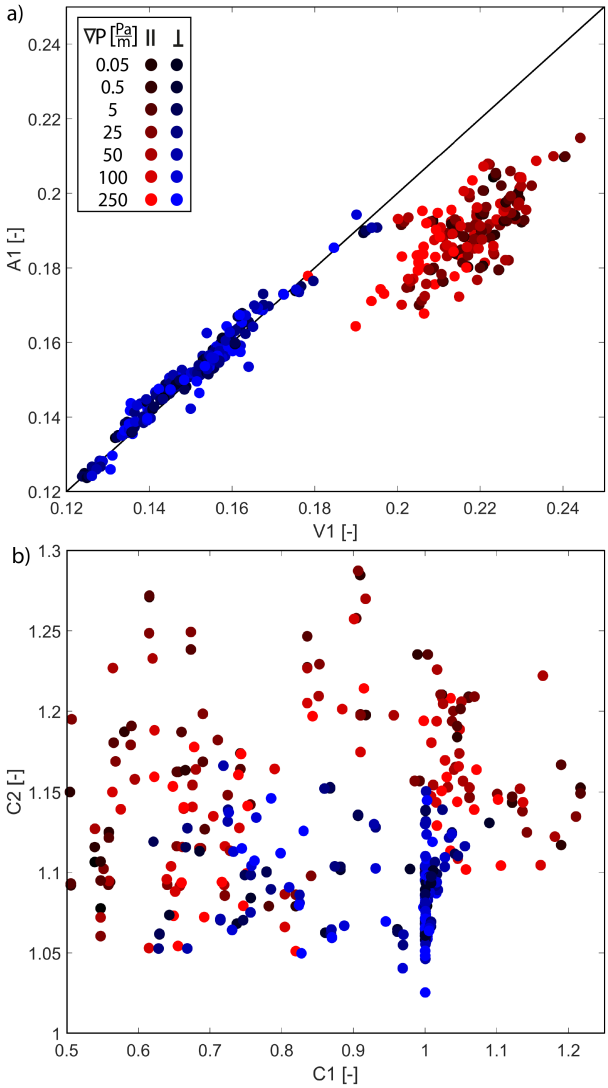

Figure 5.9: a) $V1$ vs. $A1$ for all realizations. Channel sweeping tends to show a linear increase of $A1$ with $V1$ whereas surface sweeping results in dispersed results. b) $C1$ vs. $C2$ for all realizations. Channel sweeping tends to have a uniform continuity, while surface sweeping results in highly scattered data. The red data tends to higher $C1$ and less $C2$ for increasing pressure gradient.

flow processes within the fracture and the transition from channel to surface sweeping.

The link between the two continuity indicators $C1$ and $C2$ is depicted in Figure 5.9b. In the case of parallel orientation of flow and shearing (red), surface sweeping dominates, and no dependence between $C1$ and $C2$ can be identified. In case of a perpendicular orientation of flow and shearing, $C1$ dominates but no quantitative statement about the connection of the indicators $C1$ and $C2$ can be made. As pressure gradients increase, the ratio of both flow directions and regimes tends toward unity, representing well-formed and continuous channels without any topographic height changes.

5.4.2 *Implications on large-scale reservoirs*

The formation of preferential flow paths is not only important on a laboratory scale but must be discussed with respect to fractured (geothermal) reservoirs. Given an open fractured system formed from the displacement of opposing fracture surfaces the character of flow could vary between the two extreme cases, a rather focused channel sweeping or a rather dispersed surface sweeping, resulting from the orientation of flow and shearing: channel sweeping with highly localized flow rates evolves typically from flow perpendicular to the shearing whereas surface sweeping from flow parallel to the shearing.

Therefore, the extend of channeling in a fracture will also be affected by the geomechanical process during its creation. In reservoir conditions, typical normal stress setting with vertical shear fractures close to $\sigma_1 - \sigma_2$ and vertical displacement, a horizontal flow between two wells tend to form channel sweeping and improved hydraulic conductivity (Lang et al., 2018). Having a strike-slip component with horizontal displacement along σ_1, a surface sweeping with less expectable flow rates and increased nonlinear effects could result. In the geometrical complexity of a fracture system in a reservoir, the co-existence of improved, and impeded flow regimes would result in a strong dependence upon the orientation of the most conductive features and could explain contradicting observations regarding the nonlinear behavior of geothermal systems (Kohl et al., 1997). A dominating flow regime could even change under mechanical stimulations employed to enhance existing fractures (Evans, 2005).

The formation of channels affects the transport and exchange of heat with the surrounding (impermeable) host rock, which can have contradictory effects on the performance of a reservoir (Chen and Zhao, 2020). Severe channeling leads to a decrease in $V1$ and $A1$ compared to the standard parallel plate model, resulting in a significantly reduced effective heat exchange area between the flowing fluid and the matrix as well as a reduced heat transfer coefficient. A large proportion of stagnant-water zones, which are primarily present in low-aperture regions, asperities and outside the identified channels, allow only a small amount of heat exchange. In contrast, channeled flow can also increase reservoir performance by extending the tortuous path length $C2$ of the flowing fluid within the fracture geometry (Guo et al., 2016). As a result, both the heat exchange area and the exchange time increase, as a reduced pressure gradient also leads to lower flow velocities. Applied to the two extreme cases of channel and surface sweeping, this implies that a perpendicular orientation of flow and shearing tends to be detrimental to reservoir performance by forming percolated and highly localized channels with low surface area and tortuosity. In contrast, a parallel orientation of flow and shearing tends to form less channeling and a prolonged flow distance, which can be advantageous for the heat exchange. In this extreme case, an increase in flow rates and rising nonlinear effects outside the identified channels lead to a decrease in both, the tortuous flow distance as well as the heat exchanger area.

Channeling effects are also identified via solute breakthrough curves, as matrix diffusion can be neglected for conservative tracers (Egert et al., 2020), making the shape of the curve a direct representation of the subsurface flow regime

(Klepikova et al., 2016). In this context, the relationship between channel and surface sweeping is of interest, because the highly localized flow paths in channel sweeping lead to the formation of a dominant peak, while surface sweeping causes strong mixing and long tailing (Moreno et al., 1988). Sorptive tracers are affected by a reduced flow-wetted surface.

5.5 CONCLUSION

The proper representation of small-scale fluid flow within the complex three-dimensional fracture geometry has proven to be of critical importance in a sustainable and safe reservoir performance prediction and hydrogeological numerical modeling. Unfortunately, few models characterize the flow field and formation of preferential flow paths within fractures without prior simplifications regarding geometry and flow law. As a remedy, we developed a workflow to identify channels and defined four indicators that can geometrically and statistically quantify the extent of channeling processes. The indicators are analyzed concerning their ability to characterize transport-relevant properties and changes in the flow regime as well as direction and to make predictions about large-scale flows in the fractured reservoir. The two geometric indicators $V1$ and $A1$ capture the flow-through volume and heat exchanger area, respectively. The two connectivity indicators $C1$ and $C2$ describe the continuity of the main flow path relative to the fracture length and with respect to the tortuous flow path.

With the four indicators, two characteristic flow regimes could be identified within the fracture: A focused channel sweeping and a dispersed surface sweeping. The first occurs with a perpendicular orientation of flow and shearing. Long, well-connected, and low-tortuous fluid pathways lead to severe and stable localization of volumetric flow, so that only small parts of the fracture void space and surface participate in effective flow, while large areas represent quasi-stagnant water zones. The latter is a consequence of the parallel orientation of flow and shearing. Volumetric flow is less localized than in the channel sweeping so that large areas of the fracture are still effectively flowed through. The identified channels are tortuous, increasing the flow path length and heat exchanger area, and reducing the pressure gradient. As the global flow rate increases, rising nonlinear effects, mainly outside the identified channels, cause increased localization of the volume flow and thus a transition into channel sweeping. The numerical workflow we developed to characterize the small-scale flow regime thus contributes to the predictability of the performance of a fractured reservoir. Subsequent research should focus on the experimental confirmation of the numerical results. Furthermore, additional shear displacements and higher flow velocities should be considered, also with respect to changes in the heat and mass transfer.

6

TRIAXIAL TESTING AND HYDRAULIC-MECHANICAL MODELING OF SANDSTONE RESERVOIR ROCK IN THE UPPER RHINE GRABEN

This chapter is published in Geothermal Energy 6, 23, doi:10.1186/s40517-018-0109-0.

ABSTRACT

The Upper Rhine Graben (URG) is a highly favorable location for deep geothermal energy utilization. One of the main reservoir horizons is the lower Triassic Buntsandstein formation. While quantification of thermal and hydraulic parameters and their coupling is common, geomechanical factors are often neglected due to high costs and the expense in gathering data. Equivalent experiments with analogue rocks, like triaxial tests, can help to improve this knowledge. Triaxial tests have been performed and evaluated on two different Buntsandstein rock examples as analogues to quantify the mechanical behavior under stress conditions found in the Buntsandstein of the URG. Both samples, Tennenbach (TenSst) and Pfinztal (PfSst) Sandstone, show high Young's moduli under axial loading. With confining pressures up to 90 MPa, the axial failure strength is up to 448 (TenSst) and 561 (PfSst) MPa. The results demonstrate the usability of linear elasticity for the expected stress range in the Buntsandstein reservoir of the URG. The deformation behavior is described and a linear failure criterion is derived, predicting failure strength with a high accuracy. These experimental results can be further employed as calibration parameters for a hydro-mechanical evaluation of the deformation processes.

6.1 INTRODUCTION

The determination of the subsurface conditions and reservoir properties is indispensable for exploration and exploitation of a geothermal field. It includes the expected geological structures as well as the hydraulic, thermal, chemical and mechanical parameters of the target horizon which should be favorable for geothermal utilization. Most essential is a high permeability to supply sufficient flow rates and high temperatures (Stober and Bucher, 2012). An area in Germany which fulfills the criteria is the Upper Rhine Graben with a unique geothermal potential (Agemar et al., 2014). Local temperature anomalies with elevated temperatures up to 165 °C are expected at a depth of 2500 m, while

the average geothermal gradient of the URG is above $40\,\mathrm{K\,km^{-1}}$ (Agemar et al., 2013). Especially the sedimentary formation of the Triassic, Buntsandstein and Muschelkalk, shows high permeabilities, which are necessary to provide high flow rates (Stober and Bucher, 2015).

However, the estimation of the geothermal potential of a reservoir from averaged data leads to high engineering risks. Mostly, pointwise distributed data are collected from few exploration wells and interpolated in the surrounding area, while horizontal and vertical heterogeneities are unknown (Fitch et al., 2015). Interpretation of geophysical data, like 2D or 3D seismic measurements, can provide spatial information, but is limited to larger structures, like faults or horizons, while fractures and small-scale heterogeneities are unresolvable (Mansfield and Cartwright, 1996). Preliminary studies on analogue rocks can help to decrease this risk by filling the gap between point data and reservoir scale (Philipp et al., 2008). Triaxial tests offers the opportunity to estimate the rock strength of a potential rock masses to reduce risks for wellbore and reservoir stability (Lama and Vutukuri, 1978).

While these analogue tests offer unique data averaged for the whole sample, sophisticated numerical methods are required for reservoir scale evaluations. Simulations are used to analyze mechanical and hydraulic processes and their linkage between each other in detail and to quantify their influence on both the results and vice versa (Rutqvist et al., 2002). The recent progress in hardware and software development allows calculating the complex coupling of physical processes in a natural and perturbed geoscientific environment at efficient computation times (Kohl et al., 1995; O'Sullivan et al., 2001; Watanabe et al., 2017). The experimental results of different tests, like triaxial or permeability tests, carried out with a permeameter can also be used as input and calibration parameters to upscale the laboratory to reservoir data (Settari et al., 2013).

6.2 GEOLOGICAL OVERVIEW

6.2.1 *Upper Rhine Graben*

The Upper Rhine Graben (URG), as a main geothermal target, is a NNE-SSW to N-S-striking graben structure in the central part of the 1100 km extended European Cenozoic rift system (Illies, 1965; Pflug, 1982). The evolution of the URG is related to polyphase reactivations of lithospheric crustal discontinuities since the late Paleozoic (Ziegler and Dèzes, 2005). The main phase of tectonic rifting starts in the middle Eocene with an NW-SE extension of the upper crust and the reactivation of the Permo-Carboniferous and variscan discontinuities, which lead to SW-NE striking stress regime (Ziegler et al., 2004). In the Miocene the regional stress field changes to a NW-SE sinistral transtensional regime with reactivation of the older fault system (Illies, 1972). Starting from the northern part, the URG was subjected to large subsidence and sedimentation up to 3.5 km (Grimmer et al., 2017). There are two reservoir lithologies for the utilization of geothermal energy in the URG. The crystalline basement, e.g. granite, can be utilized as an enhanced geothermal reservoir, like in Soultz-sous-Forêts (Held

et al., 2014), and the higher porous and conductive sedimentary formations, like Buntsandstein or Muschelkalk, as hydrothermal reservoir, like Bruchsal (Meixner et al., 2014). High flow rates, especially in fracture or fault systems, are expected in the URG to achieve geothermal usage.

The recent stress field in the URG is characterized by a NW-SE orientation with local variations. The northern part of the URG with an orientation from $N130°E$ to $N135°E$ is characterized by normal faulting, while in the southern part, striking $N145°E - N160°E$, a transition from strike-slip to normal faulting is observed (Cuenot et al., 2006; Meixner et al., 2014; Plenefisch and Bonjer, 1997). The stress ratio is close to 1.0 for S_{Hmax}/S_v and 0.55 for S_{hmin}/S_v (Cornet et al., 2007; Valley and Evans, 2007).

The Buntsandstein formation is, due to its high permeability, one of the preferred horizons for targeting hydrothermal reservoirs in the URG (Stober and Bucher, 2015). Due to its polyphase tectonical history, the Buntsandstein is separated into different blocks with varying subsidence and exhumation (Ziegler et al., 2004). The depth of the Buntsandstein is 3000 m below surface in the central part of the URG with a thickness up to 500 m (Jodocy and Stober, 2010). The temperature of the Buntsandstein reservoir is 160 °C with an elevated geothermal gradient of $\approx 45\,\mathrm{K\,km^{-1}}$ (Stober and Bucher, 2015). Stresses between 35 and 75 MPa have been observed for the geothermal site of Soultz-sous-Forêts and are expected in the Buntsandstein reservoir (Cornet et al., 2007; Valley and Evans, 2007). Analogues of the Buntsandstein are found in nearby outcrops, e.g. in the Vosges Mountains, the Kraichgau and the Black Forest (Bauer et al., 2017, 2015; Eisbacher and Fielitz, 2010).

6.2.2 *Mechanical characterization*

Uniaxial and triaxial tests are common lab testing methods to assess the reservoir behavior under varying stress conditions (Fjar et al., 2008). These tests can provide information about static mechanical parameters (e.g. Poisson's ratio, Young's modulus, yield and failure stress) for a single sample under defined experimental conditions (Jaeger et al., 2007). The tests help to predict the volumetric changes due to compaction (Zoback, 2011). Data characterizing the mechanical properties of different kind of high porous sandstones are collected by the oil industry and can be found in Chang et al. (2006), Cuss et al. (2003), and Wong et al. (1997). Bauer et al. (2017) shows the UCS, Young's modulus and porosities of Buntsandstein analogues from the eastern URG. Triaxial experiments on Triassic Sandstone of the Vosges (VsSst) have been reported by (Bésuelle, 2001).

It was shown that rocks in the upper crust are not very sensitive to temperature- and strain rate-changes (Donath and Fruth, 1971; Serdengecti and Boozer, 1961). The main objectives are the prediction of failure under varying confining pressures, using different approaches and concepts. Different concepts can be used: 1) a linear correlation between the horizontal and vertical stresses, like Mohr-Coulomb and Drucker-Prager (Drucker and Prager, 1952), or 2) specific failure envelope to describe mathematically and empirically the behavior of different rock types. The latter approach is divided into two categories: brittle and com-

pactive, depending on the failure or localization behavior. The volume of the sample increases in brittle failure, while it decreases for compaction (Rutter and Glover, 2012). The gradual transition, between these two end members of failure types, is the subject of intensive scientific investigations aiming to understand the compaction behavior and the effects on mechanical parameters (e.g. Rudnicki, 2004; Rutter and Glover, 2012; Wong and Baud, 2012; Wong et al., 1997). So, for practical purposes, usually an elliptical shaped failure surface is assumed (e.g. Baud et al., 2000; Rutter and Glover, 2012). Instead, for brittle failure often a parabolic failure envelope is observed (e.g. Cuss et al., 2003; Khan et al., 1991). Rutter and Glover (2012) connects the transition to the critical state concept, where in differential vs. mean stress space, a linear relation with a slope of 1.18 ± 0.03 represents the transition, where no volume change at failure occurs.

The impact of the geomechanical behavior on hydraulic-related parameters, like porosity and permeability of the reservoir, is commonly known as poroelasticity (Biot, 1956; Terzaghi, 1943). The significance of mechanical and thermal variations to hydraulic parameters effecting the productivity of a reservoir is huge (Bernabé et al., 2003; Geertsma, 1957; Zimmerman, 2000), while their quantification with measurements is limited (Han and Dusseault, 2003). The relationship between the two parameters porosity and permeability is in most cases described by a Kozeny-Carman-like relationship (Carman, 1956).

6.3 MATERIAL AND METHODS

6.3.1 *Rock material*

Two types of sandstone with different mineralogical composition have been used in the triaxial experiments: Pfinztal Sandstone (PfSst) and Tennenbach Sandstone (TenSst). Both rock types are analogues for the lower Triassic Buntsandstein formation in the Upper Rhine Graben (URG) and have been collected in quarries close to the URG. An extensive study on the petrological parameters is done by Schmidt et al. (2017).

Pfinztal Sandstone

The Pfinztal Sandstone (PfSst) is a red-colored, compact and well-sorted sandstone with a grain size between 0.04 mm and 0.2 mm, typically >0.1 mm (Figure 6.1a and 6.1b). The framework is based on angular and sub-spherical clasts and elongated muscovite plates which lead to a layered texture (Figure 6.1a). The matrix is grain-supported. The modal composition is 49 % quartz, 16 % K-feldspar, 11 % muscovite, 15 % cementation including hematite and 1 % accessory phases (Table 6.1). The samples show slight alteration. The porosity is 8 %, the permeability is 3.0×10^{-17} m^3 (measured for 4 samples in permeameters) and the density 2.38 g cm^{-3} (Schmidt et al., 2016).

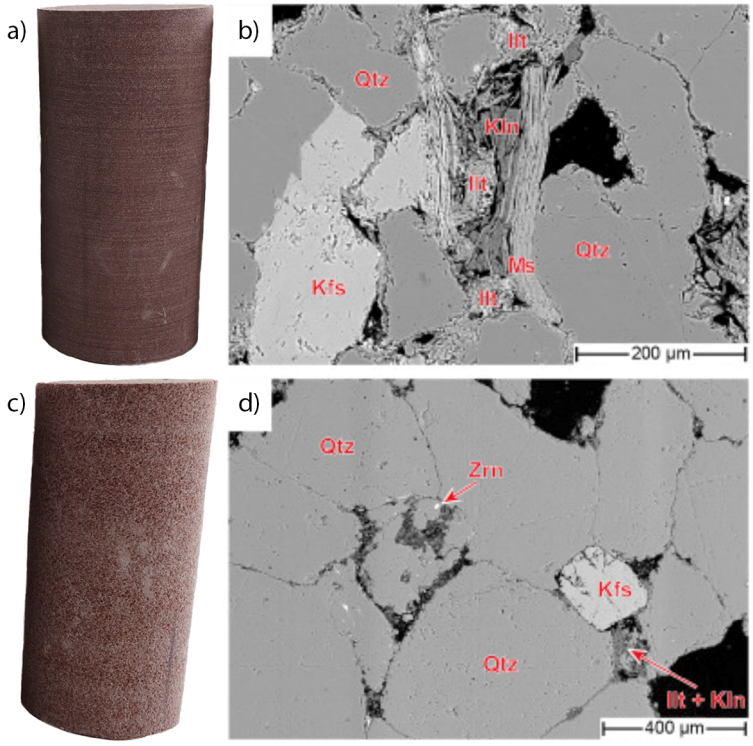

Figure 6.1: Samples for the triaxial tests for a) layered PfSst and c) unlayered TenSst. Thin section images of b) PfSst and d) TenSst in BSE mode with their mineral composition and pore space (black) (modified after Schmidt et al., 2017).

Tennenbach Sandstone

The Tennenbach Sandstone (TenSst) is a red-colored, coarse-grained and well-sorted sandstone with a grain size under 0.5 mm (Figure 6.1c and 6.1d). The clasts are well-rounded mostly spherical. The modal composition of the samples is 83 % quartz, 2 % altered K-feldspar, 5 % cementation (including hematite) and 1 % accessory phases like mica (Table 6.1). The texture is grain-supported, isotropic and without layering. The feldspar grains are significantly smaller than the quartz grains. The porosity is 9 %, the permeability, as an average of 4 samples in permeameter measurements, is 4.0×10^{-17} m^3 and the density 2.13 g cm^{-3} (Schmidt et al., 2016).

By comparing both sandstone types, we see differences in their petrological characterization. The Tennenbach Sandstone is more coarsely grained than the Pfinztal Sandstone, much more homogeneous and has a lower density (2.13 g cm^{-3} against 2.38 g cm^{-3}). The amount of cementation, building the rock matrix, is significantly lower in Tennenbach Sandstone (5 % against 15 % in PfSst).

6.3.2 *Triaxial tests*

The triaxial testing system 'Form + Test Alpha 2-3000 S' at the University of Freiburg was used for laboratory experiments. This triaxial cell has the ability

In vol %	Pfinztal Sst	Tennenbach Sst
Quartz	49	83
K-feldspar	16	2
Muscovite	11	0
Cementation	15	5
Accessories	1	1
Pore space	8	9

Table 6.1: Mineral composition of the two sandstone variations Pfinztal Sandstone and Tennenbach Sandstone used in the triaxial tests (Schmidt et al., 2017)

to perform thermo-mechanical tests with dried samples. The maximum force is restricted to 3000 kN, which is related to a maximum stress of 2387 MPa, by the hydraulic movement of a stamp on the top surface, while the bottom is fixed (Krietsch, 2014). The confining pressure is applied through pressurized oil surrounding the specimen in an outer shrinking tube. The sample is sealed with an inner shrinking tube to prevent an interaction between oil and sample. The oil pressure can sustain a confining pressure of 150 MPa. Heating of the samples up to 200 °C is possible. Due to technical restrictions, the lateral stress or confining pressure is equal in every direction ($\sigma_1 = \sigma_2$). A schematic sketch is shown in Figure 6.2. Due to the findings of Cornet et al. (2007) and Valley and Evans (2007), the triaxial tests had to be carried out at least up to 75 MPa.

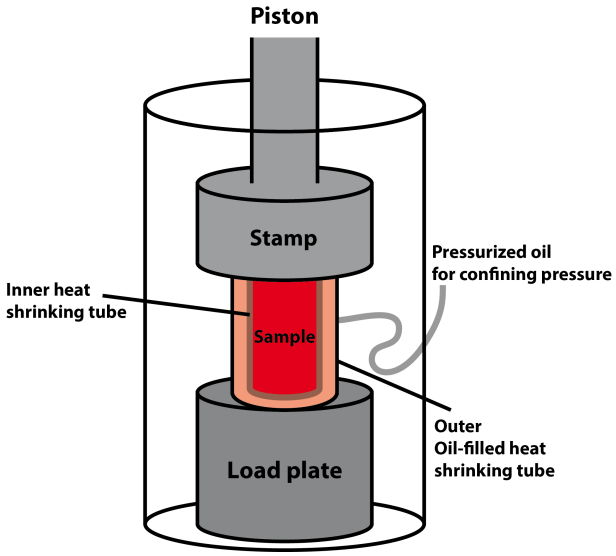

Figure 6.2: Schematic triaxial testing device with its main components

The samples, n = 11 for PfSst and n = 12 for TenSst, have cylindrical shape with a grinded bottom and top surface to reduce friction. The length:width ratio is 2:1 with a length of 80 mm and a diameter of 40 mm. The orientation of the loading axis is perpendicular with respect to the layering of the samples, especially for PfSst. Before conducting the experiments, the samples were dried.

The deformation is applied at the top surface of the sample with a constant displacement rate of $1\,\mathrm{mm\,min^{-1}}$, corresponding to $1.6 \times 10^{-5}\,\mathrm{m\,s^{-1}}$, until the specimen fails. Due to the scope of this study predicting reservoir conditions, experiments with constant confining pressures of $0, 50, 60, 70$ and $90\,\mathrm{MPa}$ have been conducted for each type of sandstone. During the loading, the confining pressure is increased to the predefined limit and then kept constant during final axial loading of the specimen. The temperature is kept constant at room temperature of $20\,^{\circ}\mathrm{C}$ during the changing confinement experiments. Additionally, we carried out triaxial tests with temperatures of $80\,^{\circ}\mathrm{C}$ and $100\,^{\circ}\mathrm{C}$ with a constant confinement of $50\,\mathrm{MPa}$.

During the experiments, the averaged axial displacement and force on the upper surface of the sample and the confining pressure acting on the mantle are measured with an accuracy of $0.1\,\mathrm{mm}$ (displacement), $0.1\,\mathrm{kN}$ (force) and $0.1\,\mathrm{bar}$ (confinement). Due to device limitations, the stamp has a round shape with a diameter of $100\,\mathrm{mm}$ ($A_{stamp} = 0.007\,85\,\mathrm{m^2}$), which is larger than the sample size of $40\,\mathrm{mm}$ ($A_{stamp} = 0.001\,26\,\mathrm{m^2}$) used in the study. Thus, the measured axial force has to be corrected by splitting in force acting on sample (F_{sample}) and force acting on confinement ($F_{confinement}$). The axial stress is corrected and calculated with Equation 6.1:

$$\sigma_1 = \frac{((F_{sample} + F_{confinement}) - \sigma_3 \times (A_{stamp} - A_{sample}))}{A_{sample}} \tag{6.1}$$

Due to the test performance, the axial stress is measured correctly when it exceeds the confining pressure ($\sigma_1 > \sigma_2$) and the force of the stamp is acting mainly on the sample. The material contrast between sample and stamp creates friction at the junction. This leads to an inhomogeneous stress distribution in the sample (Vutukuri et al., 1974). In the case of uniaxial testing ($\sigma_2 = \sigma_3 = 0$), it is possible to measure the lateral or radial deformation with an extensometer. The maximum strength, which the samples can reach with uniaxial setup, is called unconfined compressive strength (UCS). With known axial loading, radial and axial deformation, it is possible to calculate the elastic parameters of the rock samples, like Poisson ratio ν and Young's modulus E, using Hooke's law in the linear elastic part of the deformation (Jaeger et al., 2007).

6.3.3 *Numerical methods*

The numerical evaluation was carried out with the open-source software REDBACK (Poulet et al., 2017), which is based on the THMC-framework MOOSE (Multiphysics Object-Oriented Simulation Environment) (Gaston et al., 2009). MOOSE is a finite-element platform to solve multiphysical problems in an implicit and tightly coupled manner. It acts on unstructured and structured meshes and is highly scalable to work on powerful supercomputers in parallel architectures. The framework uses the finite element libraries of LibMESH (Kirk et al., 2006) and PETSc solver (Balay et al., 2016). The implementation is done in a dimensionless form as single partial differential equations (PDEs). As every kernel is only solving for a single variable, it is possible to activate or deactivate

specific parts of the code to focus on a single problem. The coupling is achieved through linking different variables and processes in an implicit or explicit way.

The application REDBACK (Rock mEchanics with Dissipative feedBACKs) is developed to solve thermo-hydro-mechanical problems in a dimensionless form (Poulet et al., 2017). It is based on the Tensor Mechanics module, which is provided by the MOOSE framework and extends it with additional constitutive models for the overstress plasticity, like von-Mises, Drucker-Prager or modified Cam-Clay (Poulet and Veveakis, 2016).

Mechanical implementation

According to Perzyna (1966), the approach is based on the principles of overstress plasticity. The total strain rate can be divided in a reversible elastic ($\dot{\epsilon}_{ij}^{el}$) and an irreversible plastic (inelastic, $\dot{\epsilon}_{ij}^{pl}$) part (Equation 6.2).

$$\dot{\epsilon}_{ij}^{total} = \dot{\epsilon}_{ij}^{el} + \dot{\epsilon}_{ij}^{pl} \tag{6.2}$$

In Equation 6.3 the elastic deformation and effective stress tensor (σ') evolution follows a linear thermo-elastic law. The first term is the Hooke's law and the second one the volumetric stress triggered by volumetric thermal expansion (λ_s) initiated by temperature changes (ΔT). C_{ijkl} is the elasticity tensor. Since we are focusing on the effects of pressure changes and the samples have been in thermal equilibrium, the second term can be neglected.

$$\sigma'_{ij} = C_{ijkl} \times \dot{\epsilon}_{kl}^{el} - \lambda_s \times \frac{E}{1-2\nu}\Delta T \tag{6.3}$$

Note that the effective stress (σ'_{ij}) in Equation 6.4, due to Terzaghi's principle, is a coupling between the absolute stress (σ_{ij}) and the pore pressure (P_f). The Biot's coefficient (α) takes the bulk modulus and the compressibility of the rock into account (Biot, 1956).

$$\sigma'_{ij} = \sigma_{ij} - \alpha P_f \tag{6.4}$$

If a critical stress defined by the yield surface in the sample is reached, the deformation becomes irreversible and inelastic. The inelastic strain rate tensor can be split into volumetric ($\dot{\epsilon}_{vol}^{pl}$) and deviatoric ($\dot{\epsilon}_{dev}^{pl}$) deformation and follows an associative plastic flow-law (Poulet and Veveakis, 2016) where the strain increment is normal to the yield surface (Equation 6.5).

$$\dot{\epsilon}_{ij}^{pl} = \sqrt{\dot{\epsilon}_{dev}^{pl^2} + \dot{\epsilon}_{vol}^{pl^2}} \times \frac{\delta f}{\delta \sigma'_{ij}} \tag{6.5}$$

The first part, bounded by the root, is a plastic multiplier and f the defined yield function which is related to the effective stresses. The deviatoric ($\dot{\epsilon}_{dev}^{pl}$) and volumetric ($\dot{\epsilon}_{vol}^{pl}$) strain rate tensor are calculated with Equation 6.6a and 6.6b.

$$\dot{\epsilon}_{dev}^{pl} = \dot{\epsilon}_0 \times \langle \frac{q - q_y}{\sigma_{ref}} \rangle^m \tag{6.6a}$$

$$\dot{\epsilon}_{vol}^{pl} = \dot{\epsilon}_0 \times \langle \frac{p' - p_y}{\sigma_{ref}} \rangle^m \tag{6.6b}$$

$\dot{\epsilon}_0$ is the reference strain rate, m an exponent, q the deviatoric stress, p' the effective mean stress, q_y and p_y are the stresses at yield, while σ_{ref} is the reference stress. The Macaulay brackets in Equation 6.6 ensure zero plastic deformation before touching the yield surface. During plastic deformation, the consumed energy or work can be decomposed in stored energy and dissipated energy (Chrysochoos et al., 1989). The related temperature change was observed mainly in metals (Johnson et al., 1964). A Drucker-Prager (DP) yield envelope (Equation 6.7) is used to numerically quantify the starting point of plastic deformation (Drucker and Prager, 1952). This DP-criterion is a linear, time-independent and pressure-dependent criterion, where the deviatoric yield stress (q_y) is a function of the volumetric mean yield stress p_y with a given slope (M) and known initial yield stress (q_{y0}). These parameters are measureable with the conducted triaxial tests.

$$q_y = q_{y0} + p_y M \tag{6.7}$$

Another empirical criterion for brittle behavior of porous medium type materials, like sandstone, was used by Khan et al. (1991) and applied to a wide range of different sandstones by Wong et al. (1997) and Cuss et al. (2003). This criterion describes the relationship between differential and hydrostatic stress in brittle regimes as a parabola with a maximum reachable differential stress ($q_{y,max}$) and mean stress ($p_{y,max}$, Equation 6.8). When this maximum stress is reached, the samples will undergo compactive behavior until grain crushing occurs. Rutter and Glover (2012) take up this concept of changing behavior and refer the critical differential stress to linear increase with a slope of 1.18 ± 0.03.

$$q_y = q_{y,max} - (\frac{q_{y,max}}{1 - p_{y,max})^2} \times (p_y - p_{y,max})^2) \tag{6.8}$$

Coupled hydro-mechanical behavior

To evaluate the influence of stress and strain on porosity and permeability, a poroelastic approach is considered (Zimmerman, 2000). The sample is treated as a porous medium with a solid skeleton and voids in between. The remaining porosity (ϕ) is defined as initial porosity (ϕ_0) and the changes of interconnected pore volume, related to mechanical deformation, elastic ($\Delta\phi_{mech}^{el}$) and plastic ($\Delta\phi_{mech}^{pl}$, Equation 6.9) (Poulet and Veveakis, 2016).

$$\phi = \phi_0 + \Delta\phi_{mech}^{el} + \Delta\phi_{mech}^{pl} \tag{6.9}$$

With Equation 6.10:

$$\Delta\phi_{mech}^{el} = (1 - \phi)(\beta_s \Delta P_f - \lambda_s \Delta T + \Delta\epsilon_{vol}^{el}) \tag{6.10a}$$

$$\Delta\phi^{pl}_{mech} = (1-\phi)\Delta\epsilon^{pl}_{vol} \tag{6.10b}$$

Where $(\beta_s \Delta P_f)$ is related to the compressibility of the solid due to pore pressure increase, $(\lambda_s \Delta T)$ the thermal expansion of the solid phase due to temperature increase and $(\Delta\epsilon^{el}_{vol})$ to elastic changes in the volume of the sample. $(\Delta\epsilon^{pl}_{vol})$ is the increment in volumetric plastic strain. Note that $\Delta\phi^{el}_{mech}$ is typically negative in compressional regimes. No pore pressure or temperature changes are assumed, the changes in hydraulic-related rock parameters only depend on the volumetric change during deformation and the reduction of pore space.

Modeling

The 3D unstructured finite-element mesh is created in Gmsh (Geuzaine and Remacle, 2017), representing a cylinder with a length:width ratio of 2:1. No artificial flaws or weak zones are added, to guarantee comparable results with the experiments carried out with the triaxial testing equipment. The modeling itself will be implemented in two steps. In the first step, the hydrostatic loading ($\sigma_1 = \sigma_2 = \sigma_3$) is applied to the sample. A Neumann boundary condition is acting on the mantle, bottom and top surfaces to apply a homogeneous stress field and resulting displacement of the whole mesh (Figure 6.3). In the second step, the calculated displacements of the previous step are applied to the mesh as an initial condition. The bottom and top surfaces are constrained in x- and y-directions, the bottom additionally in the z-direction, to guarantee comparability to the experimental results. The upper boundary is displaced in the z-direction as a function of time in agreement with the triaxial experiments, while the stress acting on the mantle is kept constant. Since the focus is on the deformation processes and their coupled effects on sample and reservoir scale, the experimental results are averaged and used as constant input parameters for the numerical evaluation (Khajeh, 2013; Settari et al., 2013).

6.4 RESULTS

6.4.1 *Triaxial tests*

For both types of sandstone (Pfinztal and Tennenbach Sandstone) uniaxial and triaxial tests have been carried out. For the uniaxial tests the axial and radial displacement and axial force were measured to calculate the Poisson's ratio and axial stress. The final Poisson's ratio is the average of at least five calculated values to decrease the uncertainty of natural inhomogeneities, which have a strong influence in unconfined samples. Thus, the Poisson's ratio for PfSst is 0.14 ± 0.03 and for TenSst 0.24 ± 0.04. For the triaxial tests, the axial and radial force and axial displacement was measured to calculate the acting stresses. We focused our triaxial tests between 50 and 90 MPa due to reservoir conditions. Figure 6.4 shows selected stress-strain curves for a confining pressure of 50 MPa for TenSst and PfSst.

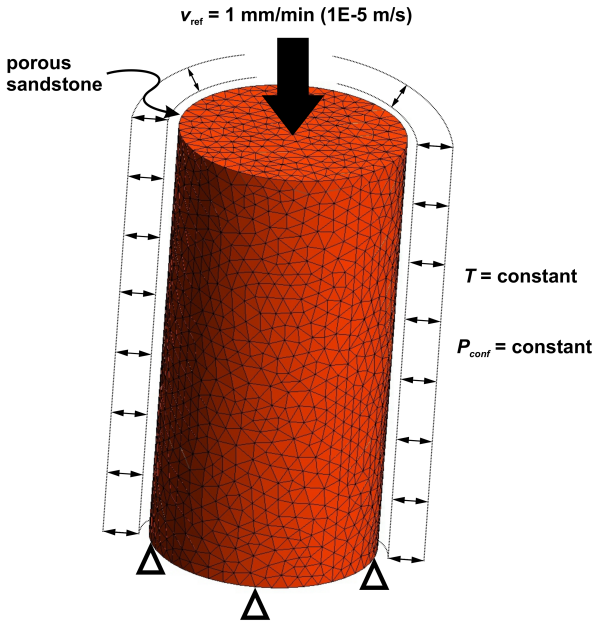

Figure 6.3: The applied FE mesh and applied boundaries for the numerical evaluation.

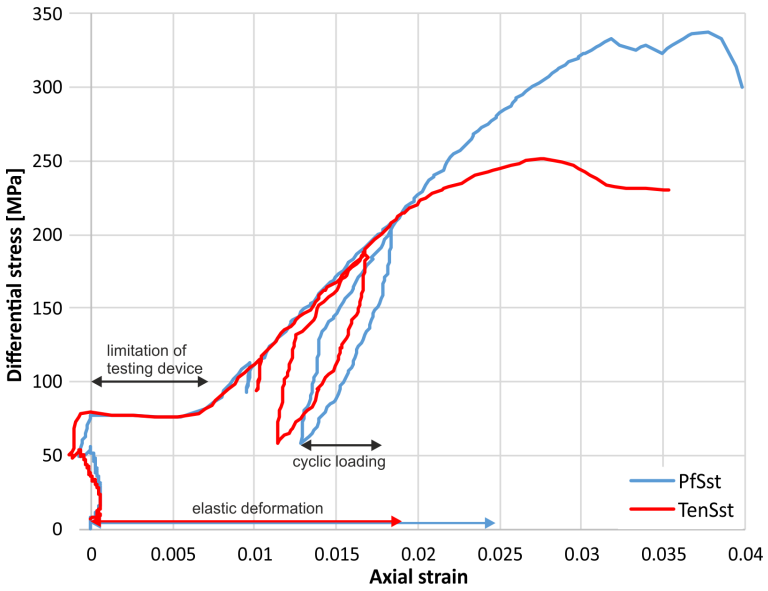

Figure 6.4: Exemplary differential stress–strain curves for PfSst and TenSst with a confining pressure of 50 MPa, showing the deformation of the two samples. The non-linear behavior for low stresses (strain up to ≈ 0.007) is related to limitations of the testing device and the application of the confining pressure.

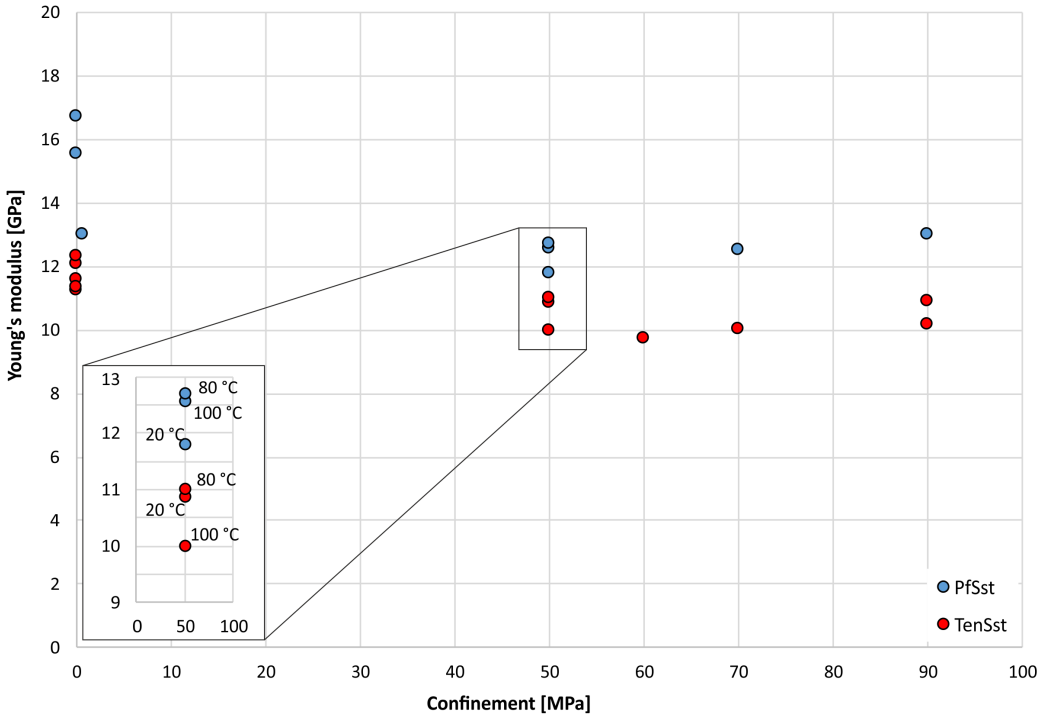

Figure 6.5: Young's moduli related to the confinement of the samples for PfSst and TenSst; the tests were performed at room temperature, except for two samples with higher temperatures (80 °C and 100 °C). Not shown are values above 20 GPa for PfSst (see Table 6.2).

With known strain and stress in the linear elastic part of the deformation, the Young's modulus is calculated. Figure 6.5 and Table 6.2 show the experimental results for the samples of both sandstone types. Generally, the uniaxial tests lead to higher Young's moduli than the triaxial tests. Thus, for example, the Young's modulus for Pfinztal Sandstone is in the range between 12.5 and 26.4 GPa, while the mean value for the confined samples is significantly lower (13.4 ± 1.5 GPa). The overall average of the Young's modulus of Tennenbach Sandstone is 10.9 ± 0.8 GPa. Most of the experiments were carried out at 20 °C. Two samples of both sandstones, with a confinement of 50 MPa, have been tested at 80 °C and 100 °C. These tests show similar Young's moduli without a significant visible influence of temperature (Figure 6.5). The averaged results and their uncertainty are shown in Table 6.3. To calculate the mechanical properties of the reservoir, the estimation of the maximum applicable stress until material failure occurs is necessary.

The comparison of the experimental results shows that the elastic modulus of the Pfinztal Sandstone is higher than the Tennenbach Sandstone (13.4 GPa compared to 10.9 GPa) (Table 6.2 and Figure 6.5). *UCS* and the slope of linear regression line between differential stress and mean stress is higher for PfSst, as well. Due to the higher Poisson's ratio, the effect of axial deformation on lateral deformation is higher in TenSst. The failure strength of both analogues shows

	Density [kg m^{-3}]	Conf. pressure [MPa]	Max. diff. stress [MPa]	Young's modulus [GPa]	Poisson's ratio [-]	Temp-ature [°C]
Pfinztal Sandstone						
PfSst_10	2290	0	-	13.0	0.18	20
PfSst_12	2400	0	114	16.7	0.12	20
PfSst_13	2540	0	114	15.6	0.19	20
PfSst_16	2460	0	-	25.7	0.14	20
PfSst_17	2380	0	-	26.8	0.1	20
PfSst_18	2380	0	142	26.4	0.11	20
PfSst_11	2280	50	337	11.8	-	20
PfSst_28	2430	50	352	12.6	-	100
PfSst_29	2400	50	366	12.7	-	80
PfSst_14	2320	70	433	12.5	-	20
PfSst_15	2290	90	471	13.0	-	20
Tennenbach Sandstone						
TenSst_9	2020	0	-	12.1	0.23	20
TenSst_11	2090	0	42	11.6	0.27	20
TenSst_14	2250	0	46	11.3	0.2	20
TenSst_15	2170	0	47	11.5	0.24	20
TenSst_18	2170	0	-	12.4	0.28	20
TenSst_13	2070	50	251	10.9	-	20
TenSst_26	2070	50	256	10.0	-	100
TenSst_27	2070	50	243	11.0	-	80
TenSst_24	2190	60	282	9.7	-	20
TenSst_16	2030	70	310	10.0	-	20
TenSst_17	2030	90	332	10.2	-	20
TenSst_28	2070	90	358	10.9	-	20

Table 6.2: Experimental data for PfSst and TenSst from uniaxial and triaxial experiments

a linear trend with increasing confinement with a slope of 1.80 (PfSst) and 1.63 (TenSst) (Figure 6.7).

The results of the triaxial tests for PfSst and TenSst are summarized in Table 6.3 and have been applied to the numerical evaluation. The results of the triaxial tests show that at reservoir depth no mechanical failure is expected.

	Pfinztal Sst	Tennenbach Sst
Young's modulus [GPa]	13.4 ± 1.5	10.9 ± 0.8
Poisson ratio [-]	0.14 ± 0.03	0.24 ± 0.03
Porosity [%]	8	9
Density [$kg\,m^{-3}$]	2380 ± 77	2130 ± 110
Initial yield stress [MPa]	36.0	16.1
Displacement top [$m\,s^{-1}$]	1.6×10^{-5}	1.6×10^{-5}
Slope yield surface [-]	1.80	1.63
Confinement [MPa]	0˜90	0˜90

Table 6.3: Summary of the relevant data and uncertainty for PfSst and TenSst

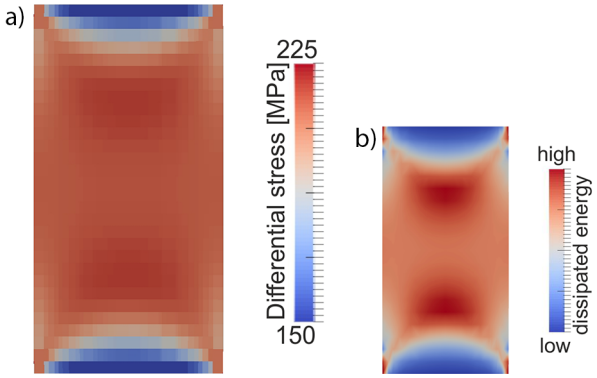

Figure 6.6: a) Exemplary differential stress distribution, before maximum stress is reached, for Tennenbach Sandstone with a confinement of 50 MPa simulated with REDBACK. b) The energy dissipation for the same sample

6.4.2 *Numerical modeling*

Maximum stress

The mechanical properties, calculated from the results of the triaxial tests (Table 6.3), are used as input parameters for the numerical simulation. All input parameters are assumed to be constant, and natural heterogeneities are neglected. We used the elastic law and overstress plasticity described in Equation 6.2 to 6.5, to predict the maximum stress the reservoir rocks can withstand. The yield surface, where irreversible deformation starts, is determined with Equation 6.7, and applied to the samples depending on the confining pressure.

Due to modeling as FE-mesh (Figure 6.3), the stress distribution in the sample can be visualized. Stress maxima are visible along an 'elongated cross', which is a result of the constrained upper/lower boundary of the numerical sample and expected in the experiments as well (Vutukuri et al., 1974). Figure 6.6a shows exemplary the stress distribution in the sample Tennenbach Sandstone at a confining pressure of 50 MPa. Additionally, it is possible to show the qualitative amount of dissipated energy during irreversible deformation (Figure 6.6b) leading to temperature increase, both not measurable in the triaxial experiments.

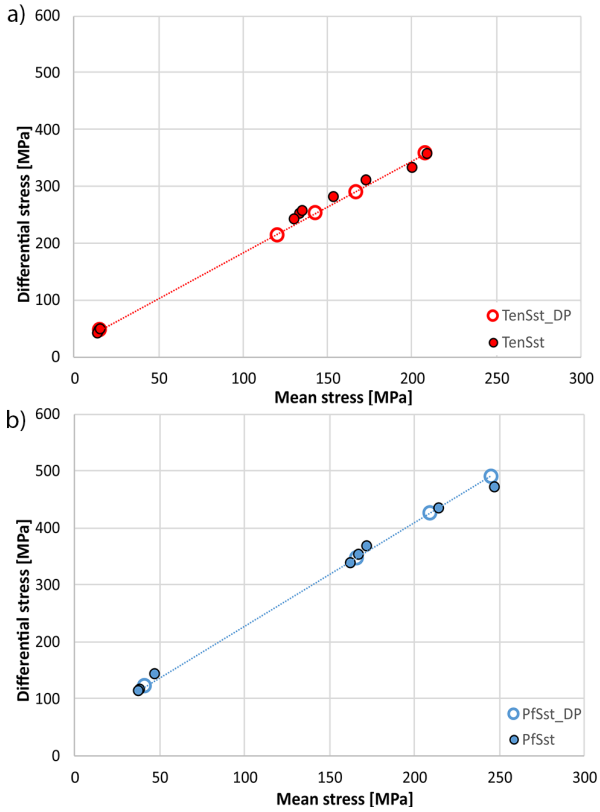

Figure 6.7: Comparison of experimental results (points) and numerical evaluation (circles) for sample failure with Drucker–Prager yield criterion for TenSst (a) and PfSst (b)

Figure 6.7 shows the comparison between the experimental and numerical results for Pfinztal Sandstone and the Tennenbach Sandstone. The confining pressures are assumed to be identical. The modeling for 90 MPa seems to slightly overestimate the differential stress compared to the results in the experiment. Measured and calculated results are in good agreement with a maximum difference of 19 MPa.

6.5 IMPACT ON PORO-PERM RELATION

To calculate the hydraulic parameters as a result of mechanical deformation we use the initial confined modeling step with differential stress $q = 0$ and $p = \sigma_1 = \sigma_2 = \sigma_3$, corresponding to hydrostatic conditions, expected in the reservoir. Porosity changes are related to volume changes in the sample, caused by volumetric deformation equally in the experiments and model. Thus, the hydrostatic compression has the most important influence on the remaining porosity. To calculate the porosity under these conditions, we used Equation 6.9 and 6.10. Figure 6.8 shows the remaining porosity depending on the confining pressure. Porosity decreases for PfSst from initially 8 % to 6.6 % at a circumferential stress of 90 MPa and for TenSst from 9 % to 7.8 % at 90 MPa.

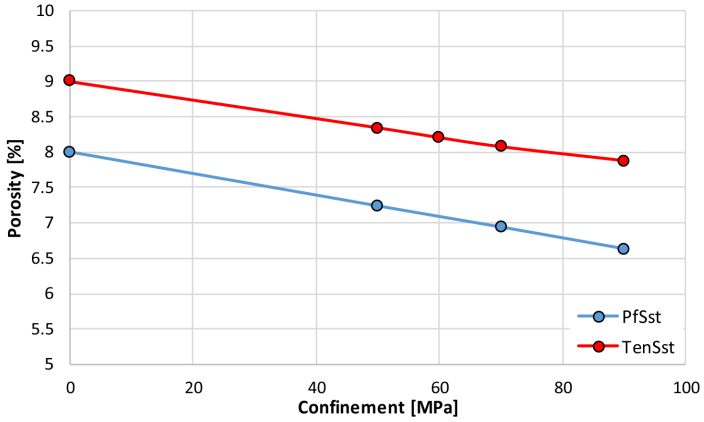

Figure 6.8: Porosity changes under hydrostatic conditions for PfSst and TenSst

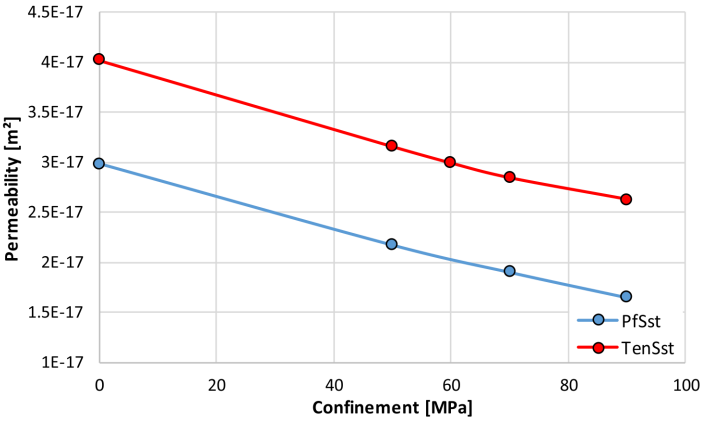

Figure 6.9: Permeability changes due to hydrostatic loading calculated from porosity changes for PfSst and TenSst

Beside porosity, permeability is a key factor for evaluating the performance of a reservoir, e.g. for geothermal usage. It describes the transport of fluid and energy through the porous medium. To quantify the effect of porosity changes (ϕ) to permeability changes (k) the fundamental Kozeny-Carman relationship is used as a reference model (Carman, 1956). More specific models and extensions to Kozeny-Carman, e.g. the fractal pore space model for sedimentary rocks, have been developed to describe this relationship (Pape et al., 2000). With known initial porosity (ϕ_0) and initial permeability (k_0), this relationship can be expressed as Equation 6.11 (Jacquey et al., 2015).

$$k = k_0 \frac{(1-\phi_0)^2}{\phi_0^3} \frac{\phi^3}{(1-\phi)^2} \tag{6.11}$$

Figure 6.9 shows the permeability evolution of Pfinztal and Tennenbach Sandstone. The values are related to the changes in porosity. The permeability decreases for PfSst from initially $3.0 \times 10^{-17}\,\mathrm{m}^2$ to $1.6 \times 10^{-17}\,\mathrm{m}^2$ for a hydrostatic stress of 90 MPa and TenSst from initially $4.0 \times 10^{-17}\,\mathrm{m}^2$ to $2.6 \times 10^{-17}\,\mathrm{m}^2$.

6.6 DISCUSSION

6.6.1 *Triaxial experiments and numerical modeling*

The static Young's moduli of the different sandstone types are shown in Figure 6.5. The scattering of the unconfined Young's modulus for the PfSst (between 13 and 25 GPa) is related to material heterogeneities like initial microcracks, grain size, cementation and porosity differences between the different samples and the testing device itself (Dunn et al., 1973; Palchik, 1999). The impact of these heterogeneities and flaws decreases with increasing confining pressure since a preconsolidation of the sample is applied with the confinement step (e.g. Zoback, 2011). Additionally, the part of linear elasticity is limited in uniaxial tests which leads to a higher uncertainty in the evaluation of the mechanical parameters compared to triaxial tests with higher absolute strains. The average values of PfSst (13.4 GPa) and TenSst (10.9 GPa) are comparable with measurements from other sandstone types (Cuss et al., 2003; Wong et al., 1997). The majority of these values are in the range of 0 to 30 GPa, with some scattering to 74 GPa. The Young's modulus of Vosges Sandstone is calculated using the slope of the stress-strain ratio (linear part). It is in the range of 12 to 13 GPa (Bésuelle, 2001). Chang et al. (2006) have shown, that Young's modulus and UCS reduce with increasing porosity. The porosity for the Buntsandstein probes used in this study is low (PfSst 8 % and TenSst 9 %) compared to other reservoir sandstones (> 10 %) (Chang et al., 2006) but fits with data reported by Bauer et al. (2017) for Buntsandstein analogues. To predict the failure, calculating the UCS, as initial failure strength under uniaxial loading, is important. The data in Chang et al. (2006) show indeed a positive correlation between Young's modulus and UCS for 260 sandstone samples, but a large variety of value pairs is observed and no precise trend is visible. However, the data of Chang et al. (2006) are in accordance with our samples of PfSst (123 MPa), TenSst (46 MPa) and VsSst (35 MPa), as well. Bauer et al. (2017) reports UCS values in the range of 80 – 100 MPa for the Buntsandstein in the northeast URG.

The mechanical parameters for both investigated sandstones (Young's modulus and failure strength) show no measureable dependency on temperature up to 100 °C (Figure 6.5 and 6.7). This agrees with the findings of Ranjith et al. (2012) and Serdengecti and Boozer (1961), who demonstrate temperature sensitivity to be observed only for temperatures above 400 °C.

Failure stress prediction

We compare the results of our triaxial tests on TenSst and PfSst samples with the linear criterion of Drucker and Prager (1952) (Equation 6.7), the parabolic envelope used by Khan et al. (1991) for brittle failure (Equation 6.8) and the critical state line of Rutter and Glover (2012), with a slope of 1.2, to find the best criterion for inter- and extrapolation to simulate reservoir conditions. Figure 6.10 shows the results and the comparison in the normalized q-p space. The normalization is applied with respect to a grain crushing pressure $p*$, which is a function of porosity*grain radius, presented by Rutter and Glover (2012) and

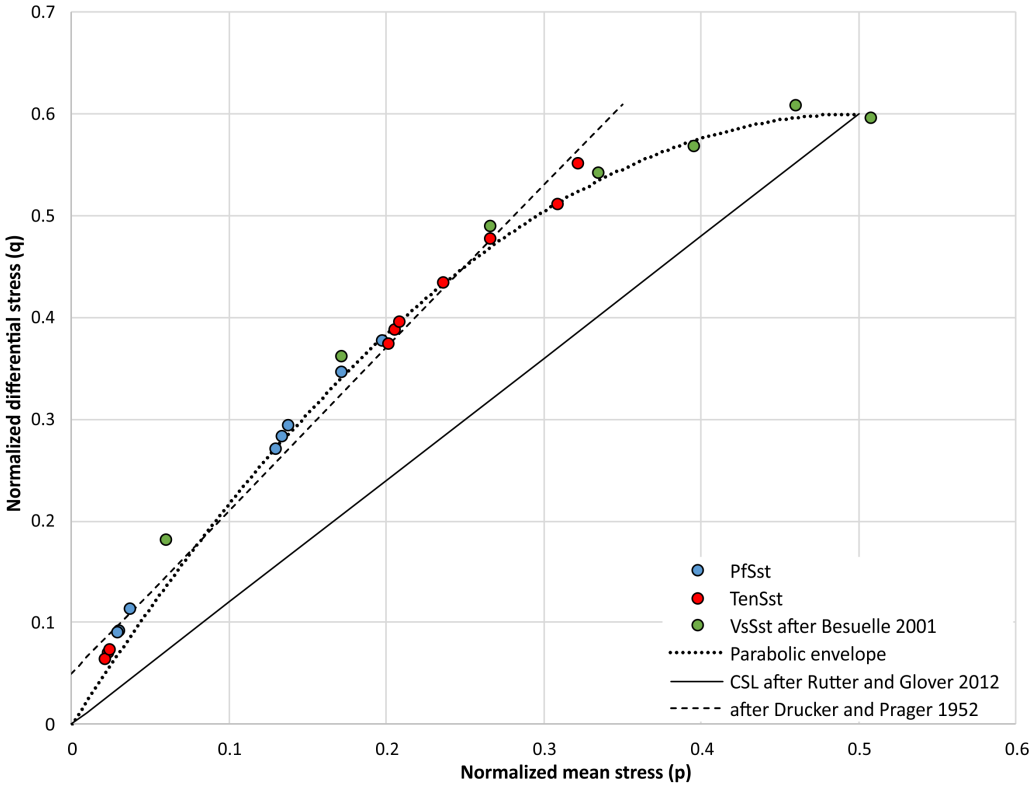

Figure 6.10: Maximum differential stress of the different sandstones types PfSst (blue), TenSst (red) and VsSst (green). The results are compared with the criteria of Drucker and Prager (1952), Khan et al. (1991) and the concept of CSL (Rutter and Glover, 2012) in normalized $q^{\vee}p$ space

Zhang et al. (1990). High grain sizes reduce the potential maximum stresses, which is commonly known as Hall-Petch relationship (Chokshi et al., 1989). Additionally, the data of Bésuelle (2001) of the Vosges Sandstone (VsSst) are presented in Figure 6.10. They show a reasonable fit with a maximum difference of 0.04 to the parabolic criterion used by Khan et al. (1991) with a maximum of $p = 0.5$ and $q = 0.6$. The results of TenSst and PfSst correspond well with both (linear and parabolic) criteria up to a normalized mean stress of 0.3. The linear plot is averaged through both sample types with a slope of 1.6 and an initial normalized differential stress of 0.05. The data points for the confined samples of TenSst are closer to the maximum differential strength of this sample type which results in a lower maximum stress resistivity.

The parabolic envelope used by Khan et al. (1991) starting at $x/y = 0/0$ in the coordinate system's origin underestimates the failure strength for low confining pressures of both sandstone samples. The accuracy for differential stress prediction is in the range of possible reservoir stresses, between 50 and 80 MPa, 0.02 for normalized differential stress, while a slight overestimation of the maximum failure strength is possible. For higher confining pressures, at which the expected transition from brittle to compactive failure takes place, no data are available. Nevertheless, these absolute stresses are out of range for a possible URG reservoir as described in the geological overview. The expected

failure stress for the criterion of Drucker and Prager (1952) fits well for normalized mean stresses up to $0.27(\pm 0.03)$ or absolute 210 MPa for TenSst and PfSst in both, triaxial experiments and modeling (Figure 6.7).

Hydraulic implications

The porosity and permeability of Tennenbach and Pfinztal Sandstone have been quantified in advance by thin section and permeability tests. REDBACK allows the coupling of mechanical deformation with hydraulic feedback. Thus, it is possible to quantify the porosity and permeability changes due to compressive loading and volumetric changes by using Equation 6.9 to 6.11. The results are shown in Figure 6.8 and Figure 6.9. Porosity is decreasing from initially 8 % to 6.6 % (PfSst) and from 9 % to 7.8 % (TenSst), corresponding to a total reduction of 17.5 % and 13.3 %, respectively. The permeability decreases from $3.0 \times 10^{-17}\,m^2$ to $1.6 \times 10^{-17}\,m^2$ (PfSst) and from $4.0 \times 10^{-17}\,m^2$ to $2.6 \times 10^{-17}\,m^2$ (TenSst), which is a drop of 46.6 % and 35 %, respectively.

The Kozeny-Carman equation depends on different parameters of the pore geometry like a geometric factor, tortuosity and surface area, and assumes steady laminar flow. However, the calculation of the exact value is rather complex because the surface area, as the most relevant factor, is typically unknown. Equation 6.11 assumes a bed of spheres with fully interconnected pores and a constant geometric factor (Hassanzadegan and Zimmermann, 2014), while changes in pore deformation and connection have been neglected.

6.6.2 *Effects on upscaling*

The extrapolation and upscaling of the results to reservoir conditions is limited to a certain extent related to the samples, experiments, modeling approach and to the reservoir itself, as described below. Experiments and modeling assume fully dry conditions, while a geothermal reservoir is saturated under hydrostatic or sometimes even over-pressure conditions. Positive changes in pore pressure, for example caused by fluid injection or compaction, would increase the porosity in the sphere of influence related to Equation 6.9 and decrease the effective stress acting on the sample (Biot, 1956). On the other hand, a decrease in temperature, for example by cold water injection, will increase the porosity as well due to volume reduction of the solid phase (Equation 6.9). A generalization was made in terms of hydrostatic stress conditions because the poly-axial behavior is unknown, but it could lead to changes in stress distribution. Taking these considerations into account, a lower decrease of porosity and permeability in the reservoir is expected.

The scale of the sample in triaxial tests is limited due to technical reasons. The internal setup of the large-scale reservoir is typically unknown, containing material heterogeneities as well as faults and fractures. For the numerical evaluation, we assumed a homogeneous and non-fractured sandstone body for comparison reasons with analogue studies (triaxial tests). This assumption is limited since first of all, the sedimentary rocks of the URG have strongly varying facies (Bauer et al., 2017), leading to a substantial heterogeneity in the mechanical parameters,

like UCS. Values between 35 and 123 MPa are reported for the Buntsandstein. Additionally, due to the deformation history of the URG, the Buntsandstein is characterized by various fault and fracture networks, affecting the mechanical and hydraulic parameters of the reservoir rock (Meixner et al., 2014). It is commonly assumed that rocks in the vicinity of fractures have no or strongly reduced cohesion (Jaeger et al., 2007), leading to a lower stress resistance. (Vutukuri et al., 1974) reported that the rock strength is mainly affected by the largest crack. A larger sample or reservoir may have larger cracks, leading to a decrease in overall rock strength. So, the results tend to overestimate the resistivity of the reservoir rock (Chang et al., 2006).

On the other hand, fractures affect the permeability and porosity of the reservoir directly (Stober and Bucher, 2015), while the matrix is acting more or less as a storage. Thus, fractures are preferable pathways for fluids when critical stresses are observed and dilatancy or shear displacement take place (Barton et al., 1995). The permeameter measurements ($4.0 \times 10^{-17}\,m^2$ and $3.0 \times 10^{-17}\,m^2$, respectively) are in good accordance to the relatively small values derived by core samples of the Buntsandstein (Stober, 2014). As described before, the permeability is a combination of matrix and fractures. Stober and Bucher (2015) reported an averaged formation permeability of $5 \times 10^{-15}\,m^2$. Analogues of the eastern border of the URG show comparable matrix porosities between 3 % and 8 % (Bauer et al., 2017). On the other hand, alteration, like remineralization and precipitation of new minerals along fractures, can decrease the fracture permeability (Schmidt et al., 2017; Stober and Bucher, 2015). Therefore, the chances of successful upscaling results from analogue studies to reservoir conditions is higher for formations with less complex internal structures like sedimentary basins, where porous media flow is the dominant process for transporting energy.

6.7 SUMMARY AND CONCLUSIONS

By means of triaxial tests realized on analogue rocks of the Buntsandstein formation of the URG, it is possible to predict the mechanical behavior of a possible geothermal reservoir rock under deformation in a general way. Two different types of Buntsandstein analogues, Tennenbach and Pfinztal Sandstone, have been investigated for mechanical and hydraulic characterization. Hydraulic tests show a low natural porosity of 9 % (TenSst) and 8 % (PfSst) and a permeability of $4.0 \times 10^{-17}\,m^2$ (TenSst) and $3.0 \times 10^{-17}\,m^2$ (PfSst). The Young's moduli, determined with the aid of triaxial tests, are in the range of 11 to 13 GPa and the Poisson's ratio is 0.24 (TenSst) and 0.14 (PfSst).

Uniaxial and triaxial tests were conducted to gain information concerning their geomechanical behavior under in-situ conditions. For the triaxial tests, the confining pressure for every setup was kept constant between 50 MPa and 90 MPa at room temperatures and additionally for a confining pressure of 50 MPa at temperatures of 80 and 100 °C. The experiments showed that an increase in horizontal stress, as confining pressure, leads to higher maximum stresses on the vertical axis. The maximum differential stress at a confining pressure of 90 MPa is 358 MPa (TenSst) and 471 MPa (PfSst). An influence of temperature

was not visible. The measured stresses have been compared to different kinds of failure criteria to predict failure stress and for interpolation purposes. The rock-dependent parabolic failure envelope used by Khan et al. (1991)and the general criteria of Drucker and Prager (1952) are in good agreement with the triaxial experiments of TenSst and PfSst in the conducted stress regime expected in the URG (Figure 6.10). For the weaker VsSst, the Drucker-Prager criterion leads to a strong overestimation of the maximum reachable stress (Figure 6.10). The high stress resistivity of TenSst and PfSst to vertical stresses under confinement suggests that the rocks are in the elastic range of deformation in the Buntsandstein horizon.

Numerical modeling of the triaxial tests with the MOOSE framework allows us to have a look inside the rock sample and to quantify the stress maxima not homogeneously located within the specimen. Stress- and deformation-induced volume changes lead to void space reduction preferentially along the zone of increased deformation. With known initial porosity and permeability (hydraulic tests with a permeameter) and the change in porosity (calculated in the numerical model), the change in matrix permeability can be evaluated using a Kozeny-Carman relationship. Thus, the porosity is reduced to 7.8 % (TenSst) and 6.6 % (PfSst) and the permeability to 2.6×10^{-17} m^2 (TenSst) and 1.6×10^{-17} m^2 (PfSst), applying an isotropic stress of 90 MPa to the sample. This corresponds to a drop in permeability of 46.6 % (PfSst) and 35 % (TenSst) respectively. Measurements of these parameters during deformation and after failure can help to verify these results and decrease the uncertainty related to the approach applied.

For complex geological structures, like the fault-related Buntsandstein reservoir in the Upper Rhine Graben, large uncertainties in predicting the mechanical and hydraulic behavior are expected. Fault and fracture architecture can affect the hydraulic characteristics by improving or inhibiting fluid flow, depending on the interaction of different factors, e.g. lithology, displacement, temperature or time (Caine et al., 1996). Thus, it is necessary to investigate the mechanical behavior of reservoir rocks in the vicinity and within fault and damage zones when natural or artificial changes in the effective stress field occur. On the other hand, for more homogeneous reservoirs, like sedimentary basins, our results can provide an increased knowledge of the target horizon with higher accuracy.

The benefit of numerically modeling the triaxial tests is the possibility to pinpoint, quantify and separate the various processes which take place during deformation in the sample and on the boundaries in a scale-independent manner. This promotes an understanding of how different parameters, like *UCS*, Young's modulus or Poisson's ratio, affect the mechanical behavior on a smaller as well as on reservoir engineering scale. We can use these mechanical implications to evaluate the influence of natural and artificial stress changes, e.g. in the vicinity of wells, on hydraulic-related parameters, like permeability and porosity. In general, our results can help to fill the gap between borehole data and their transferability to reservoir scale.

ACKNOWLEDGMENTS

This study is part of the project 'GeoFaces' supported by the Federal Ministry for Economic Affairs and Energy (BMWi) (No. 0324025C). Special thanks to Prof. Dr. T. Kenkmann and Hannes Kriesch (both University of Freiburg), which helped to conduct the experimental results. Special thanks to Dr. Max Peters, who introduced into the MOOSE framework. Particular thanks to the two anonymous reviewers, which helped to improve the quality of the paper.

7

IMPLICATIONS ON LARGE-SCALE FLOW OF THE FRACTURED EGS RESERVOIR SOULTZ INFERRED FROM HYDRAULIC DATA AND TRACER EXPERIMENTS

This chapter is published in Geothermics 84, doi: 10.1016/j.geothermics.2019.101749.

ABSTRACT

The Enhanced geothermal system in Soultz-sous-Forêts, located in the geothermal favorable Upper Rhine Graben, is a fracture-controlled reservoir that was highly investigated in the last decades generating a huge geoscientific database. Numerical reservoir models use this database to simulate the operation of the subsurface heat exchanger, yet suffer from simplifications regarding the transfer of experimental into model data, dimensional extension, and computational power and efficiency. The new extensive transient 3D simulations, based on geophysical, geological and hydraulic data, highlight the hydraulic and transport feedback of the Soultz EGS due to convective and advective fluid flow. Developed with the goal of simulating the vast tracer test data during the reservoir-testing phase in 2005, the Finite Element Model is focusing on the main fractured zones, which connect the wells in the deep reservoir. It comprises 13 major hydraulically active faults and fractures in a $13 \times 11 \times 5$ km extending model domain, as well as open-hole sections of the wells GPK1 to GPK4 and their casing leakages. The simulation of the tracer experiment confirms the strong heterogeneity of the reservoir and highlights the importance of a potential fractured zone, hydraulically separating the reservoir in a northern (GPK1 to 3) and southern section (GPK4). This zone tends to connect the reservoir to the main fault system by hydraulically separating GPK4 from the other wells. The calibration and sensitivity analyses provide a unique, broad understanding of the reservoir flow zones providing information on the extension of the Soultz reservoir in the future and on the fluid pathways in the deep subsurface of the Upper Rhine Graben.

7.1 INTRODUCTION

The Upper Rhine Graben (URG) is one of the most distinct areas in central Europe for the utilization of geothermal energy. Favorable thermal conditions with gradients of greater than $100\,\mathrm{K\,km^{-1}}$ (Pribnow and Schellschmidt, 2000) have led to the development of several successful power plant projects targeting the hydrothermal sedimentary cover and the deep crystalline basement of the

URG as Enhanced Geothermal System (EGS) (Genter et al., 2016; Vidal and Genter, 2018). EGS are designed to take advantage of natural permeable faults and fractures and improve their natural hydraulic properties through chemical and hydraulic stimulation (Schindler et al., 2010). One of the first and most prominent European EGS is located at Soultz-sous-Forêts (Garnish, 2002; Gérard et al., 2006), targeting a fractured geothermal reservoir in a depth of up to 5000 m and temperatures up to 200 °C (Genter et al., 2010). Starting in the 1980s, a unique scientific database has been created, which opens the opportunity to study hydraulic processes in the geothermal reservoir, and especially along faults and fractures and on the matrix-fracture-interface (Genter et al., 2010; Sausse et al., 2010).

Various experiments, such as tracer and circulations tests, were conducted to characterize and quantify fluid flow through a single fracture or fracture networks not only in the Soultz EGS but in laboratory and field experiments worldwide (Berkowitz, 2002). In laboratory scale, single fracture geometries were often described as self-affine rough surfaces with varying apertures exposed to laminar and/or turbulent fluid flow (Schmittbuhl et al., 2008). Meter-scale migration experiments, conducted in Underground Research Laboratories, considered fractures as shear zones with a high number of small discrete channels (Hadermann and Heer, 1996). Typically, Darcy flow was assumed within the shear zone (Moreno et al., 1988). In the reservoir scale, the geometry, interconnection, and behavior of fractures are sparsely known and accessible since wellbores and experiments provide point-like information of shape and fracture density (Dezayes et al., 2010) while geophysical measurements show the spatial distribution (Sausse et al., 2010). Detailed information about the reservoir hydraulics, including the reservoir fluid migration pathways, mean residence times, swept pore volume and heat exchange area between different wells, can be achieved using inter-well tracer experiments (Robinson and Tester, 1984). In the past, several tracer experiments were conducted in enhanced geothermal reservoirs which, however, were assumed to be simplified connections between two wells as a single planar structure or ideal fracture network when attempting to model (Ayling et al., 2016; Ghergut et al., 2016; Iglesias et al., 2015; Karmakar et al., 2016; Rose et al., 2009; Sanjuan et al., 2006).

An elegant way to resolve arisen issues of missing spatial information and unconnected data is to simultaneously apply structural and numerical models for investigating the natural and forced hydro-thermal processes of an EGS (O'Sullivan et al., 2001). Various numerical studies of the Soultz geothermal reservoir have been conducted over decades for investigating different physical processes, such as natural convection (Bächler et al., 2003; Guillou-Frottier et al., 2013; Kohl et al., 2000; Vallier et al., 2019) and the effects of mechanical stimulation to the reservoir performance (Baujard and Bruel, 2006; Kohl et al., 2006; Kohl and Mégel, 2007). Furthermore, inter-well circulation was investigated by fitting analytical and numerical solutions to the measured tracer data. Sanjuan et al. (2006) applied an analytical dispersive transfer model while Blumenthal et al. (2007) and Gessner et al. (2009) presented simplified models for the direct circulation between GPK3 and GPK2 wells. Kosack et al. (2011) compared three different inversion methods to evaluate their applicability to the connection

between GPK3 and GPK2. Vogt et al. (2012) applied the Ensemble Kalman Filter (EnKF) to individually invert for the concentrations measured at GPK2 and GPK4. Gentier et al. (2010, 2011) developed a first Discrete Fracture Network (DFN) considering hydraulically active parts and fracture sets and independently adapted the model for both wells using a particle tracking method. It was concluded that it is not possible to create a single homogeneous statistical fracture model that reproduces both wells simultaneously, as the main structure interferes with the hydraulic field between GPK3 and GPK4. Radilla et al. (2012) fitted a model to the experimental data, connecting the individual wells on three independent and isolated pathways with an equivalent stratified medium approach. All authors commonly conclude that a single-fracture approach is not suitable to sufficiently describe the hydraulic flow in the complex Soultz geothermal reservoir.

EGS are often simplified as theoretical/hypothetical fracture systems, connecting two wells along a line or one or more parallel plates (Bataillé et al., 2006; Fox et al., 2013; Vallier et al., 2019). It is known from the well-developed Soultz geothermal reservoir that this assumption does not adequately describe the structure of the heat exchanger system in an EGS (Genter et al., 2010). The understanding of the complex faults & fractures pattern and thus, on the tectonic history, preferential flow paths and hydrothermal circulations are crucial for the sustainable and safe design of a geothermal operation avoiding any artificially induced risks, like thermal breakthrough or induced seismicity (Zang et al., 2014). Therefore, the goal of the present study is a qualitative and quantitative evaluation of naturally and artificially induced fluid flow in a complex fractured geothermal reservoir to further investigate impacts of the considered limiting assumptions in the literature and better understand complex fluid circulation. Moreover, the knowledge gained allows the optimization of the design of future experiments and operation scenarios and the prediction of expected results (Kohl and Mégel, 2007).

Herein, we present an extensive numerical study including the large structural complexity of the Soultz fault and fracture network solving a transient fully-coupled Hydro-Solute (HS) transport simulation with the TIGER code. The three-dimensional flow field and tracer propagation in the Soultz geothermal reservoir are predicted and represent a major extension of an earlier approach by Held et al. (2014). The model includes the granitic basement as well as several hydraulically active faults and fractures as discrete surfaces and the open-hole sections of the wells as discrete line features. Long-term inter-well circulation tests are initially used to forward invert the hydraulic parameters of the fracture network while the hydraulic model is further recalibrated to reproduce the inter-wells tracer experiment (Sanjuan et al., 2006). The combination of the numerical approach with different kind of experimental data allows quantification and evaluation of the flow field inside the heat exchanger of the Soultz EGS and the identification of inter-well connections over the complex fracture network. The numerical approach allows a detailed characterization of the subsurface heat exchanger with the possibility to recognize feasible features for future expansion.

7.2 THE SOULTZ GEOTHERMAL RESERVOIR

The Soultz geothermal system is located in the French-side of the central URG, which is part of the European Cenozoic Rift System extending from southern France to the North Sea (Ziegler and Dèzes, 2005). The major tectonic feature of the Soultz reservoir is a horst structure uplifting the Soultz reservoir between Hermerswiller and Kutzenhausen fault, narrowing the Cenozoic and Mesozoic cover to a thickness of 1400 m (Aichholzer et al., 2016). The underlying crystalline basement is characterized as a low-permeable naturally fractured rock (Hooijkaas et al., 2006; Sausse and Genter, 2005) with an alteration-dependent rock matrix permeability ranging from $10^{-19}\,m^2$ to $10^{-20}\,m^2$ (Hettkamp et al., 1999). The existing fault- and fracture-system is a result of the tectonic history of the URG. The dominant fracture orientation ($N160 \pm 15°E$) is linked to the recent maximum horizontal stress orientation of $N170 \pm 10°E$ (Cornet et al., 2007; Evans et al., 1997). Other fracture sets are oriented with Rhenish ($N20 \pm 10°E$) and Hercynian ($N130 \pm 10°E$) orientation with a steep dip ($> 60°$) to the west (Dezayes et al., 2010). The mean aperture is varying between 0.1 mm and 250 mm (Dezayes et al., 2010). Fractures oriented parallel to the main stress field tend to remain open and thus contain increased permeability (Cornet et al., 2007), while those perpendicular or orthogonal to the main stress field have the tendency to be sealed.

As shown in Figure 7.1, the Soultz EGS can be divided into three sub-reservoirs (2000 m, 3500 m, and 5000 m) and utilized by four wells (GPK1 to GPK4) (Schill et al., 2017). The boreholes were drilled into the western flank of the Soultz horst structure. The GPK1 well targets the middle reservoir with a maximum depth of 3600 m while GPK2 to GPK4 were drilled over 5000 m depth to exploit the deeper crystalline reservoir (Genter et al., 2010). The lowest $500 - 700$ m section of each borehole is not equipped with a casing and left completely open against the rock. The remaining part is cased with leakages reported for GPK2 and GPK4 (Pfender et al., 2006). The leakage of the well GPK2 at the depth of 3880 m connects GPK2 to the major fractured and altered zone GPK3-FZ4770 and thereon to the well GPK3 (Sausse et al., 2010). Jung et al. (2010) concluded a fluid loss of more than 16 % in the leakage of GPK2 measured with the brine displacement method. The three deep wells are aligned NNW-SSE with a lateral distance of 650 m in a depth of 5000 m while the distance between GPK1 and GPK2 is 450 m.

Circulation and inter-well tracer experiments allow the prediction of forced fluid flow and the hydraulic quantification of the connection between the individual wells, while spatial information, e.g. on the flow paths within the reservoir, is not known (Ghergut et al., 2013). At the Soultz site, several experiments have been conducted with different well setups during the long-term research activities (Schill et al., 2017). A tracer experiment carried out in 1997 examined the connection of GPK1 and GPK2 (Aquilina et al., 1998), while a tracer experiment in 2005 further focused on the main hydraulic connections in the deeper reservoir between GPK2, GPK3, and GPK4. Sanjuan et al. (2006) concluded two connections between GPK3 and GPK2 through a hydraulic short-circuit and an additional pathway of elevated length, while a poor link between GPK3 and

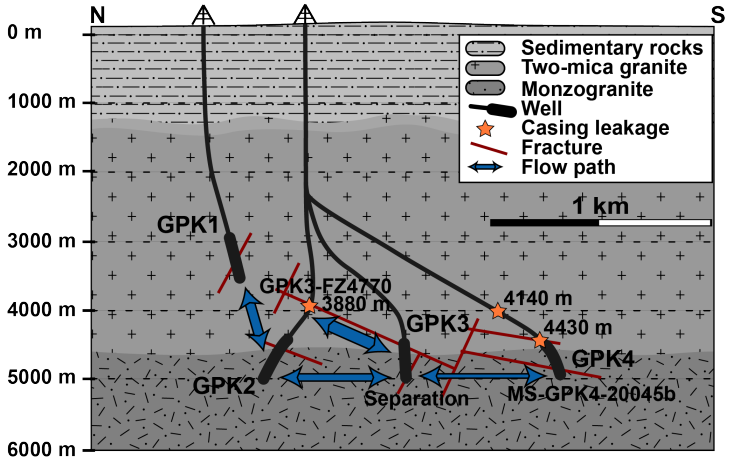

Figure 7.1: 2D-Subset of the geological setting of the Soultz geothermal reservoir including wells, open-hole sections, and the considered lithological units. The main fractures are shown as red lines; the expected hydraulic connections based on Sanjuan et al. (2006) and Aquilina et al. (2004) are shown in blue; orange stars indicate the reported casing leakages.

GPK4 was observed. Further inter-well tracer experiments have been conducted confirming the main findings of this experiment (Sanjuan et al., 2015).

7.3 NUMERICAL MODELING

The numerical simulations are carried out with a Finite-Element (FE) open-source application called TIGER (THC sImulator for GEoscience Research) (Gholami Korzani et al., 2020), which is based on MOOSE (Multiphysics Object-Oriented Simulation Environment) framework (Gaston et al., 2009). TIGER has been developed to tackle thermo-hydraulic-solute transport problems in geothermal reservoirs including lower-dimensional features for fractures and well paths.

7.3.1 *Governing equations*

The approach assumes a Representative Elementary Volume (REV) for the porous media where interaction between the coupled processes can occur. The hydraulic field is solved for the pore pressure by combining mass and momentum balances including Darcy's law (Bear and Cheng, 2010) as:

$$bS_m \frac{\delta P}{\delta t} + \nabla . b\boldsymbol{q} = Q \tag{7.1}$$

$$\boldsymbol{q} = \frac{\boldsymbol{k}}{\mu}(-\nabla P + \rho^l \boldsymbol{g}) \tag{7.2}$$

where P is the pore pressure; t is the time; S_m is the mixture specific storage of the liquid and solid phase; Q is the source term for injection and production; $\boldsymbol{k}$

is the permeability tensor; μ is the fluid dynamic viscosity; ρ^l is the fluid density; $\boldsymbol{g}$ is the gravitational acceleration vector; $\boldsymbol{q}$ is the fluid or Darcy velocity vector and b is the scale factor for considering fractures (aperture) and wells (area). Lower-dimensional fractures are treated as discrete 2D elements while open-hole sections are discretized as 1D elements, sharing nodes, faces, and lines with the 3D continuum.

The transport of solutes (e.g. tracers) is considered as spatial and temporal changes of concentration which are governed by an advection-diffusion-dispersion equation (Bear and Cheng, 2010).

$$b\frac{\phi\delta C}{\delta t} + b(-\nabla.\boldsymbol{D_m}\nabla C + \boldsymbol{q}\nabla.C) = Q \tag{7.3}$$

where C is the solute concentration; ϕ is the porosity; $\boldsymbol{D_m}$ is the sum of molecular diffusion and dispersion. The dispersion tensor is dependent on Darcy velocity and longitudinal and transversal dispersivity (Bear and Cheng, 2010), which generally describes the mixing around maximum concentration due to different mechanical effects (Bauget and Fourar, 2007).

7.3.2 *Numerical model*

A 3D-Discrete Fracture Matrix (DFM) model is used to ensure high accuracy in the geometrically complex reservoir by considering DFN and the surrounding matrix in the numerical analysis (Berre et al., 2019). The available information about the geological and tectonic settings, including well paths and open-hole sections, can be merged into a structural model of the Soultz geothermal reservoir. The used reservoir model, which is a subset of the structural model proposed by Sausse et al. (2010) and Place et al. (2011), is based on the 3D-model created by Held et al. (2014). However, the model is updated and extended in this study by introducing two additional fracture zones as 1) the WNW-ESE-oriented fracture 'Separation' between the wells GPK3 and GPK4, and 2) GPK1-FZ2856 fracture intersecting GPK1 in the middle reservoir. The Separation fracture was not drilled but suspected as an anomalous zone of either higher permeability or hydraulic barrier, separating the deeper reservoir into a northern and a southern part (Calò et al., 2016; Kohl et al., 2006; Sausse et al., 2010). The fracture GPK1-FZ2856, identified using Vertical Seismic Profiling (Sausse et al., 2010), is added to allow better adjustment of hydraulic parameters close to the GPK1 well. The model has an extension of 13(E-W) $\times$ 11 km (N-S) km with a vertical depth of 5 km (Figure 7.2), located between 1000 m and 6000 m below surface. The extension of the domain is chosen, to avoid boundary effects on the area of interest and to possibly consider the effects of the regional flow field. The minimum lateral distance between well and boundary is 4000 m.

Minor simplifications were made regarding the location, dipping and hydraulic appearance of the fracture network by representing fractures as discrete features. Out-of-plane mixing effects like surface roughness, fault gauge or internal mixing cannot be treated individually and are therefore summarized in the hydrodynamic dispersion (Bauget and Fourar, 2007). Tsang et al. (1988)

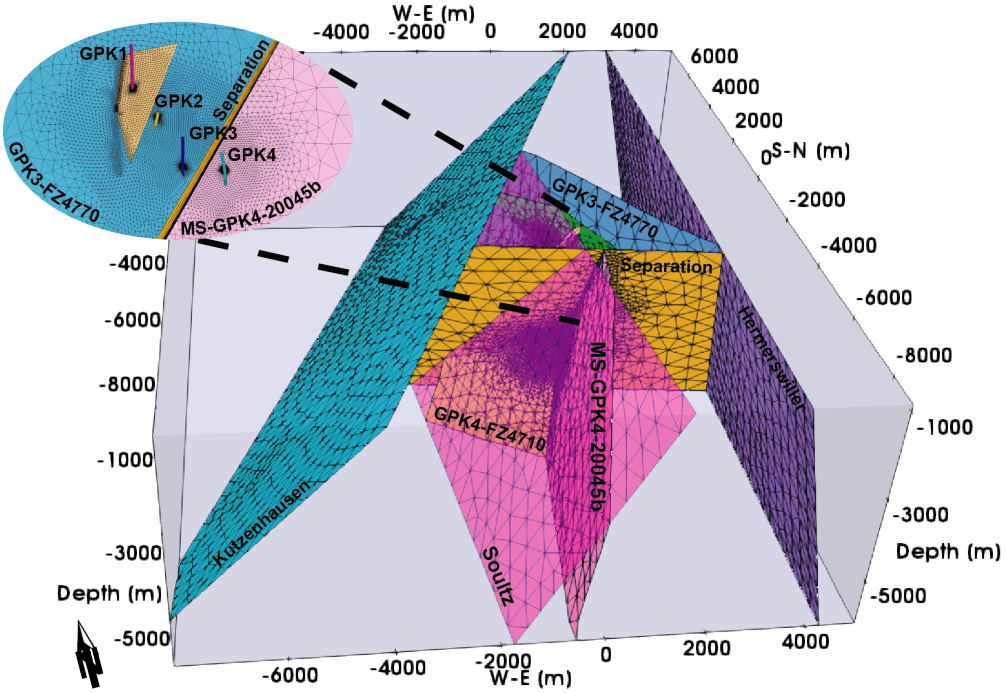

Figure 7.2: 13-fracture-model of the Soultz geothermal reservoir including wells (modified after Held et al., 2014). Grey shows the extension of the matrix. 10 out of 13 discrete faults and fractures are shown. The central area of the mesh along GPK3-FZ4770 and between GPK2, GPK3, and GPK4 is shown in detail.

concluded that it is suitable to use a statistically homogeneous system (e.g. for aperture, permeability) if the transport dimensions are significantly larger than the spacing between the channels belonging to a fracture and the transport distance is large enough to remain unaffected by local heterogeneities. The wells GPK1 to GPK4 are discretized over the entire open-hole section (and casing leakage) and connected with at least two fractures to the reservoir. The element size differs between 1.5 m (around and along the wells) and 500 m (close to the boundaries) with a typical element size around 40 m. As the fracture GPK3-FZ4770, establishing the main connection of GPK3 and GPK2 is inclined and not oriented parallel to the wells, the wells intersect the fracture in different reservoir levels resulting in the true distance of 840 m (compared to the often used 650 m derived from a pure horizontal distance). To consider the effects of hydraulic or chemical stimulation (Nami et al., 2008; Schill et al., 2017) and to minimize mesh dependency of the results, the main fracture GPK3-FZ4770 is subdivided and refined around GPK2 and GPK3. In total, the model contains 141 271 nodes which are connected by 714 453 elements including 3D matrix, 13 fractures, and 4 wells as shown in Figure 7.2.

The pore pressure in the whole reservoir is assumed to be hydrostatic (Stober and Bucher, 2007) by setting the top and bottom boundary conditions (BC) as Dirichlet BC and the model initial condition (IC) in accordance. Injection and extraction rates are applied as time-dependent mass-flux-function on top of each open-hole section. The matrix permeability is assumed to be orthotropic

Parameter	Value
Fluid density [$kg\,m^{-3}$]	1065
Fluid dyn. viscosity [$Pa\,s$]	2.3×10^{-4}
Fluid compressibility [Pa^{-1}]	2×10^{-9}
Matrix compressibility [Pa^{-1}]	5×10^{-13}
Fracture porosity [-]	1
Matrix porosity [-]	10^{-2}
Solute diffusion [$m^2\,s^{-1}$]	4×10^{-10}

Table 7.1: Constant model input parameters for the fluid and solid phases, the reservoir brine properties are in accordance with Kestin et al. (1981) representing a brine with 150 °C, 35 MPa and 1.5 $mol\,kg^{-1}$ salinity.

with higher permeability in N-S-direction to take the regional stress field of the URG and small-scale fractures into account (Cornet et al., 2007). A natural S-N-oriented graben-parallel background flux of $1\,m\,h^{-3}$ (Bächler et al., 2003; Sanjuan et al., 2006) is applied to the main faults and fractures as a function of the individual aperture.

The injected fluorescein tracer is assumed to be conservative in terms of reaction and sorption during transport as well as radioactive and thermal decays (Adams and Davis, 1991; Berkowitz, 2002). Solute diffusion, dispersion, and advection into the granitic basement are neglected (Bodin et al., 2003a), as the porosity of the matrix is significantly smaller than the ones of the DFN (Aquilina et al., 2004). The solute (re-)injection is applied as time-dependent Dirichlet BC inferred from concentration measurements at GPK3 wellhead. The parametrization of the matrix and fluid properties took into account the conditions in the reservoir (e.g. increased temperature and salinity, Table 7.1). For enhancing the accuracy, minimizing unwanted numerical diffusion and conservation of the sharp concentration front, a second-order semi-implicit time-integration method (Crank and Nicolson, 1996) and a Streamline Upwind method (Brooks and Hughes, 1982) are applied.

7.4 RESULTS

7.4.1 *Calibration of the hydraulic and solute processes*

The transmissivities of the Soultz fracture network are calibrated against two circulation tests conducted in 2009 (Schindler, 2009) and 2011 (Genter et al., 2011). Flow rate changes at wellheads and their effects on the reservoir pore pressure were used to quantify the transmissivities of the faults and fractures. Flow velocity logs from each borehole were used to assign the measured portion of flux to the individual fractures since the matrix tends to have significantly lower permeability. The calibration is necessary because two further fractures, compared to Held et al. (2014), affect the pressure field and the capability of

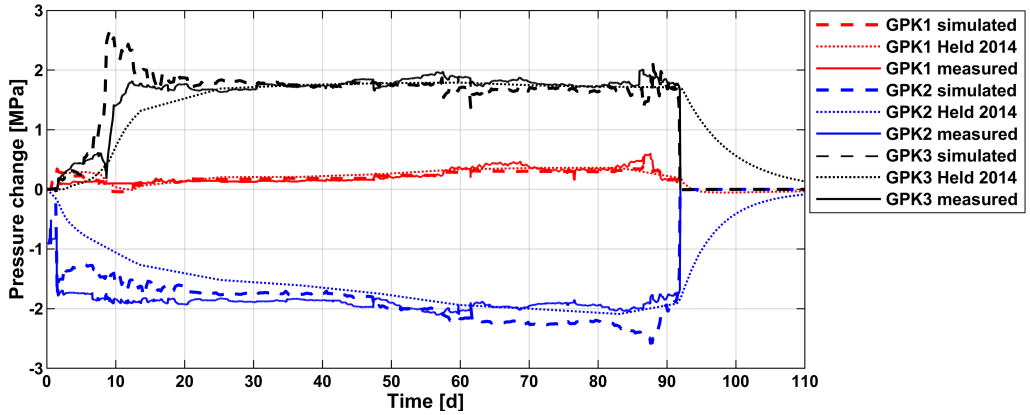

Figure 7.3: Pressure changes in comparison with the measured data and results of Held et al. (2014). Positive pressure changes represent fluid injection.

TIGER in applying time-dependent BCs enabling more accurate modeling of the reservoir.

A circulation test, with average flowrates between 9 and 20 $\mathrm{L\,s^{-1}}$, conducted in early 2011 (Genter et al., 2011) allowed the calibration of the fractures connected to three wells of GPK1, GPK2, and GPK3 through production in GPK2 and reinjection in GPK1 and GPK3. Figure 7.3 shows the pore pressure changes at GPK1 to GPK3 after the calibration of the fractures' transmissivity. For GPK1, no flow rate data was recorded from 8th to 10th day of the experiment leading to no flow in the simulation. However, the pressure response almost fitted the measured data. The lower pressure increase in GPK1, compared to GPK3, indicates a good connection of the borehole to high permeable zones. For GPK2, the simulated data slightly underestimates the pressure response in the first 50 days, while it overestimates later. A casing leakage was reported after day 47 (Genter et al., 2011), affecting the experimental results. This leakage caused the fluid already pumped in the pipe to flow back into the reservoir and led to lower measured pressure change for the measured flow rates. That leakage was not incorporated in this study as it only affects the internal system of GPK2 well.

The measurements of GPK3 show high scattering up to 20 days, which was caused by strongly varying flow rates at the start of the experiment. After 20 days, the flow rate was kept constant, leading to a steady pressure change until the end of the experiment. The obtained pressure changes for GPK3 did not well match the measured data between day 5 and 15. The missing match could be the result of several factors like borehole or skin effects, (re-)opening of small-scale fractures, changes in the flow regime and leakages in the tubing. Since the proposed model focuses on long-term evaluation, the calibration was done by fitting the mean steady section of the experimental data. It is worthwhile noting that the injection wells (GPK1 and GPK3) have almost the same average flow rates (approx. 9 $\mathrm{L\,s^{-1}}$) and at the same time have significantly different pressure responses. The immediate pressure decline after the pump shutdown shows a small storage effect along the different fractures and the granitic matrix.

A single-well circulation test in 2009 (Schindler, 2009) was used to calibrate the transmissivities of the fractures in the southeastern part of the reservoir

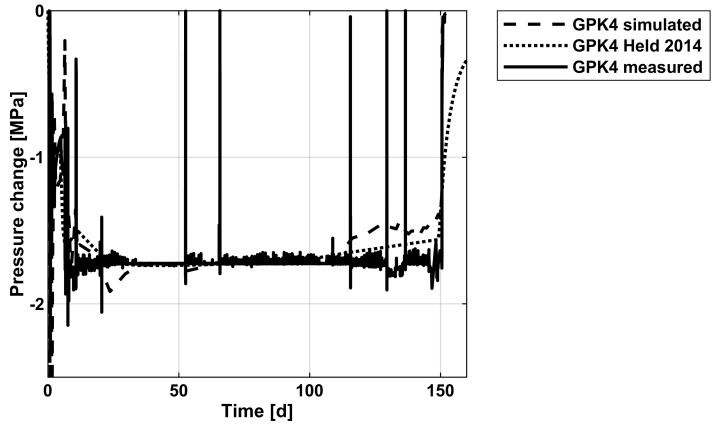

Figure 7.4: Pressure changes compared with the measured data and results of Held et al. (2014) for GPK4. Missing experimental data leads to zero values.

connected to GPK4 (Figure 7.4). Strongly varying flow rates up to the 10th day were only partially considered because their influence on the long-term reservoir behavior is negligible. Discrepancies between simulated and measured data occurring after 110 days are probably due to disturbances in the experimental sequence. Therefore, the steady pressure change between day 30 and 110 was used for the calibration of the hydraulic features.

The faults and fractures were calibrated for their transmissivities and the granitic matrix for the permeability and hydraulic diffusivity (Table 7.2). In comparison to Held et al. (2014), the calibrated data differs slightly. It is worthwhile noting that the fractures close to the wells affect the calibration results decisively. Therefore, the calibrated transmissivities have a high accuracy in the vicinity of the wells, but give only a rough estimate for the hydraulic properties of remote faults and fractures.

7.4.2 *Flow field*

The findings of the circulation experiments can be coupled to multi-well tracer experiments for quantifying the inter-well connection and flow field of the Soultz geothermal reservoir. A 145-day tracer test was carried out between July and December 2005 in the wells GPK2 to GPK4 (Sanjuan et al., 2006). During the experiment, fluorescein tracer was injected in GPK3 and extracted from GPK2 and GPK4. The fluid, extracted with average flow rates of $11.9\,\mathrm{L\,s^{-1}}$ (GPK2) and $3.1\,\mathrm{L\,s^{-1}}$ (GPK4), was reinjected in GPK3 with $15\,\mathrm{L\,s^{-1}}$. The fluorescein concentration during injection was $146\,\mathrm{mg\,L^{-1}}$ over 24 h. Before the first injection, 8 days of circulation provided a stationary flow field. The results of the experiment and best-fit modeling for the wells GPK2 and GPK4 are shown in Figure 7.5 and Figure 7.7. The peak velocities of the different pathways were fitted under the assumption of the obtained transmissivities in the previous section by adapting the permeability to the expected and measured travel time and fluid velocities along the affected fractures. The mixing around the breakthrough maximum was achieved by adjusting the longitudinal and transversal dispersivity and the

Name	Transm. [$m^2\,s^{-1}$]			Perm. [m^2]
GPK3-FZ4770	4.80×10^{-5}	Matrix	x	1.34×10^{-16}
GPK1-FZ2856	5.00×10^{-5}		y	3.30×10^{-16}
GPK1-FZ2120	3.80×10^{-4}		z	1.65×10^{-16}
GPK3-FZ5020	1.68×10^{-5}			
GPK4-FZ4710	3.80×10^{-5}			
Soultz fault	6.80×10^{-5}			
Kutzenhausen fault	6.80×10^{-4}			
MS-GPK2-2000a	5.10×10^{-5}			
MS-GPK3-2003a	3.90×10^{-4}			
MS-GPK4-20045b	3.20×10^{-5}			
Hermerswiller fault	6.80×10^{-5}			
PS3-Int (VSP)	6.40×10^{-4}			
Separation	6.80×10^{-5}			
GPK3-FZ4770-GPK2	5.65×10^{-5}			
GPK3-FZ4770-GPK3	2.95×10^{-5}			

Table 7.2: Calibrated transmissivities of the faults and fracture network and the permeability of the granitic matrix.

variation of the aperture. In addition, the 95 % confidence interval as the result of the standard error of the mean modeled solute concentration is presented.

Figure 7.5 shows the modeled and observed results of GPK2 for the tracer breakthrough curve (BTC). The maximum concentration (730 $\mu g\,L^{-1}$), giving a peak velocity of 2.6 $m\,h^{-1}$, was observed after 13 days. A strong tailing is noticeable until the end of the experiment, which could be the result of 1)

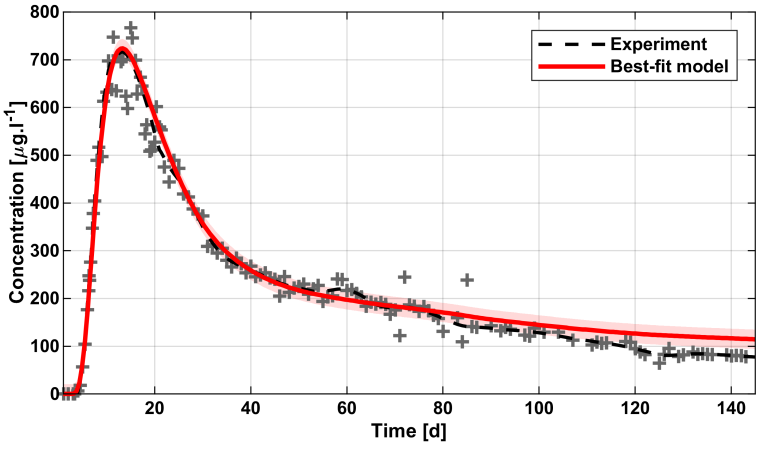

Figure 7.5: Simulated and measured fluorescein concentration at well GPK2; The grey crosses are the experimental data, and the black line shows their mean value. The red line shows the best-fit model with a 95 % confidence interval as the red shadow.

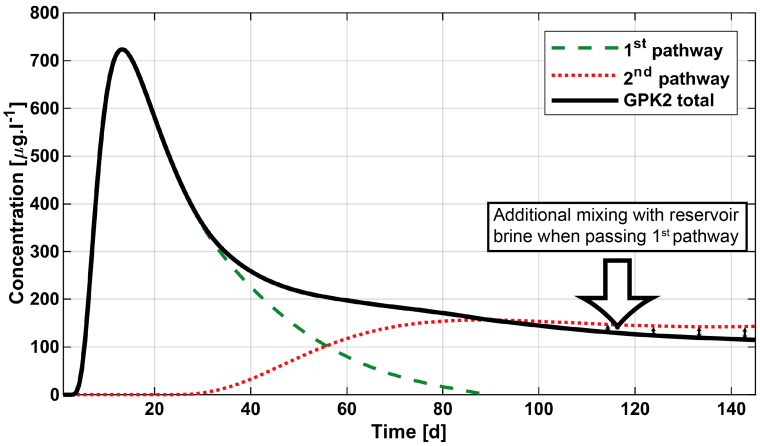

Figure 7.6: Simulated tracer concentration at the GPK2 wellhead by showing the contributions of the individual pathways.

diffusive exchange with matrix, 2) dispersive effects in the fracture channeling and/or 3) the interconnection of the wells by different fracture sets (Becker and Shapiro, 2000). As shown in Figure 7.8 the tailing could be related to the latter option. It is possible to identify and quantify two to three different hydraulic pathways connecting GPK3 and GPK2 (Figure 7.6). The main solute influx in GPK2 was identified to occur along the fracture GPK3-FZ4770, connecting the open-hole section of GPK3 with the casing leakage of GPK2. The entire amount of tracer along this pathway was swept after 90 days of circulation. The second pathway along GPK3-FZ4770 and MS-GPK2-2000a was noticed after 26 days and has a maximum concentration of 161 µg L^{-1} after 90 days with a peak velocity of 0.5 m h^{-1}. The third pathway, along GPK3-FZ5020 and MS-GPK2-2000a, shows a strong dilution with reservoir fluids, which is why no peak concentration can be detected in the simulation. The lower total measured concentration compared to the second pathway tracer concentration after 90 days (Figure 7.6) can be explained by additional mixing along the well trajectory of GPK2. The mixing took place when the higher concentrated fluid, entering the open hole section of GPK2, passed the casing leakage on its way upwards and was mixed with the less concentrated fluid of the upper pathway. These pathways were also confirmed in further experiments conducted in 2010 and 2013 along this pathway (Sanjuan et al., 2015).

The result of the simulation at GPK4 in comparison to the experimental data is shown in Figure 7.7. The first arrival occurred 23 days after injection while the maximum concentration (31 µg L^{-1}) was measured at the end of the experiment. A peak in the concentration, similar to the recorded one for GPK2, cannot be observed within the experimental period. The BTC shows typical behavior with clear mixing effects, such as strong dilution and no clear maximum. The reported scattered measured data could not be reproduced in the simulation. Predictions about the mean transfer time and maximum concentration are therefore subject to a high degree of uncertainty. Assuming a continuous circulation and constant flow rates, the peak concentration of 48 µg L^{-1} was observed after 1.5 years followed by a decline to 23 µg L^{-1} at the end of the long-term forecast (5 years)

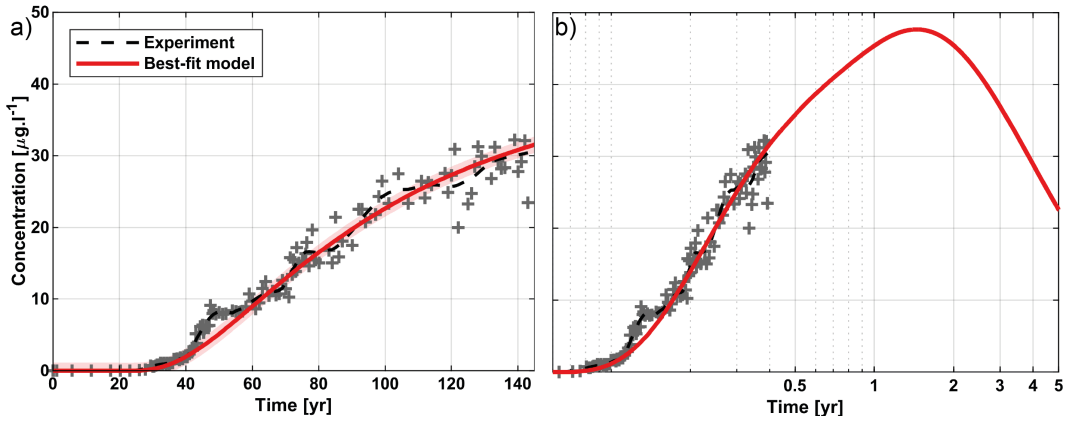

Figure 7.7: Simulated and measured dimensionless fluorescein concentration at GPK4; a) over the experimental duration; b) long-term forecast for 5 years. The grey crosses are the experimental data, and the black line shows their mean value. The red line is the result of the best-fit model with a 95 % confidence interval as the red shadow.

(Figure 7.7b). The relatively late arrival time at GPK4 compared to GPK2 indicates the low fluid velocity (0.06 m h^{-1}) of this pathway. Combined with the low tracer concentration and widely spread peak, a poor hydraulic connection between both boreholes is clear probably due to the Separation fracture. The fracture is oriented in WNW-ESE-direction and thus acts as an anomalous zone, which hydraulically unlinks the two parts of the reservoir from each other by creating a preferential pathway and drainage along itself. Figure 7.8 shows the dimensionless solute concentration on the affected faults and fractures at several time steps.

The proposed different hydraulic pathways can be identified as areas with an increased solute concentration, which allow the movement of the solute between the injection and extraction wells. In addition to the hydraulic characterization of the DFN, effects of other factors, including tracer reinjection and background flux, which are of great importance for the (long-term) evaluation of the fracture network, were studied. The reinjection of the tracer-enriched produced fluid in GPK3 affected the evolution of long-term concentrations. After the arrival of the main peak, the reinjection of enriched fluids leads to elevated tracer concentrations along GPK3-FZ4770. At the end of the experiment period, Figure 7.9a illustrates a 20 % reduction in the tracer concentration at GPK2 if the tracer reinjection was neglected. This factor influenced the concentration obtained for GPK4 less prominently than for GPK2 but a 6 % reduction is still documented in Figure 7.9b.

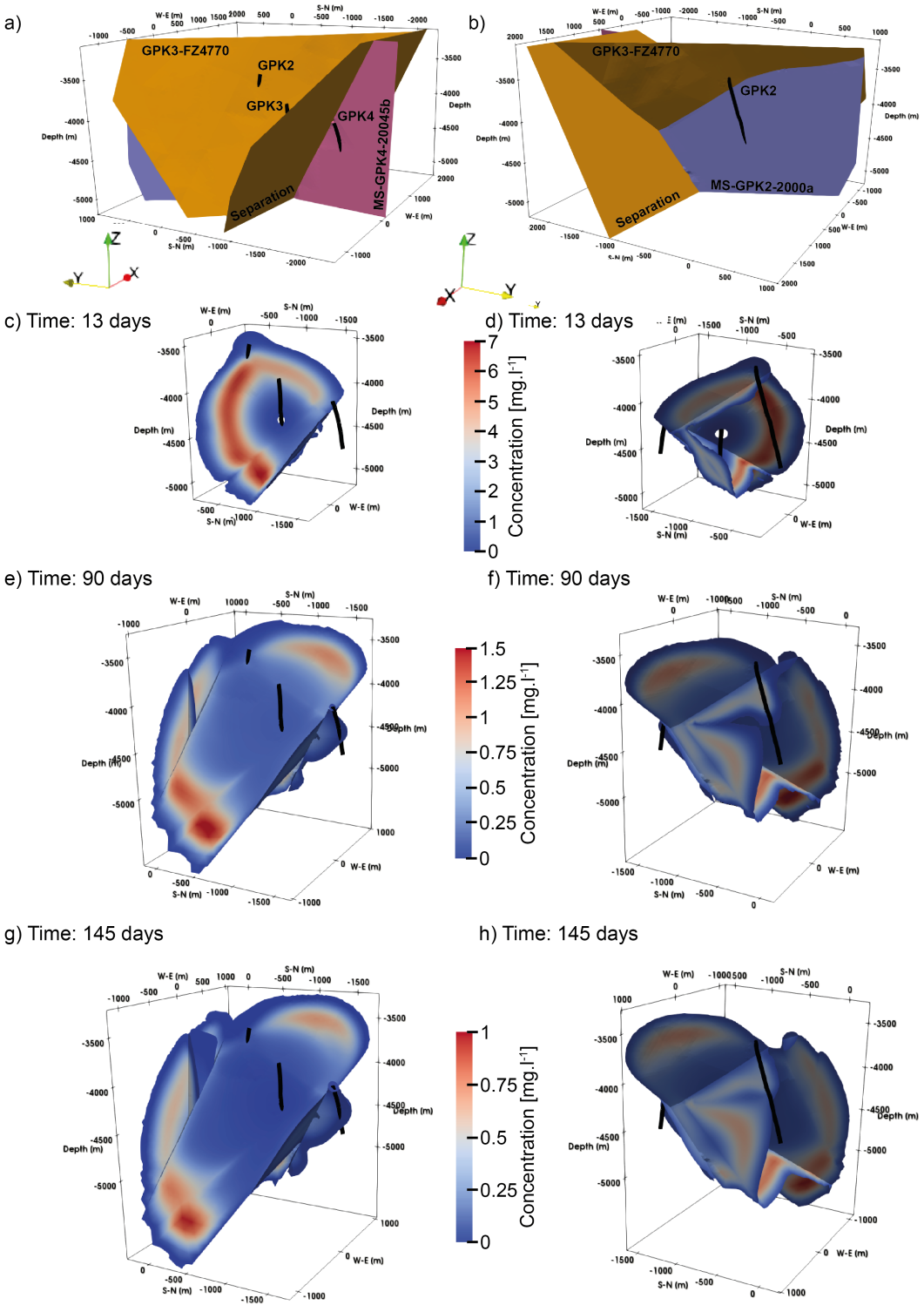

Figure 7.8: Comparison of tracer concentrations in different faults and fractures. Left side) View from southwest, right side) View from the northeast. a-b) the mainly affected fractures, c-d) the tracer concentration at GPK2 reaches the maximum, e-f) the second pathway reaches the maximum and g-h) the end day of the experiment.

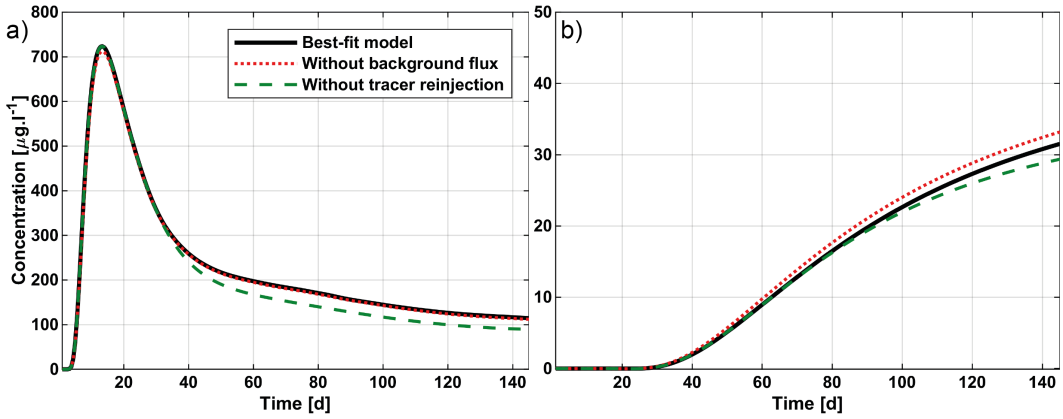

Figure 7.9: Sensitivity of concentration due to background flux and tracer reinjection of the wells GPK2 (a) and GPK4 (b). Note the different axis scale.

Another factor is the effect of the natural background flux along the main faults and fractures due to the natural convective system of the Soultz reservoir. A minimum velocity of 11 cm yr^{-1} reported by Vallier et al. (2019) and fluxes for faults and fractures were accordingly calculated. However, fluid velocity within fractures and faults generated by injection and production scenarios was dramatically higher than the induced velocity by the background convective flux. Consequently, the influence of this natural flux on the produced tracer concentration at GPK2 is negligible (Figure 7.9a), and ignoring this factor causes an increase of about 2 % in the concentration for GPK2. For GPK4, the background flow is opposing the available hydraulic gradient and thus lowers the recorded tracer concentrations by around 5 % at the end of the tracer experiment (Figure 7.9b).

7.5 DISCUSSION

Our results, therefore, confirm the existence of different pathways, connecting the wells of the Soultz geothermal reservoir along different faults and fractures. The wells GPK3 and GPK2 show a good and fast hydraulic connection, which is realized by three different pathways with different travel and residence times. Low measurable tracer concentrations indicate a poor hydraulic connection between GPK3 and GPK4. The convective background flux, as proposed by Sanjuan et al. (2006), has a minor effect on the resulting concentrations, as the forced fluid velocities exceed the natural convective velocities by several orders of magnitude.

As shown in Figure 7.9, re-circulated brine, containing tracers, can lead to a significant long-term increase in the overall concentration and it should be considered in momentum analysis of tracer recovery, swept volume and heat exchange area (Shook, 2005). The cumulative tracer recovery ratio, R_{fluo}, is the sum of the recovered solutes of each pathway (Figure 7.6). It can be calculated from the time-concentration plot by multiplying the concentration data with the production flow rate and the inverse of the totally injected tracer-mass. As calculated in Table 7.3, the total tracer recovery during the experimental period

is 25.0 %, which GPK2 and GPK4 contributed 24.6 % and 0.4 %, respectively. The total recovery of the model presented is well comparable with the experimental data and the extrapolated results from it (23.5 %, Sanjuan et al., 2006) and 25.3 % (Sanjuan et al., 2015) although the individual contributions are not exactly matched. The stronger influence of the second pathway for GPK2 in the numerical simulation is partly caused by the slight overestimation after 78 days as demonstrated in Figure 7.6.

The overestimation of the long-term values can have various causes. One possible reason are unknown fractures, which are hydraulically connected to the second pathway. Such fractures could not be considered in the model, because they were not drilled and therefore neither their geometric appearance nor their hydraulic influence on the reservoir are known (Mégel et al., 2005). Another explanation of the slight differences can be the connection of the two fractures since its internal structure is unknown, but complex flow pattern and thus mixing processes can occur here (Berkowitz et al., 1994). The neglected thermal decay of the fluorescein can also lead to slight deviations in the results, especially over a longer period of time (Adams and Davis, 1991). On the other hand, considering tracer diffusion into the matrix can increase the long-term concentration results, while the peak is lowered (Ghergut et al., 2018). This simplification is nevertheless permissible since there is no evidence of matrix diffusion (Radilla et al., 2012) and the system is strongly convective, with the time scale of the transport process being significantly shorter than that of the diffusion into the matrix (Bodin et al., 2003a).

The swept volume can be calculated from the recovery rate. The swept volume, V_{swept}, is a measure of the pore volume swept by tracer during an experiment as (Levenspiel, 1972)

$$V_{swept} = q_{inj} \tau R_{fluo} \tag{7.4}$$

where τ is the mean residence time, corrected for the tracer recycling and q_{inj} is the injection rate. Key assumptions for these calculations are a steady flow field on the affected fractures and the usage of a conservative tracer without mass losses. The swept or pore volume for the connection of GPK3 and GPK2 is 4000 m^3 for the first pathway and 10 300 m^3 for the second pathway. The swept volume for the first pathway and Sanjuan et al. (2006) are a perfect match, while the value of the second pathway is rising by around 60 %, which is due to the higher recovery rate in simulations. If a mean transfer time for GPK4 is calculated at the end of the experiment (145 days), the total swept volume is 133 m^3, which corresponds to Sanjuan et al. (2006). However, it is significantly smaller compared to the main pathways between GPK3 and GPK2.

The results confirm the existence of a fractured zone between the wells GPK3 and GPK4. After calibration of the numerical model using hydraulic and tracer tests, the Separation fracture, which is oriented WNW-ESE, could be assigned as a hydraulic conduit between the NNW-SSE striking fractures. The fracture is connecting the northern reservoir with the main fault system and creating a preferential fluid pathway. Since the fractures intersecting GPK4 (MS-GPK4-20045b and GPK4-FZ4710) have a higher resistance to fluid flow than the Separation

	R_{fluo} [%]		V_{swept} [m^3]	
Wells	This study	Sanjuan 2006	This study	Sanjuan 2006
GPK2 – 1st path	14.5	15.6	4000	3900
GPK2 – 2nd path	10.1	7.9	10300	6500
GPK4	0.4	1.8	133	120
Total	25.0	25.3	14533	10520

Table 7.3: Summary of the recovery ratio and swept pore volume of the inter-well flow between GPK3 - GPK2 and GPK3 - GPK4 as resulting from recovered solute concentrations in comparison to Sanjuan et al. (2006)

fracture, the tracer is mainly transported and mixed along this fracture and only little amount passes to the southern reservoir and GPK4. The results are in agreement with the microseismic inversion of Kohl et al. (2006), which indicated a seismically inactive E-W-striking plane that could be either highly permeable or totally sealed. Calò et al. (2016) concluded a seismic anomalous zone between the two wells from Vertical Seismic Profiling as well. Barton et al. (1995) observed that fractures oriented perpendicular to the maximum horizontal stress have a higher probability to be sealed. Here, the fracture possesses a high hydraulic conductivity, even as the orientation is unfavorable in terms of dilation with respect to the regional stress field. Localized stress perturbations and a transition in the stress regime (from normal-faulting to strike-slip) are known for the deepest parts of the Soultz reservoir (Cuenot et al., 2006; Dorbath et al., 2010). Comparable observations could also be made for the nearby Bruchsal geothermal power plant. Several antithetic fractures have been detected, which are misaligned with the recent stress field and are a result of the complex tectonic history of the URG (Meixner, 2016). Those misoriented fault zones can, as indicated in this study, have an impact on the local flow field.

In the northern part of the reservoir, the fracture GPK3-FZ4770 creates the shortest pathway between the wells GPK3 and GPK2, with the main contribution to the inter-well flow and an average fluid velocity of $2.6\,\mathrm{m\,h^{-1}}$. As the breakthrough curve is completely captured within the experimental time, the minimum heat exchange area for this pathway can be calculated. The minimal heat exchange surface area is the area of the fracture surfaces swept by fluid traveling from the injection to the production well assuming a parallel plate model with the known pore volume and aperture (Robinson and Tester, 1984). The area along the GPK3-FZ4770, which was analytically calculated from the pore volume swept ($1.1 \times 10^6\,\mathrm{m^2}$), is half of the area ($2.1 \times 10^6\,\mathrm{m^2}$) determined by the analysis of the streamlines between the wells in the simulation results (Figure 7.10). In reality, the heat exchange area tends to be even higher due to the complex internal structure of fractures, which is simplified in the model. Fractures in the area of Soultz are typically described as zones of highly clustered shear fractures with varying aperture and length. A core zone is surrounded by a damage zone and hydrothermally altered granite (Dezayes et al., 2010). Shook (2003) developed a concept for quantifying the relationship between the flow capacity of the set of fracture channels and its storage capacity. According to this

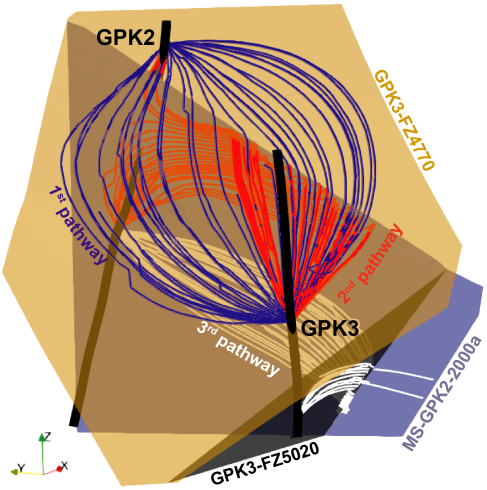

Figure 7.10: The main fractures and flow paths connecting the wells GPK3 and GPK2. The first pathway connects both wells along GPK3-FZ4770, the second pathway along GPK3-FZ4770 and MS-GPK2-2000a and the third pathway along GPK3-FZ5020 and MS-GPK2-2000a. The streamlines are displayed for visualizing the fracture flow.

approach, the fracture GPK3-FZ4770 can be described as a set of clustered channels with non-uniform internal structure in which half of the fluid produced in the experiments passes through 27 % of the pore volume. Therefore, the heat surface area, where the exchange between the fracture and the matrix occurs, tends to be larger than calculated and simulated with the parallel plate approach. The flow field along the fracture is asymmetric. As already shown in Figure 7.8, most of the fluids recovered in GPK2 originated from a relatively small area between the two boreholes. However, a great amount of the injected solute remained in deeper sections of the reservoir and the fracture GPK3-FZ4770 without ever entering the influence region of GPK2. Detailed quantification of the minimal heat exchange area for the second and third pathways, as shown in Figure 7.8 is not possible as the flow and the inter-well connection occur at a set of fractures with different flow velocities and residence times, and time-concentration plot (Figure 7.6) shows ongoing recovery beyond the end of the experiment. The same issues also apply to the connection between GPK3 and GPK4.

The new results of the deep connection of the GPK2, GPK3 and GPK4 wells allow the reassessment of the performance of the Soultz-sous-Forêts heat exchanger system. The recalibration of the hydraulic model points to rapid fluid pathways in the central-northern part of the reservoir (between GPK1 and GPK2) increasing the risk of a (thermal) breakthrough. In contrast, for the operating scheme used in the tracer experiment, short circuits are rather unlikely due to the connection to the large-scale circulation system. The same applies to the current economic operation, where reservoir brine is produced from GPK2 and reinjected into GPK3 and GPK4 wells (Mouchot et al., 2018). Moreover, it could be shown that the northernmost part of the deep reservoir (north of GPK2), as well as the connection of the separation fracture to the regional fault system, has enlarged hydraulic conductivity and thus could potentially be the target

for future research and exploration. The hydraulic model presented here can be used as a basis for the design and prediction of future experiments.

7.6 CONCLUSION

In the past, many attempts have been made to describe the flow field in the Soultz geothermal reservoir. Mostly, the individual interconnections of the wells were considered separately, while a holistic and more general description of the reservoir pathways often failed. In this paper, the developed and presented concept allows the simultaneous matching of the tracer's breakthrough curves on both production wells and the qualitative and quantitative identification of the different hydraulic interconnections along the fault and fracture network based on the structural model of the Soultz reservoir.

The Soultz EGS can be described as a fractured reservoir connecting different wells along flow channels generated by the main hydraulic pathways. The hydraulic connection of GPK3 and GPK2 was established along highly transmissive pathways with two fluorescein peak times of 13 and 90 days. The main direct pathway is occurring along the fracture GPK3-FZ4770, which accounts for 14.5 % of the tracer contribution. The cumulative tracer recovery of the different pathways is 25 % while the total swept volume is 14 533 m^3. The minimal heat exchanger surface on the main pathway is 2.1×10^6 m^2. The value is twice as large as the expected value from the analytical evaluation of the experiment. In contrast, the connection between GPK3 and GPK4 has no directly identifiable fluid pathway. The forecast modeling predicted a peak arrival after 1.5 years of continuous injection with the maximum tracer concentration which is 10 times lower than for GPK2. Only a small amount of tracer is recovered from the well GPK4 (0.4 %), and the swept pore volume is approximately two orders of magnitude smaller (133 m^3) than the direct and well-established connection of GPK2. The impeded connection between GPK3 and GPK4 is presumably related to a WNW-ESE-oriented fractured zone, establishing a preferential fluid pathway, connecting the northern reservoir with the local fault network, while the southern reservoir is only connected by minor transmissive fractures to this conductive zone. According to the new hydraulic model, further exploration and experimental research should focus on the connection of the Soultz geothermal reservoir to the regional fault network.

ACKNOWLEDGMENTS

We thank the anonymous reviewers for their constructive criticisms that helped to improve the quality of the manuscript. The authors acknowledge the financial support by the Federal Ministry for Economic Affairs and Energy of Germany in the project GeoFaces (No. 0324025C) and the Helmholtz portfolio project 'Geoenergy'. The support from the program 'Renewable Energies', under the topic 'Geothermal Energy Systems', is gratefully acknowledged. We also thank the EnBW Energie Baden-Württemberg AG for supporting geothermal research at KIT.

8

THERMO-HYDRAULIC MODELING OF AN ENHANCED GEOTHERMAL SYSTEM IN THE UPPER RHINE GRABEN USING MOOSE / TIGER

This chapter is published in Proceedings World Geothermal Congress 2020+1.

ABSTRACT

The research project GeoFaces aims to analyze the thermo-hydro-mechanic properties of possible geothermal reservoirs in the Upper Rhine Graben (URG) in SW-Germany / E-France. The scope is the quantification of the fluid circulation along or through faults and fractures under recent geological conditions. This paper concentrates on the joint analysis of different scientific datasets to predict the physical behavior of the Soultz Enhanced geothermal reservoir in terms of thermal conduction and fluid flow. Different data, including temperature, hydraulic and seismic measurements, were evaluated and used as input and calibration parameters and for the definition of the boundary conditions in a numerical fully coupled FE-13-fracture-modeling of the Soultz reservoir with the TIGER application (Gholami Korzani et al., 2020). On the basis of the models created by Sausse et al. (2010) and Held et al. (2014), new simulations were conducted to evaluate and calibrate the long-term behavior of the reservoir with regard to hydraulic and thermal sustainability. This analysis allows the prediction modeling of the reservoir temperatures under the new economic power plant design of Soultz-sous-Forêts as well as the sensitivity to changes in the production- and injection-rates and –temperatures.

8.1 INTRODUCTION

The Upper Rhine Graben (URG) is one of the most promising locations for geothermal energy utilization in central Europe with elevated thermal gradients up to $100\,\mathrm{K\,km^{-1}}$ and preferable hydraulic conditions (Pribnow and Schellschmidt, 2000). Power plant projects targeting either the deep crystalline basement as Enhanced Geothermal System (EGS) or the hydrothermal mesozoic sedimentary cover (Genter et al., 2016). EGS are designed to use and enhance the natural permeability of fault and fractures by hydraulic or chemical stimulation (Schindler et al., 2010). The most prominent European EGS is located at Soultz-sous-Forêts (Garnish, 2002), targeting a 5000 m deep fractured reservoir (Genter et al., 2010). Various kinds of experiments were conducted, creating a huge scien-

tific database and allowing the study of hydraulic and thermal processes in the fractured geothermal reservoirs in general (Genter et al., 2010; Sausse et al., 2010). Experiments, like circulation, tracer and flow-meter tests, allow the quantitative description of the fluid flow through the fractured reservoir rock, but give only punctual data at the wellheads, spatial and coupled information of the reservoir is quite often missing. The combination of structural and numerical models can close this existing gap and help to investigate the hydrothermal processes that take place in an EGS (O'Sullivan et al., 2001). In numerical modeling, EGS are very often simplified to a parallel-plate approach, which is not sufficient for the Soultz reservoir. Understanding and quantifying the fault and fracture network and thus the natural flow paths is crucial for the sustainable utilization of a geothermal power plant. Therefore, an updated numerical model of Held et al. (2014) is presented, considering the quantitative flow along the Soultz fracture network inferred from circulation tests, tracer experiments and the new power plant design for commercial usage of the facility (Mouchot et al., 2018). The findings are used to forecast the thermo-hydraulic long-term behavior of the heat exchanger system in terms of thermal breakthrough and cooling area. Furthermore, the sensitivity of the entire EGS design to different uncertainties, e.g. a further increase of the flow rates or different reinjection temperatures, is investigated using fully-coupled numerical simulations.

8.2 NUMERICAL MODELING

The Finite-Element(FE) open-source application TIGER (THC sImulator for GEoscience Research) (Gholami Korzani et al., 2020) was used for the numerical study. The code is based on the MOOSE framework (Gaston et al., 2009) and designed to solve thermo-hydraulic-solute transport problems in geothermal reservoirs in a fully coupled manner. It offers the opportunity to treat features like fractures and well paths in a discrete lower-dimensional way.

8.2.1 *Governing equations*

The hydraulic field is solved by combining the mass and momentum balances (Bear and Cheng, 2010) for the matrix as well as the lower-dimensional elements as:

$$bS_m \frac{\delta P}{\delta t} + \nabla . b\boldsymbol{q} = Q \tag{8.1}$$

$$\boldsymbol{q} = \frac{\boldsymbol{k}}{\mu}(-\nabla P + \rho^l \boldsymbol{g}) \tag{8.2}$$

where P is the pore pressure; t is the time; S_m is the mixture specific storage; Q is a source term for mass changes; $\boldsymbol{k}$ is the permeability tensor; μ is the fluid dynamic viscosity; ρ^l is the fluid density; $\boldsymbol{g}$ is the gravitational acceleration vector;

$\boldsymbol{q}$ is the fluid or Darcy velocity vector and b is the scale factor for considering fractures (aperture) and wells (diameter).

Heat transport is considered with an advection-diffusion equation considering Fourier's law:

$$b\rho c_p \frac{\delta T}{\delta t} + b(-\boldsymbol{\lambda}\nabla.\nabla T + \rho^l c_p^l \boldsymbol{q}\nabla.\boldsymbol{T}) = Q \tag{8.3}$$

where ρc_p and $\boldsymbol{\lambda}$ is the heat capacity and thermal conductivity of mixture, respectively. $\rho^l c_p^l$ is the heat capacity of the fluid.

8.2.2 *Numerical model*

The numerical model is based on a 3D-discrete fracture matrix model (DFM) incorporating the hydraulically active faults and fractures as a discrete fracture network (DFN) as well as the granitic basement as matrix. The open-hole-sections of the Soultz wells (GPK1 to GPK4) are included as line elements. The available information of the local reservoir setting is merged into a structural model of the Soultz EGS. The FE-model is based on the structural model of Sausse et al. (2010) and the numerical model of Held et al. (2014). For a better hydraulic adjustment, the numerical model is updated with two additional fractures, intersecting GPK1 (GPK1-FZ2856) and between GPK3 and GPK4 wells. The latter fracture is called 'Separation' and not drilled but suspected from seismic measurements (Kohl et al., 2006).

The mesh for the numerical study is shown in Figure 8.1 and extends 13(E-W) × 11(N-S) × 5 km (vertical depth) and is located between 1000 m and 6000 m below surface. The model contains 141 271 nodes, which are connected by 714 453 elements. It contains 13 hydraulically active faults and fractures as lower-dimensional elements neglecting out-of-plane flow. A homogeneous equivalent aperture is used to describe pressure and temperature changes along the fractures. Refinement is applied around and along the four well paths as well as on the main fractures and fracture-well-intersections. The element size differs between 1.5 m and 500 m. The lateral distance between the main wells GPK2, GPK3 and GPK4 is 650 m, while the direct connection along GPK3-FZ4770 results in a true distance of 840 m between GPK2 and GPK3.

The boundary conditions (BCs) for the different models are kept constant. Hydrostatic pore pressure is applied on the upper and lower boundary as Dirichlet BC and as initial condition (IC). The lateral boundaries are constraint as no flow Neumann BC. Injection and extraction are considered as mass-flux-function on the top of the open-hole sections. An orthotropic matrix permeability, with higher values in N-S-direction, considers the effects of small-scale fractures and the recent stress field on the hydraulic conductivity (Cornet et al., 2007). A natural graben-parallel background flux of 1 $m^3\,h^{-1}$ (Bächler et al., 2003) is applied to the main hydraulic features. The transmissivity of the different fractures was calibrated in Held et al. (2014) with two circulation experiments. Since two fractures were added, the hydraulic properties of the DFN had to be recalibrated, by the usage of the same circulation experiment data and additionally, an inter-well

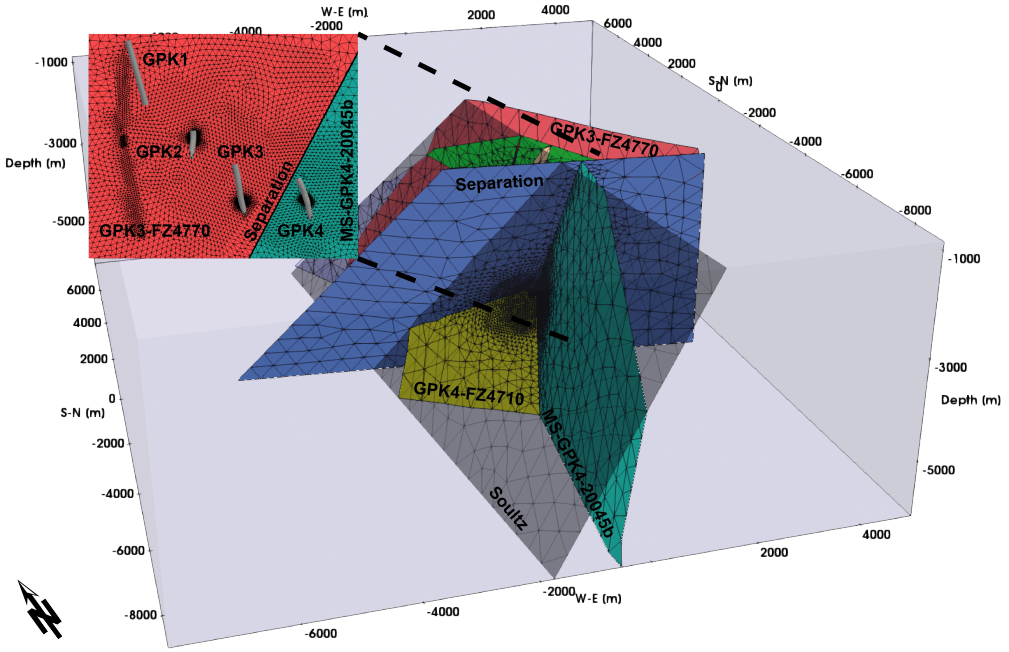

Figure 8.1: Subset of the mesh for the FE-modeling with the main faults and fractures in the Soultz reservoir (modified after Held et al., 2014). The central area around along around the deep wells is shown in detail.

Structure	Transmissivity [$m^2\,s^{-1}$]
GPK1-FZ2856	5.0×10^{-5}
GPK4-FZ4710	3.8×10^{-5}
MS-GPK2-2000a	5.1×10^{-5}
MS-GPK4-20045b	3.2×10^{-5}
PS3-Int	6.4×10^{-4}
Separation	6.8×10^{-5}
GPK3-FZ4770 around GPK2	5.7×10^{-5}

Table 8.1: Transmissivities of the different faults and fractures. Only structures with changes compared to Held et al. (2014) are shown.

tracer experiment conducted in 2005 (Sanjuan et al., 2006). Table 8.1 shows the transmissivity of the fractures which differ from Held et al. (2014).

A linear temperature gradient is defined by fixing the top and bottom boundary. The temperature gradient is in accordance to Held et al. (2014), assuming a gradient of $0.026\,K\,m^{-1}$ and an upper boundary temperature of 101 °C. Streamline Upwind method is used to increase the stability of the simulations (Brooks and Hughes, 1982). According to Kestin et al. (1981), a brine with a constant density of $1065\,kg\,m^{-3}$ and dynamic viscosity of $2.32 \times 10^{-4}\,Pa\,s$, representing a fluid at a temperature of 150 °C, pore pressure of 35 MPa and salinity of $1.5\,mol\,kg^{-1}$, is assumed. The different thermal and hydraulic material properties of the matrix, fractures, and fluid are shown in Table 8.2. Mixture properties

	Matrix	Fractures	Brine
Porosity [-]	0.01	1	-
Compressibility [Pa^{-1}]	5×10^{-13}	10^{-9}	5×10^{-10}
Specific heat capacity [$J\,kg^{-1}\,K$]	950	950	3950
Density [$kg\,m^{-3}$]	2316	2316	1065
Thermal conductivity [$W\,m^{-1}\,K$]	3	0.6	0.6

Table 8.2: Material properties of the matrix and fractures.

are calculated internally with the porosity of the element, leading to effective fluid properties in the fractures.

8.3 RESULTS

8.3.1 *Old power plant design*

Held et al. (2014) carried out long-term forecast modeling and economic evaluation of the Soultz EGS. The assigned flow rates for the analysis were $13\,kg\,s^{-1}$ (GPK1), $-26\,kg\,s^{-1}$ (GPK2) and $10\,kg\,s^{-1}$ (GPK3). Note that negative mass rates mean fluid extraction, while positive values represent an injection of mass. The reinjection temperature was fixed with 70 °C. For comparison reasons, the new simulation was done with the same flow rates. Figure 8.2 shows the temperature at the top of the open-hole section in the GPK2 well for 60 years as a result of ongoing and constant production/injection for the new simulation and the comparison to Held et al. (2014).

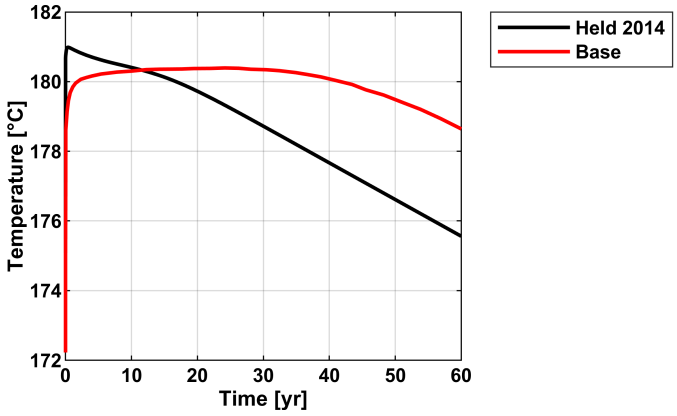

Figure 8.2: Comparison of the temperature in the well GPK2 of Held et al. (2014) and the recalibrated model.

In the first couple of days, a strong temperature increase is shown in both simulations with a maximum temperature of 181 °C (current simulation) and 180 °C (Held et al., 2014). The maximum temperature of GPK2 was simulated after less than a year, while the older model expected a long-lasting, but slow temperature increase up to the year 25. Afterward the temperature decreases

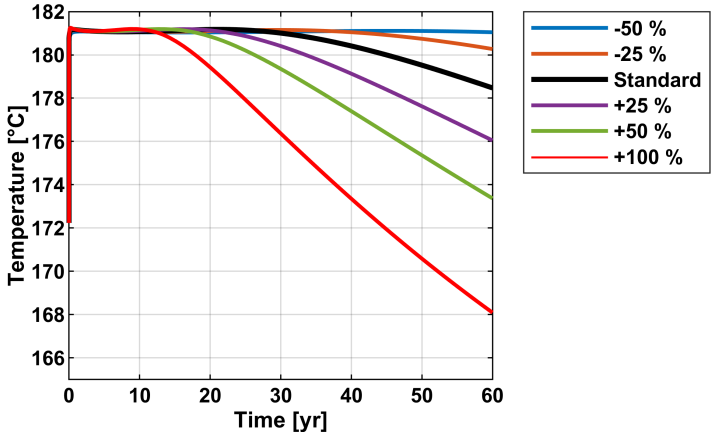

Figure 8.3: Temperature at the top of GPK2 open-hole section after 60 years of forecast modeling. The flow rates of the three wells GPK2 to GPK4 were changed as a ratio of the current standard power plant design (Mouchot et al., 2018). The injection temperature was kept constant with 70 °C.

until the end of the simulation (60 years) to 175 °C and 178 °C, respectively. The temperature breakthrough in the new simulation was achieved by the good hydraulic connection of the GPK2 and GPK1 wells when cold fluids sink along the fractures in the deeper areas of the geothermal reservoir. The described connection of GPK3 and GPK2 contributed only slightly to the cooling of GPK2 even with increasing time runtime. The GPK4 well was not used for this production concept, as its hydraulic connection to the reservoir is significantly less favorable than that of the other wells.

8.3.2 *Current power plant operation*

After 30 years of research activities, the power plant was put into commercial operation in 2015. As the old power plant design expected a hydraulic short circuit and thermal breakthrough between the GPK1 and GPK2 wells, the production and injection design were changed to avoid cooling in the production well with increasing uptime (Mouchot et al., 2018). GPK2 is still used as a production well, while the fluid is reinjected in GPK3 and GPK4 well with a temperature of 70 °C (BINE Information Service, 2017). The current flow rates are $-30\,\mathrm{kg\,s^{-1}}$ (GPK2), $20\,\mathrm{kg\,s^{-1}}$ (GPK3) and $10\,\mathrm{kg\,s^{-1}}$ (GPK4). The conducted thermo-hydraulic simulations allow the forecast of the cooling in the Soultz reservoir. Additionally, the influence of de-/increased flow rates and changed injection temperatures to the long-term behavior of the current power plant design was investigated. It was assumed that the current power plant design is the standard case, percentage changes of the flow rates always refer to this setup.

Figure 8.3 shows the temperature at the top of the open-hole section of the GPK2 well with increasing simulation time when the flow rates of the wells GPK2 to GPK4 are uniformly changed between −50 % and 100 % of the standard rates. All models show an instant temperature increase after the start of operation up to 181 °C, a long period of constant production temperature and a decline

until the end of the simulations. The expected minimum production temperature for the standard case after 60 years was 178 °C (−3 K) and a first reduction of the temperature was simulated after 25 years of continuous operation. The models show that even a 50 % reduction in flow rates would completely prevent a thermal breakthrough at the GPK2 well within the forecast period. In contrast, an increase in the overall flow rates could lead to a faster thermal breakthrough and reduced temperatures after 60 years. The simulations show that a doubling of the flow rates leads to a reduction of the fluid temperature of 13 K to 168 °C and first indicators for a thermal breakthrough after 11 years of production.

As shown in Figure 8.4, at the end of the standard simulation, the cooling area is mainly oriented along the affected faults- and fractures GPK3-FZ4770 and MS-GPK4-20045b. Fluids that were cooled and reinjected into GPK3 well affect the producer GPK2 and decreased the production temperature. The GPK4 well has just a low hydraulic connection to GPK3, which means that its influence on production temperatures is negligible. In addition, the spread of the cooling front is significantly smaller, as the injection rates are just half of GPK3.

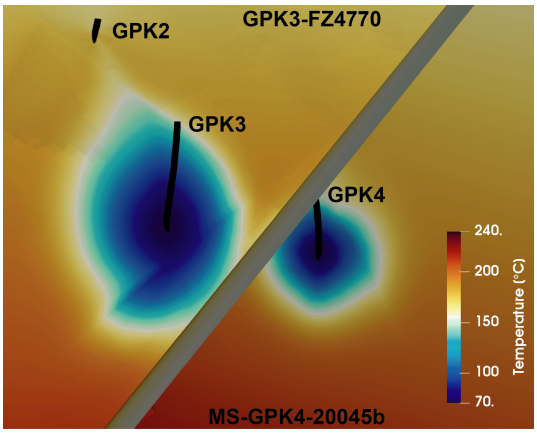

Figure 8.4: Temperature distribution on the fractures GPK3-FZ4770 and MS-GPK4-20045b after 60 years of production and injection in the standard case.

Figure 8.5 shows the change in the fluid temperature at the top of the open-hole section of the GPK2 well with increasing simulation time when the injection temperature of GPK3 and GPK4 was changed as opposed to the standard case. In comparison to the change in flow rates, the effect of a changed injection temperature is very small. A change in the final fluid temperature of less than one degree (178 − 179 °C) can be expected after 60 years of continuous operation. All investigated variants are consistent with the standard case, the temperature increased at the beginning of the operation to 181 °C and a first reduction the fluid temperature was simulated after 25 years.

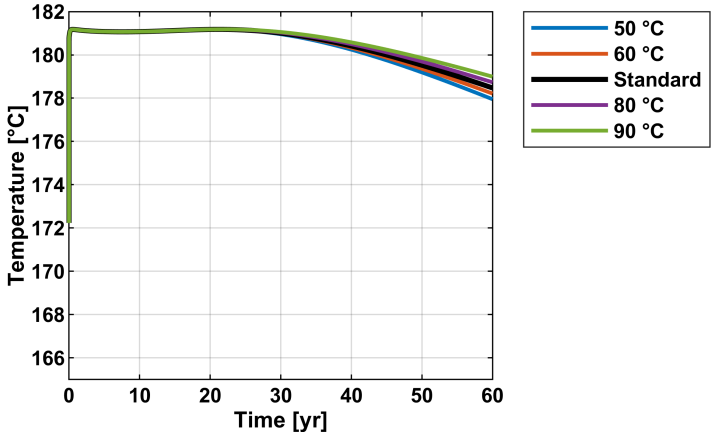

Figure 8.5: Temperature at the top of GPK2 open-hole section after 60 years of forecast modeling. The injection temperature of the wells GPK3 and GPK4 was changed, while the flow rates were kept constant. The standard injection temperature was 70 °C.

8.4 SUMMARY

The recently developed numerical models of the Soultz-sous-Forêts geothermal reservoir were solved with the thermo-hydraulic application TIGER. Different kinds of experiments, like circulation and tracer experiments, were used to update the calibration of the fault and fracture network with respect to the hydraulic connections, the natural and artificial fluid flow along the network as well as the wells GPK1 to GPK4.

Based on the recent production design of the Soultz EGS, forecast-modeling was performed that focused on the long-term development of the production temperature. After 60 years of continuous production, a temperature drop of 3 K was simulated. It could be shown, that the production and injection flow rates have significant influence on the temperature decline and thermal sustainability of the reservoir. While a 50 % reduction of the flow rates would prevent any thermal breakthrough, a doubling of flow rates would result in a 13 K temperature decrease. On the other hand, changes in the injection temperature ($\pm$20 K) has a negligible influence on the long-term temperatures.

ACKNOWLEDGMENTS

We thank the Federal Ministry for Economic Affairs and Energy (BMWi) for the support through the 'GeoFaces-SD' project (No. 0324025C).

9

CONCLUSIONS

Strengthened exploitation of geothermal resources is essential to achieve the climate goals for this century outlined in the introduction, as it offers the possibility of covering both peak and baseload capacity (IEA, 2017). Specifically, deep geothermal energy from Enhanced Geothermal Systems (EGS) can generate large amounts of heat and electricity at almost any location on Earth. A prime example is the Upper Rhine Graben, which offers an optimal basis for geothermal energy utilization with elevated temperatures of up to 200 °C at a depth of 5 km. Unfortunately, the initial investment costs are still very high compared to the geological risks. These include drilling challenges and, above all, the need to achieve sufficient hydraulic conductivity to extract large quantities of water and heat from the deep underground. In the case of the EGS, the fluid localizes within a network of well-permeable fractures and faults, while the host rock itself is impermeable (Genter et al., 2010). Therefore, a better knowledge of the multiscale fluid flow in fractured geothermal reservoirs is crucial for the safe and sustainable operation of geothermal installations.

The research within this thesis aimed at the process understanding and quantification of fluid flow and related coupled thermo-hydro-mechanical processes within fractures and fracture networks to address various problems and sometimes contradictory observations related to geothermal reservoir exploration. The knowledge is of vast importance since fluid flow is often highly simplified concerning the geometrical constraints as well as the flow regime and thus imposes several uncertainties. Towards achieving this goal, a workflow was developed that combines experimental laboratory and field data with numerical models. In doing so, it is possible to describe the fractured reservoir and the mutual coupling of relevant physical processes on multiple temporal and spatial scales. This work thus promotes the understanding of the small-scale geomechanical formation of rock fractures and localized hydraulic pathways within them, to the large-scale flow field within a regional fault and fracture network. The main results of the studies (Chapter 4 through 8) are summarized in the following section.

9.1 MAJOR FINDINGS OF THE RESEARCH

The majority of current studies on fracture flow either assume fractures as two opposing parallel plates or use a calculated aperture field in order to be able to represent the geometric properties in simple two-dimensional models.

In doing so, most studies tend to neglect the feedback effects of the tortuous fracture void geometry and introduce uncertainties of unknown extent that can have massive implications for the successful operation when applied to large-scale reservoir models. My aim in Chapters 4 and 5 was the simulation of high-resolution fluid flow in a single fracture without any simplifications in order to find and quantify the controlling processes of the rising uncertainties and sometimes contradicting observations from hydraulic tests. In Chapter 4, a spatially resolved comparison between the three-dimensional Navier-Stokes equations (NSE) and the simplified local cubic law (LCL) revealed that the LCL validity at geothermal-typical flow rates depends on the complex interplay of geometric and hydraulic framework conditions. A perpendicular orientation of flow and shearing leads to the formation of well-developed fluid pathways in which an ideal parabolic flow can be maintained even at high flow rates, providing a good match between NSE and LCL.

In Chapter 5 could be shown that these ideal channels constitute only a small fraction of the total fracture volume, whereas large parts of the entire domain represent stagnant-water-zones, where the exchange of heat and solutes with the surrounding host rock is very limited. The situation is different when flow and shearing are oriented in parallel. Although poorly connected channels lead to greater uncertainty in expected flow rates, the resulting elongated flow path length leads to lower local hydraulic gradients and velocities and an enlarged heat exchanger area. Transferred to the reservoir scale, a normal stress regime, with vertically displaced surfaces and horizontal flow between wells, allows higher flow rates and improved prediction with simplified models but also favors thermal breakthroughs on shorter timescales.

In Chapter 6, I presented an approach to establish nonlinear relationships between porous rocks and the expected material properties of deep geothermal reservoirs employing limited laboratory investigations. It was shown that numerical models allow us to upscale and predict microstructural processes such as the nonlinear elastoplastic deformation of a porous medium and the associated changes in structural, mechanical, and transport properties. Laboratory observations (including triaxial and permeameter measurements) on different types of low-permeable sandstones from the Upper Rhine Graben are utilized to obtain detailed information on the thermo-poroelastic as well as failure behavior in typical geothermal environments and serve as constraints and boundary conditions for advanced numerical reservoir modeling. This nonlinear geomechanical behavior and shearing of intact rock masses can significantly alter the transport of heat and solutes within the low-permeability host rock and in the fracture network.

The major findings from these small-scale investigations are leveraged to understand the processes and dynamics involved in the large-scale flow regime in typical EGS. Natural and artificial fractures and fault zones are spatially highly localized discontinuities in a low-permeability host rock that control the thermo-hydro-mechanical framework of the entire system. Challenges are posed in identifying the influencing structural features as well as the best possible numerical integration. Special attention must be paid to the geometric description of the individual fractures and faults, which, depending on the history

of deformation, pressure, and temperature, and the resulting microstructural processes, form a complex and heterogeneous entity of hydraulic conductors and barriers (Chapter 1). Exemplified by the highly dynamic Soultz-sous-Forêts EGS and the unique basis of experimental data, in Chapter 7 I developed a novel workflow to describe the flow regime within the EGS and subsequently to make predictions about its future sustainable utilization (Chapter 8). Multiple circulation and tracer experiments as well as individual flow logs were evaluated to identify the constraints and boundary conditions for the numerical reservoir model. While circulation experiments are only suitable for the near-wellbore characterization of the hydraulic regime, three-dimensional, large-scale, and numerically stable models of solute transport represent a novel approach to characterize the formation of preferential flow paths along with a reservoir fracture network. For the Soultz EGS, I was able to show that the GPK1, GPK2, and GPK3 wells are connected along different fractures. In addition, a fault zone between GPK3 and GPK4 could be identified, which hydraulically decouples them from each other but connects the reservoir to the natural flow regime of the URG. Although the recent stress field rather indicates a sealed fault zone, it represents a combined conduit barrier according to the concept of Caine et al. (1996), thus illustrating the complexity and heterogeneity of geological discontinuities and their dynamic evolution. The hydraulic model was further elaborated in Chapter 8 in order to capture the thermo-hydraulic performance of the geothermal reservoir and to predict expected temperatures. The current operating scheme shows a slight decrease in temperature after a few decades. The response to a change in injection temperature is only slight; in contrast, increased flow rates lead to an accelerated decrease in production temperature.

9.2 OUTLOOK

The present work highlighted that the transfer of laboratory and field experimental data to large-scale geothermal reservoirs is and will remain a challenging and important task. The studies shown focus on either coupled but simplified processes or static nonlinear flow effects. Future research in the field of fracture flow should focus on the nonlinear nature of high-resolution fluid flow in combination with the transient effects (in terms of temperature, pore pressure, and mechanical deformation) induced by artificial changes during reservoir operation and hydraulic stimulation. For small scales, flow-through experiments on artificial and natural fractures are an appropriate method, while for medium to large scales, underground research laboratories, such as those at Grimsel or Bedretto, are necessary. Numerically, the limited availability of multiscale material parameters and the explicit geometric description of fractures are the major obstacles in upscaling. The extended finite element method provides a way to circumvent these limitations and account for discontinuities without mesh refinement (Khoei, 2015). To the author's knowledge, this method has been successfully applied for flow problems only in 2D.

More generally, I have also shown that microscopic processes, such as the formation of preferential fluid paths, can significantly alter the large-scale thermo-

hydro-mechanical dynamics of an EGS. Therefore, the overarching goal must be to understand and predict the multiscale and multiphysical processes in the reservoir during project development to ensure productive, sustainable, and environmentally friendly geothermal operations. In this context, the linkage of experiments with complex and coupled numerical models represents an indispensable tool to bridge the different temporal and spatial scales and to capture the nonlinear nature of these systems.

REFERENCES

Adams, M. C. and Davis, J. (1991). "Kinetics of fluorescein decay and its application as a geothermal tracer." In: *Geothermics* 20.1-2, pp. 53–66. ISSN: 03756505. DOI: 10.1016/0375-6505(91)90005-G.

Adler, P. M., Thovert, J.-F., and Mourzenko, V. V. (2012). *Fractured Porous Media*. Oxford University Press. ISBN: 9780199666515. DOI: 10.1093/acprofoso/9780199666515.001.0001.

Afshari Moein, M. J., Somogyvári, M., Valley, B., Jalali, M., Loew, S., and Bayer, P. (2018). "Fracture Network Characterization Using Stress-Based Tomography." In: *Journal of Geophysical Research: Solid Earth* 123.11, pp. 9324–9340. ISSN: 21699313. DOI: 10.1029/2018JB016438.

Agemar, T., Alten, J.-A., Ganz, B., Kuder, J., Kühne, K., Schumacher, S., and Schulz, R. (2014). "The Geothermal Information System for Germany – GeotIS." In: *Zeitschrift der Deutschen Gesellschaft für Geowissenschaften* 165.2, pp. 129–144. ISSN: 18601804. DOI: 10.1127/1860-1804/2014/0060.

Agemar, T., Brunken, J., Jodocy, M., Schellschmidt, R., Schulz, R., and Stober, I. (2013). "Untergrundtemperaturen in Baden-Württemberg." In: *Zeitschrift der Deutschen Gesellschaft für Geowissenschaften* 164.1, pp. 49–62. ISSN: 18601804. DOI: 10.1127/1860-1804/2013/0010.

Aichholzer, C., Duringer, P., Orciani, S., and Genter, A. (2016). "New stratigraphic interpretation of the Soultz-sous-Forêts 30-year-old geothermal wells calibrated on the recent one from Rittershoffen (URG, France)." In: *Geothermal Energy* 4.1. ISSN: 2195-9706. DOI: 10.1186/s40517-016-0055-7.

Akber Hassan, W. A. and Jiang, X. (2012). "Upscaling and its application in numerical simulation of long-term CO 2 storage." In: *Greenhouse Gases: Science and Technology* 2.6, pp. 408–418. ISSN: 21523878. DOI: 10.1002/ghg.1306.

Al-Yaarubi, A. H., Pain, C. C., Grattoni, C. A., and Zimmerman, R. W. (2005). "Navier-Stokes Simulations of Fluid Flow Through a Rock Fracture." In: *Dynamics of Fluids and Transport in Fractured Rock*. Ed. by B. Faybishenko, P. A. Witherspoon, and J. Gale. Vol. 17. Geophysical monograph. Washington, D. C.: American Geophysical Union, pp. 55–64. ISBN: 9781118666173. DOI: 10.1029/162GM07.

Allègre, C. J., Le Mouel, J. L., and Provost, A. (1982). "Scaling rules in rock fracture and possible implications for earthquake prediction." In: *Nature* 297.5861, pp. 47–49. DOI: 10.1038/297047a0.

Amann, F., Gischig, V., Evans, K., Doetsch, J., Jalali, R., Valley, B., Krietsch, H., Dutler, N., Villiger, L., Brixel, B., Klepikova, M., Kittilä, A., Madonna, C., Wiemer, S., Saar, M. O., Loew, S., Driesner, T., Maurer, H., and Giardini, D. (2018). "The seismo-hydromechanical behavior during deep geothermal reservoir stimulations: open questions tackled in a decameter-scale in situ stimulation experiment." In: *Solid Earth* 9.1, pp. 115–137. ISSN: 1869-9529. DOI: 10.5194/se-9-115-2018.

Aquilina, L., Dreuzy, J.-R. de, Bour, O., and Davy, P. (2004). "Porosity and fluid velocities in the upper continental crust (2 to 4 km) inferred from injection tests at the Soultz-sous-Forêts geothermal site." In: *Geochimica et Cosmochimica Acta* 68.11, pp. 2405–2415. ISSN: 00167037. DOI: 10.1016/j.gca.2003.08.023.

Aquilina, L., Rose, P., Brach, M., Gentier, S., Jeannot, R., Jacquot, E., Audigane, P., Tran-Vie, T., Jung, R., Baumgärtner, J., Baria, R., and Gérard, A. (1998). *A Tracer Test at the Soultz-Sous-Forêts Hot Dry Rock Geothermal Site: PROCEEDINGS Twenty-Third Workshop on Geothermal Reservoir Engineering*. Stanford, California.

Aris, R. (1956). "On the dispersion of a solute in a fluid flowing through a tube." In: *Proceedings of the Royal Society of London. Series A. Mathematical and Physical Sciences* 235.1200, pp. 67–77. ISSN: 0080-4630. DOI: 10.1098/rspa.1956.0065.

Auradou, H., Drazer, G., Hulin, J. P., and Koplik, J. (2005). "Permeability anisotropy induced by the shear displacement of rough fracture walls." In: *Water Resources Research* 41.9. ISSN: 00431397. DOI: 10.1029/2005WR003938.

Auradou, H., Hulin, J. P., and Roux, S. (2001). "Experimental study of miscible displacement fronts in rough self-affine fractures." In: *Physical review. E, Statistical, nonlinear, and soft matter physics* 63.6 Pt 2, p. 066306. DOI: 10.1103/PhysRevE.63.066306.

Auradou, H., Drazer, G., Boschan, A., Hulin, J.-P., and Koplik, J. (2006). "Flow channeling in a single fracture induced by shear displacement." In: *Geothermics* 35.5-6, pp. 576–588. ISSN: 03756505. DOI: 10.1016/j.geothermics.2006.11.004.

Aydin, A. (2000). "Fractures, faults, and hydrocarbon entrapment, migration and flow." In: *Marine and Petroleum Geology* 17.7, pp. 797–814. ISSN: 02648172. DOI: 10.1016/S0264-8172(00)00020-9.

Ayling, B. F., Hogarth, R. A., and Rose, P. E. (2016). "Tracer testing at the Habanero EGS site, central Australia." In: *Geothermics* 63, pp. 15–26. ISSN: 03756505. DOI: 10.1016/j.geothermics.2015.03.008.

Azizmohammadi, S. and Matthäi, S. K. (2017). "Is the permeability of naturally fractured rocks scale dependent?" In: *Water Resources Research* 53.9, pp. 8041–8063. ISSN: 00431397. DOI: 10.1002/2016WR019764.

BINE Information Service (2017). *Projektinfo 10/2017: German-French geothermal power plant completed*.

BMUB (2016). *Klimaschutzpolitische Grundsätze und Ziele der Bundesregierung*.

Bächler, D., Kohl, T., and Rybach, L. (2003). "Impact of graben-parallel faults on hydrothermal convection—-Rhine Graben case study." In: *Physics and Chemistry of the Earth, Parts A/B/C* 28.9-11, pp. 431–441. ISSN: 14747065. DOI: 10.1016/S1474-7065(03)00063-9.

Balay, S., Abhyankar, S., Adams, M., Brown, J., Brune, P., Buschelman, K., Dalcin, L., Eijkhout, V., Gropp, W., Karpeyev, D., Kaushik, D., Knepley, M., Curfman McInnes, L., Rupp, K., Smith, B., Zampini, S., and Zhang, H. (2016). *PETSc User Manual, Technical Report ANL-95/11 - Revision 3.7*. Argonne National Laboratory.

Bandis, S., Lumsden, A. C., and Barton, N. R. (1981). "Experimental studies of scale effects on the shear behaviour of rock joints." In: *International Journal of Rock Mechanics and Mining Sciences & Geomechanics Abstracts* 18.1, pp. 1–21. ISSN: 01489062. DOI: 10.1016/0148-9062(81)90262-X.

Barton, C. A., Hickman, S., Morin, R. H., Zoback, M. D., Finkbeiner, T., Sass, J., and Benoit, D. (1997). *Fracture Permeability and its Relationship to in-situ stress in the dixie valley, nevada, geothermal reservoir: PROCEEDINGS Twenty-Second Workshop on Geothermal Reservoir Engineering*. Stanford, California.

Barton, C. A., Zoback, M. D., and Moos, D. (1995). "Fluid flow along potentially active faults in crystalline rock." In: *Geology* 23.8, p. 683. ISSN: 0091-7613.

Barton, N., Bandis, S., and Bakhtar, K. (1985). "Strength, deformation and conductivity coupling of rock joints." In: *International Journal of Rock Mechanics and Mining Sciences & Geomechanics Abstracts* 22.3, pp. 121–140. ISSN: 01489062. DOI: 10.1016/0148-9062(85)93227-9.

Barton, N. and Choubey, V. (1977). "The shear strength of rock joints in theory and practice." In: *Rock Mechanics Felsmechanik Mecanique des Roches* 10.1-2, pp. 1–54. ISSN: 0035-7448. DOI: 10.1007/BF01261801.

Barton, N. (2016). "Non-linear shear strength for rock, rock joints, rockfill and interfaces." In: *Innovative Infrastructure Solutions* 1.1. ISSN: 2364-4176. DOI: 10.1007/s41062-016-0011-1.

Bataillé, A., Genthon, P., Rabinowicz, M., and Fritz, B. (2006). "Modeling the coupling between free and forced convection in a vertical permeable slot: Implications for the heat production of an Enhanced Geothermal System." In: *Geothermics* 35.5-6, pp. 654–682. ISSN: 03756505. DOI: 10.1016/j.geothermics.2006.11.008.

Baud, P., Zhu, W., and Wong, T.-f. (2000). "Failure mode and weakening effect of water on sandstone." In: *Journal of Geophysical Research* 105.B7, pp. 16371–16389. ISSN: 0148-0227. DOI: 10.1029/2000JB900087.

Bauer, J. F., Krumbholz, M., Meier, S., and Tanner, D. C. (2017). "Predictability of properties of a fractured geothermal reservoir: the opportunities and limitations of an outcrop analogue study." In: *Geothermal Energy* 5.1, p. 65. ISSN: 2195-9706. DOI: 10.1186/s40517-017-0081-0.

Bauer, J. F., Meier, S., and Philipp, S. L. (2015). "Architecture, fracture system, mechanical properties and permeability structure of a fault zone in Lower Triassic sandstone, Upper Rhine Graben." In: *Tectonophysics* 647-648, pp. 132–145. ISSN: 00401951. DOI: 10.1016/j.tecto.2015.02.014.

Bauget, F. and Fourar, M. (2007). *Convective dispersion in a real fracture: PROCEEDINGS 32nd Workshop on Geothermal Reservoir Engineering*. Stanford, California.

Baujard, C. and Bruel, D. (2006). "Numerical study of the impact of fluid density on the pressure distribution and stimulated volume in the Soultz HDR reservoir." In: *Geothermics* 35.5-6, pp. 607–621. ISSN: 03756505. DOI: 10.1016/j.geothermics.2006.10.004.

Bear, J. (1988). *Dynamics of fluids in porous media*. Dover books on physics and chemistry. New York: Dover. ISBN: 9780486656755.

Bear, J. and Cheng, A. H.-D. (2010). *Modeling Groundwater Flow and Contaminant Transport*. Vol. 23. Theory and Applications of Transport in Porous Media. Dordrecht: Springer Netherlands. ISBN: 9781402066818. DOI: 10.1007/978-1-4020-6682-5.

Bear, J., Tsang, C.-F., and Marsily, G. de (1993). *Flow and Contaminant Transport in Fractured Rock*. Burlington: Elsevier Science. ISBN: 0120839806.

Becker, M. W. and Shapiro, A. M. (2000). "Tracer transport in fractured crystalline rock: Evidence of nondiffusive breakthrough tailing." In: *Water Resources Research* 36.7, pp. 1677–1686. ISSN: 00431397. DOI: 10.1029/2000WR900080.

Berkowitz, B. (2002). "Characterizing flow and transport in fractured geological media: A review." In: *Advances in Water Resources* 25.8-12, pp. 861–884. ISSN: 03091708. DOI: 10.1016/S0309-1708(02)00042-8.

Berkowitz, B., Bour, O., Davy, P., and Odling, N. (2000). "Scaling of fracture connectivity in geological formations." In: *Geophysical Research Letters* 27.14, pp. 2061–2064. ISSN: 00948276. DOI: 10.1029/1999GL011241.

Berkowitz, B., Naumann, C., and Smith, L. (1994). "Mass transfer at fracture intersections: An evaluation of mixing models." In: *Water Resources Research* 30.6, pp. 1765–1773. ISSN: 00431397. DOI: 10.1029/94WR00432.

Bernabé, Y., Mok, U., and Evans, B. (2003). "Permeability-porosity Relationships in Rocks Subjected to Various Evolution Processes." In: *Pure and Applied Geophysics* 160.5-6, pp. 937–960. ISSN: 0033-4553. DOI: 10.1007/PL00012574.

Berre, I., Doster, F., and Keilegavlen, E. (2019). "Flow in Fractured Porous Media: A Review of Conceptual Models and Discretization Approaches." In: *Transport in Porous Media* 130.1, pp. 215–236. ISSN: 0169-3913. DOI: 10.1007/s11242-018-1171-6.

Bésuelle, P. (2001). "Evolution of strain localisation with stress in a sandstone: Brittle and semi-brittle regimes." In: *Physics and Chemistry of the Earth, Part A: Solid Earth and Geodesy* 26.1-2, pp. 101–106. ISSN: 14641895. DOI: 10.1016/S1464-1895(01)00032-1.

Biot, M. A. (1956). "General solutions of the equations of elasticity and consolidation for a porous material." In: *J. Appl. Mech.* 78, pp. 91–96.

Blöcher, G., Kluge, C., Milsch, H., Cacace, M., Jacquey, A. B., and Schmittbuhl, J. (2019). "Permeability of matrix-fracture systems under mechanical loading – constraints from laboratory experiments and 3-D numerical modelling." In: *Advances in Geosciences* 49, pp. 95–104. DOI: 10.5194/adgeo-49-95-2019.

Blumenthal, M., Kühn, M., Pape, H., Rath, V., and Clauser, C. (2007). "Hydraulic model of the deep reservoir quantifying the multi-well tracer test." In: *Paper presented at EHDRA Scientific Conference, 28-29 June 2007*.

Bodin, J., Delay, F., and Marsily, G. de (2003a). "Solute transport in a single fracture with negligible matrix permeability: 1. fundamental mechanisms." In: *Hydrogeology Journal* 11.4, pp. 418–433. ISSN: 1431-2174. DOI: 10.1007/s10040-003-0268-2.

Bodin, J., Delay, F., and Marsily, G. de (2003b). "Solute transport in a single fracture with negligible matrix permeability: 2. mathematical formalism." In: *Hydrogeology Journal* 11.4, pp. 434–454. ISSN: 1431-2174. DOI: 10.1007/s10040-003-0269-1.

Bonnet, E., Bour, O., Odling, N. E., Davy, P., Main, I., Cowie, P., and Berkowitz, B. (2001). "Scaling of fracture systems in geological media." In: *Reviews of Geophysics* 39.3, pp. 347–383. ISSN: 87551209. DOI: 10.1029/1999RG000074.

Bour, O. (2002). "A statistical scaling model for fracture network geometry, with validation on a multiscale mapping of a joint network (Hornelen Basin, Norway)." In: *Journal of Geophysical Research* 107.B6. ISSN: 0148-0227. DOI: 10.1029/2001JB000176.

Brooks, A. N. and Hughes, T. J. (1982). "Streamline upwind/Petrov-Galerkin formulations for convection dominated flows with particular emphasis on the incompressible Navier-Stokes equations." In: *Computer Methods in Applied Mechanics and Engineering* 32.1-3, pp. 199–259. ISSN: 00457825. DOI: 10.1016/0045-7825(82)90071-8.

Brown, S. R. (1987). "Fluid flow through rock joints: The effect of surface roughness." In: *Journal of Geophysical Research* 92.B2, p. 1337. ISSN: 0148-0227. DOI: 10.1029/JB092iB02p01337.

Brown, S. R. (1989). "Transport of fluid and electric current through a single fracture." In: *Journal of Geophysical Research* 94.B7, p. 9429. ISSN: 0148-0227. DOI: 10.1029/JB094iB07p09429.

Brown, S. R., Stockman, H. W., and Reeves, S. J. (1995). "Applicability of the Reynolds Equation for modeling fluid flow between rough surfaces." In: *Geophysical Research Letters* 22.18, pp. 2537–2540. ISSN: 00948276. DOI: 10.1029/95GL02666.

Bruderer-Weng, C., Cowie, P., Bernabé, Y., and Main, I. (2004). "Relating flow channelling to tracer dispersion in heterogeneous networks." In: *Advances in Water Resources* 27.8, pp. 843–855. ISSN: 03091708. DOI: 10.1016/j.advwatres.2004.05.001.

Brush, D. J. and Thomson, N. R. (2003). "Fluid flow in synthetic rough-walled fractures: Navier-Stokes, Stokes, and local cubic law simulations." In: *Water Resources Research* 39.4, p. 1337. ISSN: 00431397. DOI: 10.1029/2002WR001346.

Byerlee, J. D. (1978). "Friction of Rocks." In: *Pure and Applied Geophysics* 116(4-5), pp. 615–626. ISSN: 0033-4553.

Cacace, M. and Jacquey, A. B. (2017). "Flexible parallel implicit modelling of coupled thermal–hydraulic–mechanical processes in fractured rocks." In: *Solid Earth Discussions* 8.5, pp. 921–941. ISSN: 1869-9537. DOI: 10.5194/se-8-921-2017.

Caine, J. S., Evans, J. P., and Forster, C. B. (1996). "Fault zone architecture and permeability structure." In: *Geology* 24.11, p. 1025. ISSN: 0091-7613.

Calò, M., Dorbath, C., and Lubrano Lavadera, P. (2016). "Can faults become barriers for deep fluid circulation? Insights from high-resolution seismic VSP tomography at the Soultz-sous-Forêts geothermal site." In: *Geophysical Research Letters* 43.17, pp. 8986–8993. ISSN: 00948276. DOI: 10.1002/2016GL069623.

Carman, P. (1956). *Flow of gases through porous media*. London: Butterworths Scientific Publications.

Carroll, M. M. and Katsube, N. (1983). "The Role of Terzaghi Effective Stress in Linearly Elastic Deformation." In: *Journal of Energy Resources Technology* 105.4, pp. 509–511. ISSN: 0195-0738. DOI: 10.1115/1.3230964.

Chang, C., Zoback, M. D., and Khaksar, A. (2006). "Empirical relations between rock strength and physical properties in sedimentary rocks." In: *Journal of Petroleum Science and Engineering* 51.3-4, pp. 223–237. ISSN: 09204105. DOI: 10.1016/j.petrol.2006.01.003.

Chen, Y., Durlofsky, L. J., Gerritsen, M., and Wen, X. H. (2003). "A coupled local–global upscaling approach for simulating flow in highly heterogeneous formations." In: *Advances in Water Resources* 26.10, pp. 1041–1060. ISSN: 03091708. DOI: 10.1016/S0309-1708(03)00101-5.

Chen, Y.-F., Zhou, J.-Q., Hu, S.-H., Hu, R., and Zhou, C.-B. (2015). "Evaluation of Forchheimer equation coefficients for non-Darcy flow in deformable rough-walled fractures." In: *Journal of Hydrology* 529, pp. 993–1006. ISSN: 00221694. DOI: 10.1016/j.jhydrol.2015.09.021.

Chen, Y. and Zhao, Z. (2020). "Heat transfer in a 3D rough rock fracture with heterogeneous apertures." In: *International Journal of Rock Mechanics and Mining Sciences* 134, p. 104445. ISSN: 13651609. DOI: 10.1016/j.ijrmms.2020.104445.

Chen, Z., Narayan, S. P., Yang, Z., and Rahman, S. S. (2000). "An experimental investigation of hydraulic behaviour of fractures and joints in granitic rock." In: *International Journal of Rock Mechanics and Mining Sciences* 37.7, pp. 1061–1071. ISSN: 13651609. DOI: 10.1016/S1365-1609(00)00039-3.

Cheng, C., Hale, S., Milsch, H., and Blum, P. (2020). "Measuring hydraulic fracture apertures: a comparison of methods." In: *Solid Earth* 11.6, pp. 2411–2423. ISSN: 1869-9529. DOI: 10.5194/se-11-2411-2020.

Choi, J.-H., Edwards, P., Ko, K., and Kim, Y.-S. (2016). "Definition and classification of fault damage zones: A review and a new methodological approach." In: *Earth-Science Reviews* 152, pp. 70–87. ISSN: 00128252. DOI: 10.1016/j.earscirev.2015.11.006.

Chokshi, A. H., Rosen, A., Karch, J., and Gleiter, H. (1989). "On the validity of the hall-petch relationship in nanocrystalline materials." In: *Scripta Metallurgica* 23.10, pp. 1679–1683. ISSN: 00369748. DOI: 10.1016/0036-9748(89)90342-6.

Christie, M. A. and Blunt, M. J. (2001). "Tenth SPE Comparative Solution Project: A Comparison of Upscaling Techniques." In: *SPE Reservoir Simulation Symposium*. Society of Petroleum Engineers. DOI: 10.2118/66599-MS.

Chrysochoos, A., Maisonneuve, O., Martin, G., Caumon, H., and Chezeaux, J. C. (1989). "Plastic and dissipated work and stored energy." In: *Nuclear Engineering and Design* 114.3, pp. 323–333. ISSN: 00295493. DOI: 10.1016/0029-5493(89)90110-6.

Clauser, C. (1992). "Permeability of crystalline rocks." In: *Eos, Transactions American Geophysical Union* 73.21, p. 233. ISSN: 0096-3941. DOI: 10.1029/91EO00190.

Cornet, F. H., Bérard, T., and Bourouis, S. (2007). "How close to failure is a granite rock mass at a 5km depth?" In: *International Journal of Rock Mechanics and Mining Sciences* 44.1, pp. 47–66. ISSN: 13651609. DOI: 10.1016/j.ijrmms.2006.04.008.

Coulomb, C. (1773). "Application des règles de maxima et minima à quelques problèmes de statique relatifs à l'Architecture." In: *Mémoires de Mathématiques et de Physiques présentés à l'Académie Royale des Sciences* 7, pp. 343–382.

Cowie, P. A., Sornette, D., and Vanneste, C. (1995). "Multifractal scaling properties of a growing fault population." In: *Geophysical Journal International* 122.2, pp. 457–469. ISSN: 0956540X. DOI: 10.1111/j.1365-246X.1995.tb07007.x.

Crank, J. and Nicolson, P. (1996). "A practical method for numerical evaluation of solutions of partial differential equations of the heat-conduction type." In: *Advances in Computational Mathematics* 6.1, pp. 207–226. ISSN: 1019-7168. DOI: 10.1007/BF02127704.

Cuenot, N., Charléty, J., Dorbath, L., and Haessler, H. (2006). "Faulting mechanisms and stress regime at the European HDR site of Soultz-sous-Forêts, France." In: *Geothermics* 35.5-6, pp. 561–575. ISSN: 03756505. DOI: 10.1016/j.geothermics.2006.11.007.

Cunningham, D., Auradou, H., Shojaei-Zadeh, S., and Drazer, G. (2020). "The Effect of Fracture Roughness on the Onset of Nonlinear Flow." In: *Water Resources Research* 56.11. ISSN: 00431397. DOI: 10.1029/2020WR028049.

Cushman, J. H., Bennethum, L. S., and Hu, B. X. (2002). "A primer on upscaling tools for porous media." In: *Advances in Water Resources* 25.8-12, pp. 1043–1067. ISSN: 03091708. DOI: 10.1016/S0309-1708(02)00047-7.

Cuss, R. J., Rutter, E. H., and Holloway, R. F. (2003). "The application of critical state soil mechanics to the mechanical behaviour of porous sandstones." In: *International Journal of Rock Mechanics and Mining Sciences* 40.6, pp. 847–862. ISSN: 13651609. DOI: 10.1016/S1365-1609(03)00053-4.

Dagan, G., Fiori, A., and Jankovic, I. (2013). "Upscaling of flow in heterogeneous porous formations: Critical examination and issues of principle." In: *Advances in Water Resources* 51, pp. 67–85. ISSN: 03091708. DOI: 10.1016/j.advwatres.2011.12.017.

Darcy, H. (1856). *Les Fontaines de la Ville de Dijon*. Paris: Victor Dalmont.

Dezayes, C., Genter, A., and Valley, B. (2010). "Structure of the low permeable naturally fractured geothermal reservoir at Soultz." In: *Comptes Rendus Geoscience* 342.7-8, pp. 517–530. ISSN: 16310713. DOI: 10.1016/j.crte.2009.10.002.

Diersch, H.-J. and Kolditz, O. (1998). "Coupled groundwater flow and transport: 2. Thermohaline and 3D convection systems." In: *Advances in Water Resources* 21.5, pp. 401–425. ISSN: 03091708. DOI: 10.1016/S0309-1708(97)00003-1.

Dijkstra, E. W. (1959). "A note on two problems in connexion with graphs." In: *Numerische Mathematik* 1.1, pp. 269–271. ISSN: 0029-599X. DOI: 10.1007/BF01386390.

Donath, F. A. and Fruth, L. S. (1971). "Dependence of Strain-Rate Effects on Deformation Mechanism and Rock Type." In: *The Journal of Geology* 79.3, pp. 347–371. ISSN: 0022-1376. DOI: 10.1086/627630.

Dorbath, L., Evans, K., Cuenot, N., Valley, B., Charléty, J., and Frogneux, M. (2010). "The stress field at Soultz-sous-Forêts from focal mechanisms of induced seismic events: Cases of the wells GPK2 and GPK3." In: *Comptes Rendus Geoscience* 342.7-8, pp. 600–606. ISSN: 16310713. DOI: 10.1016/j.crte.2009.12.003.

Dronfield, D. G. and Silliman, S. E. (1993). "Velocity dependence of dispersion for transport through a single fracture of variable roughness." In: *Water Resources Research* 29.10, pp. 3477–3483. ISSN: 00431397. DOI: 10.1029/93WR01407.

Drucker, D. C. and Prager, W. (1952). "Soil mechanics and plastic analysis or limit design." In: *Quarterly of Applied Mathematics* 10.2, pp. 157–165. ISSN: 0033-569X. DOI: 10.1090/qam/48291.

Dunn, D. E., LaFountain, L. J., and Jackson, R. E. (1973). "Porosity dependence and mechanism of brittle fracture in sandstones." In: *Journal of Geophysical Research* 78.14, pp. 2403–2417. ISSN: 0148-0227. DOI: 10.1029/JB078i014p02403.

Dussel, M., Lüschen, E., Thomas, R., Agemar, T., Fritzer, T., Sieblitz, S., Huber, B., Birner, J., and Schulz, R. (2016). "Forecast for thermal water use from Upper Jurassic carbonates in the Munich region (South German Molasse Basin)." In: *Geothermics* 60, pp. 13–30. ISSN: 03756505. DOI: 10.1016/j.geothermics.2015.10.010.

Egert, R., Gholami Korzani, M., Held, S., and Kohl, T. (2020). "Implications on large-scale flow of the fractured EGS reservoir Soultz inferred from hydraulic data and tracer experiments." In: *Geothermics* 84, p. 101749. ISSN: 03756505. DOI: 10.1016/j.geothermics.2019.101749.

Egert, R., Gholami Korzani, M., Held, S., and Kohl, T. (2021a). *Thermo-hydraulic Modeling of an Enhanced Geothermal System in the Upper Rhine Graben using MOOSE/TIGER: PROCEEDINGS World Geothermal Congress 2020+1*. Reykjavik.

Egert, R., Nitschke, F., Gholami Korzani, M., and Kohl, T. (2021b). "Stochastic 3D Navier–Stokes Flow in Self–Affine Fracture Geometries Controlled by Anisotropy and Channeling." In: *Geophysical Research Letters* 48.9. ISSN: 00948276. DOI: 10.1029/2020GL092138.

Egert, R., Seithel, R., Kohl, T., and Stober, I. (2018). "Triaxial testing and hydraulic–mechanical modeling of sandstone reservoir rock in the Upper Rhine Graben." In: *Geothermal Energy* 6.1. ISSN: 2195-9706. DOI: 10.1186/s40517-018-0109-0.

Eisbacher, G. H. and Fielitz, W. (2010). *Karlsruhe und seine Region: Nordschwarzwald, Kraichgau, Neckartal, Oberrhein-Graben, Pfälzerwald und westliche Schwäbische Alb*. Vol. 103. Sammlung geologischer Führer. Stuttgart: Borntraeger. ISBN: 9783443150891.

Elsworth, D. and Goodman, R. E. (1986). "Characterization of rock fissure hydraulic conductivity using idealized wall roughness profiles." In: *International Journal of Rock Mechanics and Mining Sciences & Geomechanics Abstracts* 23.3, pp. 233–243. ISSN: 01489062. DOI: 10.1016/0148-9062(86)90969-1.

Evans, J. P., Forster, C. B., and Goddard, J. V. (1997). "Permeability of fault-related rocks, and implications for hydraulic structure of fault zones." In: *Journal of Structural Geology* 19.11, pp. 1393–1404. ISSN: 01918141. DOI: 10.1016/S0191-8141(97)00057-6.

Evans, K. F. (2005). "Permeability creation and damage due to massive fluid injections into granite at 3.5 km at Soultz: 2. Critical stress and fracture strength." In: *Journal of Geophysical Research* 110.B4. ISSN: 0148-0227. DOI: 10.1029/2004JB003169.

Farmer, C. L. (2002). "Upscaling: a review." In: *International Journal for Numerical Methods in Fluids* 40.1-2, pp. 63–78. ISSN: 0271-2091. DOI: 10.1002/fld.267.

Faulkner, D. R., Jackson, C., Lunn, R. J., Schlische, R. W., Shipton, Z. K., Wibberley, C., and Withjack, M. O. (2010). "A review of recent developments concerning the structure, mechanics and fluid flow properties of fault zones." In: *Journal of Structural Geology* 32.11, pp. 1557–1575. ISSN: 01918141. DOI: 10.1016/j.jsg.2010.06.009.

Figueiredo, B., Tsang, C.-F., Niemi, A., and Lindgren, G. (2016). "Review: The state-of-art of sparse channel models and their applicability to performance assessment of radioactive waste repositories in fractured crystalline formations." In: *Hydrogeology Journal* 24.7, pp. 1607–1622. ISSN: 1431-2174. DOI: 10.1007/s10040-016-1415-x.

Fitch, P. J., Lovell, M. A., Davies, S. J., Pritchard, T., and Harvey, P. K. (2015). "An integrated and quantitative approach to petrophysical heterogeneity." In: *Marine and Petroleum Geology* 63, pp. 82–96. ISSN: 02648172. DOI: 10.1016/j.marpetgeo.2015.02.014.

Fjar, E., Holt, R. M., and Raaen, A. M. (2008). *Petroleum Related Rock Mechanics: 2nd Edition*. 2. Aufl. Vol. 53. Developments in petroleum science. s.l.: Elsevier professional. ISBN: 9780444502605.

Fox, D. B., Sutter, D., Beckers, K. F., Lukawski, M. Z., Koch, D. L., Anderson, B. J., and Tester, J. W. (2013). "Sustainable heat farming: Modeling extraction and recovery in discretely fractured geothermal reservoirs." In: *Geothermics* 46, pp. 42–54. ISSN: 03756505. DOI: 10.1016/j.geothermics.2012.09.001.

Frih, N., Roberts, J. E., and Saada, A. (2008). "Modeling fractures as interfaces: a model for Forchheimer fractures." In: *Computational Geosciences* 12.1, pp. 91–104. ISSN: 1420-0597. DOI: 10.1007/s10596-007-9062-x.

GISTEMP Team (2020). *GISS Surface Temperature Analysis (GISTEMP), version 4 NASA Goddard Institute for Space Studies. Dataset accessed 2020-12-31 at data.giss.nasa.gov/gistemp/.*

Garnish, J. (2002). "European activities in Hot Dry Rock research." In: *Open Meeting on Enhanced Geothermal Systems*, pp. 8–9.

Gaston, D., Newman, C., Hansen, G., and Lebrun-Grandié, D. (2009). "MOOSE: A parallel computational framework for coupled systems of nonlinear equations." In: *Nuclear Engineering and Design* 239.10, pp. 1768–1778. ISSN: 00295493. DOI: 10.1016/j.nucengdes.2009.05.021.

Ge, S. (1997). "A governing equation for fluid flow in rough fractures." In: *Water Resources Research* 33.1, pp. 53–61. ISSN: 00431397. DOI: 10.1029/96WR02588.

Geertsma, J. (1957). "The effect of fluid decline on volumetric changes of porous rocks." In: *Petrol. Trans. AIME* 210, pp. 331–340.

Gelhar, L. W. (1994). *Stochastic subsurface hydrology*. Englewood Cliffs, N.J.: Prentice-Hall. ISBN: 0-13-846767-6.

Gelhar, L. W., Welty, C., and Rehfeldt, K. R. (1992). "A critical review of data on field-scale dispersion in aquifers." In: *Water Resources Research* 28.7, pp. 1955–1974. ISSN: 00431397. DOI: 10.1029/92WR00607.

Gelhar, L. W., Welty, C., and Rehfeldt, K. R. (1993). "Reply [to "Comment on 'A Critical review of data on field-scale dispersion in aquifers' by L. W. Gelhar, C. Welty, and K. R. Rehfeldt"]." In: *Water Resources Research* 29.6, pp. 1867–1869. ISSN: 00431397. DOI: 10.1029/93WR00580.

Genter, A., Baujard, C., Cuenot, N., Dezayes, C., Kohl, T., Masson, F., Sanjuan, B., Scheiber, J., Schill, E., Schmittbuhl, J., and Vidal, J. (2016). *Geology, Geophysics and Geochemistry in the Upper Rhine Graben: the frame for geothermal energy use*. European Geothermal Congress 2016.

Genter, A., Cuenot, N., Goerke, X., Moeckes, W., and Scheiber, J. (2011). *Scientific and technical activity of the Soultz geothermal power plant, Progress report from December 2010 to June 2011: GEIE report RA05 002*.

Genter, A., Evans, K., Cuenot, N., Fritsch, D., and Sanjuan, B. (2010). "Contribution of the exploration of deep crystalline fractured reservoir of Soultz to the knowledge of enhanced geothermal systems (EGS)." In: *Comptes Rendus Geoscience* 342.7-8, pp. 502–516. ISSN: 16310713. DOI: 10.1016/j.crte.2010.01.006.

Gentier, S., Lamontagne, E., Archambault, G., and Riss, J. (1997). "Anisotropy of flow in a fracture undergoing shear and its relationship to the direction of shearing and injection pressure." In: *International Journal of Rock Mechanics and Mining Sciences* 34.3-4. ISSN: 13651609. DOI: 10.1016/S1365-1609(97)00085-3.

Gentier, S., Rachez, X., Ngoc, T. D. T., Peter-Borie, M., and Souque Christine (2010). *3D Flow Modelling of the Medium-Term Circulation Test Performed in the Deep Geothermal Site of Soultz-Sous-forêts (France): PROCEEDINGS World Geothermal Congress 2010*. Bali, Indonesia.

Gentier, S., Rachez, X., Peter-Borie, M., Blaisonneau, A., and Sanjuan, B. (2011). "Transport and Flow Modelling of the Deep Geothermal Exchanger Between Wells at Soultz-sous-Forêts (France)." In: *GRC Transactions* 35, pp. 363–369.

Gérard, A., Genter, A., Kohl, T., Lutz, P., Rose, P., and Rummel, F. (2006). "The deep EGS (Enhanced Geothermal System) project at Soultz-sous-Forêts (Alsace, France)." In: *Geothermics* 35.5-6, pp. 473–483. ISSN: 03756505. DOI: 10.1016/j.geothermics.2006.12.001.

Gerritsen, M. G. and Durlofsky, L. J. (2005). "Modeling fluid flow in oil reservoirs." In: *Annual Review of Fluid Mechanics* 37.1, pp. 211–238. ISSN: 0066-4189. DOI: 10.1146/annurev.fluid.37.061903.175748.

Gessner, K., Kühn, M., Rath, V., Kosack, C., Blumenthal, M., and Clauser, C. (2009). "Coupled Process Models as a Tool for Analysing Hydrothermal Systems." In: *Surveys in Geophysics* 30.3, pp. 133–162. ISSN: 0169-3298. DOI: 10.1007/s10712-009-9067-1.

Geuzaine, C. and Remacle, J.-F. (2017). *Gmsh Reference Manual: The documentation for Gmsh 2.16*.

Ghergut, I., Behrens, H., Sauter, M., Licha, T., and Nottebohm, M. (2013). *Can Peclet numbers depend on tracer species? going beyond SW test insensitivity to advective or equilibrium-exchange processes. PROCEEDINGS Thirty-Eighth Workshop on Geothermal Reservoir Engineering*. Stanford, California.

Ghergut, J., Behrens, H., Bansabat, J., Sauter, M., Wagner, B., and Wiegand, B. (2018). *Sorption, matrix diffusion, ... need not make a major difference for frac characterization from short-term tracer signals: PROCEEDINGS 43rd Workshop on Geothermal Reservoir Engineering*. Stanford, California.

Ghergut, J., Behrens, H., and Sauter, M. (2016). "Petrothermal and aquifer-based EGS in the Northern-German Sedimentary Basin, investigated by conservative tracers during single-well injection-flowback and production tests." In: *Geothermics* 63, pp. 225–241. ISSN: 03756505. DOI: 10.1016/j.geothermics.2016.01.015.

Gholami Korzani, M., Held, S., and Kohl, T. (2020). "Numerical based filtering concept for feasibility evaluation and reservoir performance enhancement of hydrothermal doublet systems." In: *Journal of Petroleum Science and Engineering* 190, p. 106803. ISSN: 09204105. DOI: 10.1016/j.petrol.2019.106803.

Grimmer, J. C., Ritter, J. R. R., Eisbacher, G. H., and Fielitz, W. (2017). "The Late Variscan control on the location and asymmetry of the Upper Rhine Graben." In: *International Journal of Earth Sciences* 106.3, pp. 827–853. ISSN: 1437-3254. DOI: 10.1007/s00531-016-1336-x.

Guéguen, Y., Le Ravalec, M., and Ricard, L. (2006). "Upscaling: Effective Medium Theory, Numerical Methods and the Fractal Dream." In: *Pure and Applied Geophysics* 163.5-6, pp. 1175–1192. ISSN: 0033-4553. DOI: 10.1007/s00024-006-0053-y.

Guéguen, Y. and Boutéca, M. (2004). *Mechanics of fluid saturated rocks*. Vol. v. 89. International geophysics series. Amsterdam and Boston: Elsevier Academic Press. ISBN: 9780080479361.

Guihéneuf, N., Bour, O., Boisson, A., Le Borgne, T., Becker, M. W., Nigon, B., Wajiduddin, M., Ahmed, S., and Maréchal, J.-C. (2017). "Insights about transport mechanisms and fracture flow channeling from multi-scale observations of tracer dispersion in shallow fractured crystalline rock." In: *Journal of Contaminant Hydrology* 206, pp. 18–33. ISSN: 01697722. DOI: 10.1016/j.jconhyd.2017.09.003.

Guillou-Frottier, L., Carrė, C., Bourgine, B., Bouchot, V., and Genter, A. (2013). "Structure of hydrothermal convection in the Upper Rhine Graben as inferred from corrected temperature data and basin-scale numerical models." In: *Journal of Volcanology and Geothermal Research* 256, pp. 29–49. ISSN: 03770273. DOI: 10.1016/j.jvolgeores.2013.02.008.

Guimerà, J., Vives, L., and Carrera, J. (1995). "A discussion of scale effects on hydraulic conductivity at a granitic site (El Berrocal, Spain)." In: *Geophysical Research Letters* 22.11, pp. 1449–1452. ISSN: 00948276. DOI: 10.1029/95GL01493.

Guo, B., Fu, P., Hao, Y., Peters, C. A., and Carrigan, C. R. (2016). "Thermal drawdown-induced flow channeling in a single fracture in EGS." In: *Geothermics* 61, pp. 46–62. ISSN: 03756505. DOI: 10.1016/j.geothermics.2016.01.004.

Hadermann, J. and Heer, W. (1996). "The Grimsel (Switzerland) migration experiment: integrating field experiments, laboratory investigations and modelling." In: *Journal of Contaminant Hydrology* 21.1-4, pp. 87–100. ISSN: 01697722. DOI: 10.1016/0169-7722(95)00035-6.

Han, G. and Dusseault, M. B. (2003). "Description of fluid flow around a wellbore with stress-dependent porosity and permeability." In: *Journal of Petroleum Science and Engineering* 40.1-2, pp. 1–16. ISSN: 09204105. DOI: 10.1016/S0920-4105(03)00047-0.

Hanor, J. S. (1993). "Effective hydraulic conductivity of fractured clay beds at a hazardous waste landfill, Louisiana Gulf Coast." In: *Water Resources Research* 29.11, pp. 3691–3698. ISSN: 00431397. DOI: 10.1029/93WR01913.

Hassanzadegan, A. and Zimmermann, G. (2014). "A Poroelastic Description of Permeability Evolution." In: *Pure and Applied Geophysics* 171.7, pp. 1187–1201. ISSN: 0033-4553. DOI: 10.1007/s00024-013-0714-6.

Held, S., Genter, A., Kohl, T., Kölbel, T., Sausse, J., and Schoenball, M. (2014). "Economic evaluation of geothermal reservoir performance through modeling the complexity of the operating EGS in Soultz-sous-Forêts." In: *Geothermics* 51, pp. 270–280. ISSN: 03756505. DOI: 10.1016/j.geothermics.2014.01.016.

Hettkamp, T., Fuhrmann, G., and Rummel, F. (1999). "Hydraulic properties of the Rheingraben basement material." In: *Bulletin d'Hydrogiologie No 17*.

Heuze, F. E. (1980). "Scale effects in the determination of rock mass strength and deformability." In: *Rock Mechanics Felsmechanik Mecanique des Roches* 12.3-4, pp. 167–192. ISSN: 0035-7448. DOI: 10.1007/BF01251024.

Hooijkaas, G. R., Genter, A., and Dezayes, C. (2006). "Deep-seated geology of the granite intrusions at the Soultz EGS site based on data from 5km-deep boreholes." In: *Geothermics* 35.5-6, pp. 484–506. ISSN: 03756505. DOI: 10.1016/j.geothermics.2006.03.003.

Horne, R. N. and Rodriguez, F. (1983). "Dispersion in tracer flow in fractured geothermal systems." In: *Geophysical Research Letters* 10.4, pp. 289–292. ISSN: 00948276. DOI: 10.1029/GL010i004p00289.

Hornung, U. (1997). *Homogenization and porous media*. Vol. 6. Interdisciplinary applied mathematics. New York: Springer. ISBN: 978-1-4612-1920-0.

Hou, T. Y. and Wu, X.-H. (1997). "A Multiscale Finite Element Method for Elliptic Problems in Composite Materials and Porous Media." In: *Journal of Computational Physics* 134.1, pp. 169–189. ISSN: 00219991. DOI: 10.1006/jcph.1997.5682.

Hsieh, P. A. (1998). "Scale effects in fluid flow through fractured geologic media." In: *Scale Dependence and Scale Invariance in Hydrology*. Ed. by G. Sposito. Cambridge: Cambridge University Press, pp. 335–353.

Hsieh, P. A., Neuman, S. P., Stiles, G. K., and Simpson, E. S. (1985). "Field Determination of the Three-Dimensional Hydraulic Conductivity Tensor of Anisotropic Media: 2. Methodology and Application to Fractured Rocks." In: *Water Resources Research* 21.11, pp. 1667–1676. ISSN: 00431397. DOI: 10.1029/WR021i011p01667.

Huenges, E. (2016). "Enhanced geothermal systems." In: *Geothermal Power Generation*. Elsevier, pp. 743–761. ISBN: 9780081003374. DOI: 10.1016/b978-0-08-100337-4.00025-5.

Hughes, T. J., Franca, L. P., and Balestra, M. (1986). "A new finite element formulation for computational fluid dynamics: V. Circumventing the babuška-brezzi condition: a stable Petrov-Galerkin formulation of the stokes problem accommodating equal-order interpolations." In: *Computer Methods in Applied Mechanics and Engineering* 59.1, pp. 85–99. ISSN: 00457825. DOI: 10.1016/0045-7825(86)90025-3.

IEA (2017). *Energy Technology Perspectives 2017*.

IEA, ed. (2019). *Geothermal Power Statistics 2017*.

IPCC, ed. (2018). *Global warming of 1.5°C*.

Icardi, M., Boccardo, G., and Dentz, M. (2019). "Upscaling Flow and Transport Processes." In: *Flowing Matter*. Ed. by F. Toschi and M. Sega. Soft and Biological Matter. Cham: Springer International Publishing and Imprint, Springer, pp. 137–176. ISBN: 978-3-030-23370-9. DOI: 10.1007/978-3-030-23370-95.

Iglesias, E. R., Flores-Armenta, M., Torres, R. J., Ramirez-Montez, M., Reyes-Picaso, N., and Cruz-Grajales, I. (2015). *Tracer Testing at Los Humeros, Mexico, High-Enthalpy Geothermal Field: PROCEEDINGS World Geothermal Congress 2015*. Melbourne.

Illies, J. H. (1965). "Bauplan und Baugeschichte des Oberrheingrabens." In: *Oberrhein. Geol. Abh.* 14.1/2, pp. 1–54.

Illies, J. H. (1972). "The Rhine graben rift system-plate tectonics and transform faulting." In: *Geophysical Surveys* 1.1, pp. 27–60. ISSN: 0046-5763. DOI: 10.1007/BF01449550.

Illman, W. A. (2006). "Strong field evidence of directional permeability scale effect in fractured rock." In: *Journal of Hydrology* 319.1-4, pp. 227–236. ISSN: 00221694. DOI: 10.1016/j.jhydrol.2005.06.032.

Istok, J. (1989). *Groundwater Modeling by the Finite Element Method*. Vol. 13. Washington, D. C.: American Geophysical Union. ISBN: 0-87590-317-7. DOI: 10.1029/WM013.

Jackson, C. P., Hoch, A. R., and Todman, S. (2000). "Self-consistency of a heterogeneous continuum porous medium representation of a fractured medium." In: *Water Resources Research* 36.1, pp. 189–202. ISSN: 00431397. DOI: 10.1029/1999WR900249.

Jacquey, A. B., Cacace, M., Blöcher, G., Watanabe, N., Huenges, E., and Scheck-Wenderoth, M. (2016). "Thermo-poroelastic numerical modelling for enhanced geothermal system performance: Case study of the Groß Schönebeck reservoir." In: *Tectonophysics* 684, pp. 119–130. ISSN: 00401951. DOI: 10.1016/j.tecto.2015.12.020.

Jacquey, A. B., Cacace, M., Blöcher, G., Watanabe, N., and Scheck-Wenderoth, M. (2015). "Hydro-Mechanical Evolution of Transport Properties in Porous Media: Constraints for Numerical Simulations." In: *Transport in Porous Media* 110.3, pp. 409–428. ISSN: 0169-3913. DOI: 10.1007/s11242-015-0564-z.

Jaeger, J. C., Cook, N. G. W., and Zimmerman, R. W. (2007). *Fundamentals of rock mechanics*. 4. ed. Malden Mass.: Blackwell Publ. ISBN: 0-632-05759-9.

Javadi, M., Sharifzadeh, M., and Shahriar, K. (2010). "A new geometrical model for non-linear fluid flow through rough fractures." In: *Journal of Hydrology* 389.1-2, pp. 18–30. ISSN: 00221694. DOI: 10.1016/j.jhydrol.2010.05.010.

Javadi, M., Sharifzadeh, M., Shahriar, K., and Mitani, Y. (2014). "Critical Reynolds number for nonlinear flow through rough-walled fractures: The role of shear processes." In: *Water Resources Research* 50.2, pp. 1789–1804. ISSN: 00431397. DOI: 10.1002/2013WR014610.

Jodocy, M. and Stober, I. (2010). "Geologisch-geothermische Tiefenprofile für den baden-württembergischen Teil des nördlichen und mittleren Oberrheingrabens." In: *Erdöl Erdgas Kohle 126* 2, pp. 68–76.

Johnson, W., Baraya, G. L., and Slater, R. (1964). "On heat lines or lines of thermal discontinuity." In: *International Journal of Mechanical Sciences* 6.6, 409–IN4. ISSN: 00207403. DOI: 10.1016/S0020-7403(64)80001-1.

Jung, R. (2013). "EGS — Goodbye or Back to the Future 95." In: *Effective and Sustainable Hydraulic Fracturing*. Ed. by R. Jeffrey. InTech. ISBN: 978-953-51-1137-5. DOI: 10.5772/56458.

Jung, R., Schindler, M., Nami, P., and Tischner, T. (2010). "Determination of flow exits in the Soultz borehole GPK2 by using the brine displacement method." In: *Comptes Rendus Geoscience* 342.7-8, pp. 636–643. ISSN: 16310713. DOI: 10.1016/j.crte.2009.06.002.

Karmakar, S., Ghergut, J., and Sauter, M. (2016). "Early-flowback tracer signals for fracture characterization in an EGS developed in deep crystalline and sedimentary formations: a parametric study." In: *Geothermics* 63, pp. 242–252. ISSN: 03756505. DOI: 10.1016/j.geothermics.2015.08.007.

Kestin, J., Khalifa, H. E., and Correia, R. J. (1981). "Tables of the dynamic and kinematic viscosity of aqueous KCl solutions in the temperature range 25–150 °C and the pressure range 0.1–35 MPa." In: *Journal of Physical and Chemical Reference Data* 10.1, pp. 57–70. ISSN: 0047-2689. DOI: 10.1063/1.555640.

Khajeh, M. M. (2013). *Heterogeneity Consideration and Upscaling of Elastic Properties in Coupled Geomechanical Flow Simulation of SAGD. Dissertation*. University of Alberta, Kanada.

Khan, A. S., Xiang, Y., and Huang, S. (1991). "Behavior of Berea sandstone under confining pressure part I: Yield and failure surfaces, and nonlinear elastic response." In: *International Journal of Plasticity* 7.6, pp. 607–624. ISSN: 07496419. DOI: 10.1016/0749-6419(91)90046-2.

Khoei, A. R. (2015). *Extended finite element method: Theory and applications*. Chichester, West Sussex: John Wiley & Sons, Inc. ISBN: 978-1-118-86968-0.

Kiraly, L. (1975). "Rapport sur l' etat actuel des connaissances dans le domaines des caracte' res physiques des roches karstiques." In: *Hydrogeology of Karstic Terrains, Int. Union of Geological Sciences, Ser. B*, 3, pp. 53–67.

Kirk, B. S., Peterson, J. W., Stogner, R. H., and Carey, G. F. (2006). "libMesh : a C++ library for parallel adaptive mesh refinement/coarsening simulations." In: *Engineering with Computers* 22.3-4, pp. 237–254. ISSN: 0177-0667. DOI: 10.1007/s00366-006-0049-3.

Klepikova, M. V., Le Borgne, T., Bour, O., Dentz, M., Hochreutener, R., and Lavenant, N. (2016). "Heat as a tracer for understanding transport processes in fractured media: Theory and field assessment from multiscale thermal push-pull tracer tests." In: *Water Resources Research* 52.7, pp. 5442–5457. ISSN: 00431397. DOI: 10.1002/2016WR018789.

Klepikova, M., Brixel, B., and Jalali, M. (2020). "Transient hydraulic tomography approach to characterize main flowpaths and their connectivity in fractured media." In: *Advances in Water Resources* 136, p. 103500. ISSN: 03091708. DOI: 10.1016/j.advwatres.2019.103500.

Knudby, C. and Carrera, J. (2005). "On the relationship between indicators of geostatistical, flow and transport connectivity." In: *Advances in Water Resources* 28.4, pp. 405–421. ISSN: 03091708. DOI: 10.1016/j.advwatres.2004.09.001.

Kohl, T., Evans, K. F., Hopkirk, R. J., Jung, R., and Rybach, L. (1997). "Observation and simulation of non-Darcian flow transients in fractured rock." In: *Water Resources Research* 33.3, pp. 407–418. ISSN: 00431397. DOI: 10.1029/96WR03495.

Kohl, T., Bächler, D., and Rybach, L. (2000). *Steps towards a comprehensive thermo-hydraulic analysis of the HDR test site Soultz-sous-Forêts: PROCEEDINGS World Geothermal Congress 2000*, pp. 3459–3464.

Kohl, T., Baujard, C., and Mégel, T. (2006). "Conditions for mechanical re-stimulation of GPK4." In: *Paper presented at EHDRA Scientific Conference, 15-16 June 2006*.

Kohl, T., Evans, K. F., Hopkirk, R. J., Jung, R., and Rybach, L. (1995). *Modelling of turbulent flow transients within Hot Dry Rock fracture systems: Preliminary results: PROCEEDINGS World Geothermal Congress 1995*. Florence, Italy.

Kohl, T. and Mégel, T. (2007). "Predictive modeling of reservoir response to hydraulic stimulations at the European EGS site Soultz-sous-Forêts." In: *International Journal of Rock Mechanics and Mining Sciences* 44.8, pp. 1118–1131. ISSN: 13651609. DOI: 10.1016/j.ijrmms.2007.07.022.

Kolditz, O., Shao, H., Wang, W., and Bauer, S., eds. (2015). *Thermo-Hydro-Mechanical-Chemical Processes in Fractured Porous Media: Modelling and Bench-*

marking: Closed-Form Solutions. Cham: Springer International Publishing. ISBN: 978-3-319-11893-2.

Konzuk, J. S. and Kueper, B. H. (2004). "Evaluation of cubic law based models describing single-phase flow through a rough-walled fracture." In: *Water Resources Research* 40.2, p. 1. ISSN: 00431397. DOI: 10.1029/2003WR002356.

Kosack, C., Vogt, C., Rath, V., and Marquart, G. (2011). *Stochastic Estimates of the Permeability Field of the Soultz-sous-Forêts Geothermal Reservoir - Comparison of Bayesian Inversion, MC Geostatistics, and EnKF Assimilation: PROCEEDINGS Thirty-Sixth Workshop on Geothermal Reservoir Engineering*. Stanford, California.

Koyama, T., Fardin, N., Jing, L., and Stephansson, O. (2006). "Numerical simulation of shear-induced flow anisotropy and scale-dependent aperture and transmissivity evolution of rock fracture replicas." In: *International Journal of Rock Mechanics and Mining Sciences* 43.1, pp. 89–106. ISSN: 13651609. DOI: 10.1016/j.ijrmms.2005.04.006.

Krietsch, H. (2014). *Analysis of fracture topographies of deformed rocks using white light interferometry. Master thesis*. Freiburg: Albert-Ludwigs-University.

Lama, R. D. and Vutukuri, V. S. (1978). *Handbook on mechanical properties of rocks: Testing techniques and results*. 1. print. Vol. 2, No. 1. Clausthal: Trans Tech Publications. ISBN: 0878490213.

Lang, P. S., Paluszny, A., Nejati, M., and Zimmerman, R. W. (2018). "Relationship Between the Orientation of Maximum Permeability and Intermediate Principal Stress in Fractured Rocks." In: *Water Resources Research* 54.11, pp. 8734–8755. ISSN: 00431397. DOI: 10.1029/2018WR023189.

Le Goc, R., Dreuzy, J.-R. de, and Davy, P. (2010). "An inverse problem methodology to identify flow channels in fractured media using synthetic steady-state head and geometrical data." In: *Advances in Water Resources* 33.7, pp. 782–800. ISSN: 03091708. DOI: 10.1016/j.advwatres.2010.04.011.

Levenspiel, O. (1972). *Chemical reaction engineering*. 2. ed. New York: Wiley. ISBN: 0471530190.

Li, B., Liu, R., and Jiang, Y. (2016). "Influences of hydraulic gradient, surface roughness, intersecting angle, and scale effect on nonlinear flow behavior at single fracture intersections." In: *Journal of Hydrology* 538, pp. 440–453. ISSN: 00221694. DOI: 10.1016/j.jhydrol.2016.04.053.

Li, L., Steefel, C. I., and Yang, L. (2008). "Scale dependence of mineral dissolution rates within single pores and fractures." In: *Geochimica et Cosmochimica Acta* 72.2, pp. 360–377. ISSN: 00167037. DOI: 10.1016/j.gca.2007.10.027.

Li, X. S. and Demmel, J. W. (2003). "SuperLU_DIST." In: *ACM Transactions on Mathematical Software* 29.2, pp. 110–140. ISSN: 0098-3500. DOI: 10.1145/779359.779361.

Liu, R., Li, B., Jiang, Y., and Huang, N. (2016). "Review: Mathematical expressions for estimating equivalent permeability of rock fracture networks." In: *Hydrogeology Journal* 24.7, pp. 1623–1649. ISSN: 1431-2174. DOI: 10.1007/s10040-016-1441-8.

Liu, R., Wang, C., Li, B., Jiang, Y., and Jing, H. (2020). "Modeling linear and nonlinear fluid flow through sheared rough-walled joints taking into account boundary stiffness." In: *Computers and Geotechnics* 120, p. 103452. ISSN: 0266352X. DOI: 10.1016/j.compgeo.2020.103452.

Lloyd, J. W., Greswell, R., Williams, G. M., Ward, R. S., Mackay, R., and Riley, M. (1996). "An integrated study of controls on solute transport in the Lincolnshire limestone." In: *Quarterly Journal of Engineering Geology and Hydrogeology* 29.4, pp. 321–339. ISSN: 1470-9236. DOI: 10.1144/GSL.QJEGH.1996.029.P4.06.

Louis, C. (1967). "Strömungsvorgänge in klüftigen Medien und ihre Wirkung auf die Standsicherheit von Bauwerken und Böschungen im Fels." In: *Veröffentlichung des Institutes für Bodenmechanik und Felsmechanik* 30.

Lukaszewicz, G. and Kalita, P. (2016). *Navier-Stokes Equations: An Introduction with Applications*. Advances in Mechanics and Mathematics. Cham: Springer International Publishing, Imprint, and Springer. ISBN: 9783319277585.

Maillot, J., Davy, P., Le Goc, R., Darcel, C., and Dreuzy, J. R. de (2016). "Connectivity, permeability, and channeling in randomly distributed and kinematically defined discrete fracture network models." In: *Water Resources Research* 52.11, pp. 8526–8545. ISSN: 00431397. DOI: 10.1002/2016WR018973.

Mallikamas, W. and Rajaram, H. (2005). "On the anisotropy of the aperture correlation and effective transmissivity in fractures generated by sliding between identical self-affine surfaces." In: *Geophysical Research Letters* 32.11. ISSN: 00948276. DOI: 10.1029/2005GL022859.

Mandelbrot, B. B. (1982). *The fractals geometry of nature*. Updated and augmented. Vol. 173. Einaudi paperbacks. San Francisco, Calif.: Freeman. ISBN: 0716711869.

Mansfield, C. S. and Cartwright, J. A. (1996). "High resolution fault displacement mapping from three-dimensional seismic data: evidence for dip linkage during fault growth." In: *Journal of Structural Geology* 18.2-3, pp. 249–263. ISSN: 01918141. DOI: 10.1016/S0191-8141(96)80048-4.

Marchand, S., Mersch, O., Selzer, M., Nitschke, F., Schoenball, M., Schmittbuhl, J., Nestler, B., and Kohl, T. (2020). "A Stochastic Study of Flow Anisotropy and Channelling in Open Rough Fractures." In: *Rock Mechanics Felsmechanik Mecanique des Roches* 53.1, pp. 233–249. ISSN: 0035-7448. DOI: 10.1007/s00603-019-01907-4.

Martinez-Landa, L. and Carrera, J. (2005). "An analysis of hydraulic conductivity scale effects in granite (Full-scale Engineered Barrier Experiment (FEBEX), Grimsel, Switzerland)." In: *Water Resources Research* 41.3. ISSN: 00431397. DOI: 10.1029/2004WR003458.

Mégel, T., Kohl, T., Gérard, A., Rybach, L., and Hopkirk, R. (2005). *Downhole Pressures Derived from Wellhead Measurements during Hydraulic Experiments: PROCEEDINGS World Geothermal Congress 2005*. Antalya, Turkey.

Méheust, Y. and Schmittbuhl, J. (2001). "Geometrical heterogeneities and permeability anisotropy of rough fractures." In: *Journal of Geophysical Research: Solid Earth* 106.B2, pp. 2089–2102. ISSN: 01480227. DOI: 10.1029/2000JB900306.

Méheust, Y. and Schmittbuhl, J. (2003). "Scale Effects Related to Flow in Rough Fractures." In: *Pure and Applied Geophysics* 160.5-6, pp. 1023–1050. ISSN: 0033-4553. DOI: 10.1007/PL00012559.

Meixner, J. (2016). *Geomechanical characterization of geothermal relevant fault patterns in Southwest Germany: Dissertation*. Karlsruhe.

Meixner, J., Schill, E., Gaucher, E., and Kohl, T. (2014). "Inferring the in situ stress regime in deep sediments: An example from the Bruchsal geothermal site." In: *Geothermal Energy* 2.1. ISSN: 2195-9706. DOI: 10.1186/s40517-014-0007-z.

Meller, C., Genter, A., and Kohl, T. (2014). "The application of a neural network to map clay zones in crystalline rock." In: *Geophysical Journal International* 196.2, pp. 837–849. ISSN: 0956540X. DOI: 10.1093/GJI/GGT423.

Moreno, L., Tsang, Y. W., Tsang, C. F., Hale, F. V., and Neretnieks, I. (1988). "Flow and tracer transport in a single fracture: A stochastic model and its relation to some field observations." In: *Water Resources Research* 24.12, pp. 2033–2048. ISSN: 00431397. DOI: 10.1029/WR024i012p02033.

Moreno, L. and Tsang, C.-F. (1994). "Flow channeling in strongly heterogeneous porous media: A numerical study." In: *Water Resources Research* 30.5, pp. 1421–1430. ISSN: 00431397. DOI: 10.1029/93WR02978.

Mouchot, J., Genter, A., Cuenot, N., Scheiber, J., Seibel, O., Bosia, C., and Ravier, G. (2018). *First Year of Operation from EGS geothermal Plants in Alsace, France: Scaling Issues: PROCEEDINGS 43rd Workshop on Geothermal Reservoir Engineering*. Stanford, California.

Murphy, H. D., Tester, J. W., Grigsby, C. O., and Potter, R. M. (1981). "Energy extraction from fractured geothermal reservoirs in low-permeability crystalline rock." In: *Journal of Geophysical Research* 86.B8, p. 7145. ISSN: 0148-0227. DOI: 10.1029/JB086iB08p07145.

Nami, P., Schellschmidt, R., Schindler, M., and Tischner, T. (2008). *Chemical stimulation operations for reservoir development of the deep crystalline HDR/EGS system at Soultz-sous-Forêts (France): PROCEEDINGS Thirty-Second Workshop on Geothermal Reservoir Engineering*. Stanford, California.

Neuman, S. P. (1994). "Generalized scaling of permeabilities: Validation and effect of support scale." In: *Geophysical Research Letters* 21.5, pp. 349–352. ISSN: 00948276. DOI: 10.1029/94GL00308.

Nicholl, M. J., Rajaram, H., Glass, R. J., and Detwiler, R. (1999). "Saturated flow in a single fracture: evaluation of the Reynolds Equation in measured aperture fields." In: *Water Resources Research* 35.11, pp. 3361–3373. ISSN: 00431397. DOI: 10.1029/1999WR900241.

Nitschke, F. (2017). "Numerical and Experimental Characterization of Dissolution and Precipitation Processes in Deep Geothermal Reservoirs." Dissertation. Karlsruhe: Karlsruhe Institute of Technology.

Nusiaputra, Y. Y. (2017). "Coupled Hydraulic, Thermal and Chemical Simulations for Geothermal Installations." Dissertation. Karlsruhe: Karlsruhe Institute of Technology. DOI: 10.5445/IR/1000068708.

O'Sullivan, M. J. and O'Sullivan, J. P. (2016). "Reservoir modeling and simulation for geothermal resource characterization and evaluation." In: *Geothermal Power Generation*. Elsevier, pp. 165–199. ISBN: 9780081003374. DOI: 10.1016/B978-0-08-100337-4.00007-3.

O'Sullivan, M. J., Pruess, K., and Lippmann, M. J. (2001). "State of the art of geothermal reservoir simulation." In: *Geothermics* 30.4, pp. 395–429. ISSN: 03756505. DOI: 10.1016/S0375-6505(01)00005-0.

Palchik, V. (1999). "Influence of Porosity and Elastic Modulus on Uniaxial Compressive Strength in Soft Brittle Porous Sandstones." In: *Rock Mechanics and Rock Engineering* 32.4, pp. 303–309. ISSN: 0723-2632. DOI: 10.1007/s006030050050.

Panfilov, M. (2000). *Macroscale Models of Flow Through Highly Heterogeneous Porous Media*. Vol. 16. Theory and Applications of Transport in Porous Media. Dordrecht: Springer Netherlands. ISBN: 978-94-015-9582-7.

Pape, H., Clauser, C., and Iffland, J. (2000). "Variation of Permeability with Porosity in Sandstone Diagenesis Interpreted with a Fractal Pore Space Model." In: *Pure and Applied Geophysics* 157.4, pp. 603–619. ISSN: 0033-4553. DOI: 10.1007/PL00001110.

Peng, D.-Y. and Robinson, D. B. (1976). "A New Two-Constant Equation of State." In: *Industrial & Engineering Chemistry Fundamentals* 15.1, pp. 59–64. ISSN: 0196-4313. DOI: 10.1021/i160057a011.

Permann, C. J., Gaston, D. R., Andrš, D., Carlsen, R. W., Kong, F., Lindsay, A. D., Miller, J. M., Peterson, J. W., Slaughter, A. E., Stogner, R. H., and Martineau, R. C. (2020). "MOOSE: Enabling massively parallel multiphysics simulation." In: *SoftwareX* 11. ISSN: 23527110. DOI: 10.1016/j.softx.2020.100430.

Perzyna, P. (1966). "Fundamental Problems in Viscoplasticity." In: *Advances in applied mechanics*. Ed. by G. G. Chernyi. Vol. 9. Advances in Applied Mechanics. New York: Academic Press, pp. 243–377. ISBN: 9780120020096. DOI: 10.1016/S0065-2156(08)70009-7.

Peterson, J. W., Lindsay, A. D., and Kong, F. (2018). "Overview of the incompressible Navier–Stokes simulation capabilities in the MOOSE framework." In: *Advances in Engineering Software* 119, pp. 68–92. ISSN: 09659978. DOI: 10.1016/j.advengsoft.2018.02.004.

Pfender, M., Nami, P., Tischner, T., and Jung, R. (2006). "Status of the Soultz deep wells based on low rate hydraulic tests and temperature logs." In: *EHDRA Scientific Conference 15.-16.06*.

Pflug, R. (1982). *Bau und Entwicklung des Oberrheingrabens.* Darmstadt: Wissenschaftliche Buchgesellschaft.

Philipp, S. L., Reyer, D., Meier, S., Hemes, S., Hoffmann, S., Lunsdorf, N. K., and Oelrich, A. (2008). "Strukturgeologische Gelandestudien in Aufschlussanalogen und Permeabilitatsentwicklung in geothermischen Reservoiren." In: *Geotectonic Research* 95.0, pp. 137–139. ISSN: 1864-5658. DOI: 10.1127/1864-5658/08/9501-0137.

Place, J., Sausse, J., Marthelot, J.-M., Diraison, M., Géraud, Y., and Naville, C. (2011). "3-D mapping of permeable structures affecting a deep granite basement using isotropic 3C VSP data." In: *Geophysical Journal International* 186.1, pp. 245–263. ISSN: 0956540X. DOI: 10.1111/j.1365-246X.2011.05012.x.

Plenefisch, T. and Bonjer, K.-P. (1997). "The stress field in the Rhine Graben area inferred from earthquake focal mechanisms and estimation of frictional parameters." In: *Tectonophysics* 275.1-3, pp. 71–97. ISSN: 00401951. DOI: 10.1016/S0040-1951(97)00016-4.

Poulet, T., Paesold, M., and Veveakis, M. (2017). "Multi-Physics Modelling of Fault Mechanics Using REDBACK: A Parallel Open-Source Simulator for Tightly Coupled Problems." In: *Rock Mechanics and Rock Engineering* 50.3, pp. 733–749. ISSN: 0723-2632. DOI: 10.1007/s00603-016-0927-y.

Poulet, T. and Veveakis, M. (2016). "A viscoplastic approach for pore collapse in saturated soft rocks using REDBACK: An open-source parallel simulator for

Rock mEchanics with Dissipative feedBACKs." In: *Computers and Geotechnics* 74, pp. 211–221. ISSN: 0266352X. DOI: 10.1016/j.compgeo.2015.12.015.

Pribnow, D. and Schellschmidt, R. (2000). "Thermal tracking of upper crustal fluid flow in the Rhine graben." In: *Geophysical Research Letters* 27.13, pp. 1957–1960. ISSN: 00948276. DOI: 10.1029/2000GL008494.

Pruess, K. (1990). "Modeling of geothermal reservoirs: Fundamental processes, computer simulation and field applications." In: *Geothermics* 19.1, pp. 3–15. ISSN: 03756505. DOI: 10.1016/0375-6505(90)90062-G.

Qian, J., Zhan, H., Luo, S., and Zhao, W. (2007). "Experimental evidence of scale-dependent hydraulic conductivity for fully developed turbulent flow in a single fracture." In: *Journal of Hydrology* 339.3-4, pp. 206–215. ISSN: 00221694. DOI: 10.1016/j.jhydrol.2007.03.015.

Radilla, G., Sausse, J., Sanjuan, B., and Fourar, M. (2012). "Interpreting tracer tests in the enhanced geothermal system (EGS) of Soultz-sous-Forêts using the equivalent stratified medium approach." In: *Geothermics* 44, pp. 43–51. ISSN: 03756505. DOI: 10.1016/j.geothermics.2012.07.001.

Ramey, H., Brigham, W., Chen, H., Atkinson, P., and Arihara, N. (1974). "Thermodynamic and hydrodynamic properties of hydrothermal systems." In: *Proceedings of the NSF Conference on the Utilization of Volcano Energy, 4–8 February 1974, Hilo, HI*, pp. 509–587.

Ranjith, P. G., Viete, D. R., Chen, B. J., and Perera, M. S. A. (2012). "Transformation plasticity and the effect of temperature on the mechanical behaviour of Hawkesbury sandstone at atmospheric pressure." In: *Engineering Geology* 151, pp. 120–127. ISSN: 00137952. DOI: 10.1016/j.enggeo.2012.09.007.

Rasmuson, A. and Neretnieks, I. (1986). "Radionuclide Transport in Fast Channels in Crystalline Rock." In: *Water Resources Research* 22.8, pp. 1247–1256. ISSN: 00431397. DOI: 10.1029/WR022i008p01247.

Redlich, O. and Kwong, J. N. S. (1949). "On the thermodynamics of solutions; an equation of state; fugacities of gaseous solutions." In: *Chemical reviews* 44.1, pp. 233–244. ISSN: 0009-2665. DOI: 10.1021/cr60137a013.

Renard, P. and Allard, D. (2013). "Connectivity metrics for subsurface flow and transport." In: *Advances in Water Resources* 51, pp. 168–196. ISSN: 03091708. DOI: 10.1016/j.advwatres.2011.12.001.

Robinson, B. A. and Tester, J. W. (1984). "Dispersed fluid flow in fractured reservoirs: An analysis of tracer-determined residence time distributions." In: *Journal of Geophysical Research: Solid Earth* 89.B12, pp. 10374–10384. ISSN: 21699313. DOI: 10.1029/JB089iB12p10374.

Ronayne, M. J., Gorelick, S. M., and Caers, J. (2008). "Identifying discrete geologic structures that produce anomalous hydraulic response: An inverse modeling approach." In: *Water Resources Research* 44.8. ISSN: 00431397. DOI: 10.1029/2007WR006635.

Rose, P., Leecaster, K., Drakos, P., and Robertson-Tait, A. (2009). "Tracer Testing at the Desert Peak EGS Project." In: *GRC Transactions* 33, pp. 241–249.

Rovey, C. W. and Cherkauer, D. S. (1995). "Scale Dependency of Hydraulic Conductivity Measurements." In: *Ground water* 33.5, pp. 769–780. DOI: 10.1111/j.1745-6584.1995.tb00023.x.

Rudnicki, J. W. (2004). "Shear and compaction band formation on an elliptic yield cap." In: *Journal of Geophysical Research* 109.B3, p. 355. ISSN: 0148-0227. DOI: 10.1029/2003JB002633.

Rutqvist, J., Wu, Y.-S., Tsang, C.-F., and Bodvarsson, G. (2002). "A modeling approach for analysis of coupled multiphase fluid flow, heat transfer, and deformation in fractured porous rock." In: *International Journal of Rock Mechanics and Mining Sciences* 39.4, pp. 429–442. ISSN: 13651609. DOI: 10.1016/S1365-1609(02)00022-9.

Rutter, E. H. and Glover, C. T. (2012). "The deformation of porous sandstones; are Byerlee friction and the critical state line equivalent?" In: *Journal of Structural Geology* 44, pp. 129–140. ISSN: 01918141. DOI: 10.1016/j.jsg.2012.08.014.

Sanjuan, B., Brach, M., Genter, A., Sanjuan, R., Scheiber, J., and Touzelet, S. (2015). *Tracer testing of the EGS site at Soultz-sous-Forêts (Alsace, France) between 2005 and 2013: PROCEEDINGS World Geothermal Congress 2015*. Melbourne.

Sanjuan, B., Pinault, J.-L., Rose, P., Gerard, A., and Brach, M. (2006). "Geochemical fluid characteristics and main achievements about tracer tests at Soultz-sous-Forêts (France)." In: *EHDRA Scientific Conference*.

Sausse, J. and Genter, A. (2005). "Types of permeable fractures in granite." In: *Geological Society, London, Special Publications* 240.1, pp. 1–14. ISSN: 0305-8719. DOI: 10.1144/GSL.SP.2005.240.01.01.

Sausse, J., Dezayes, C., Dorbath, L., Genter, A., and Place, J. (2010). "3D model of fracture zones at Soultz-sous-Forêts based on geological data, image logs, induced microseismicity and vertical seismic profiles." In: *Comptes Rendus Geoscience* 342.7-8, pp. 531–545. ISSN: 16310713. DOI: 10.1016/j.crte.2010.01.011.

Scheidegger, A. E. (1974). *The Physics of Flow Through Porous Media (3rd Edition)*. Heritage. Toronto and Berlin: University of Toronto Press and Walter de Gruyter GmbH. ISBN: 9781487583750.

Schill, E., Genter, A., Cuenot, N., and Kohl, T. (2017). "Hydraulic performance history at the Soultz EGS reservoirs from stimulation and long-term circulation tests." In: *Geothermics* 70, pp. 110–124. ISSN: 03756505. DOI: 10.1016/j.geothermics.2017.06.003.

Schindler, M. (2009). *Hydraulic Data recorded during the three circulations with down-hole pumps at soultz, Rapport Public GEIE n◦ RAP 71 000 Voo. GEIE, Soultz-sous-Forêts, France,*

Schindler, M., Baumgärtner, J., Gandy, T., Hauffe, P., Hettkamp, T., Menzel, H., Penzkofer, P., Teza, D., Tischner, T., and Wahl, G. (2010). *Successful Hydraulic Stimulation Techniques for Electric Power Production in the Upper Rhine Graben, Central Europe: PROCEEDINGS World Geothermal Congress 2010*. Bali, Indonesia.

Schmidt, R. B. (2019). "Alteration experiments on geothermal reservoir rocks of the Upper Rhine Graben." Dissertation. Karlsruhe: Karlsruhe Institute of Technology.

Schmidt, R. B., Bucher, K., Drüppel, K., and Stober, I. (2017). "Experimental interaction of hydrothermal Na-Cl solution with fracture surfaces of geothermal reservoir sandstone of the Upper Rhine Graben." In: *Applied Geochemistry* 81, pp. 36–52. ISSN: 08832927. DOI: 10.1016/j.apgeochem.2017.03.010.

Schmidt, R., Seithel, R., and Stober, I. (2016). *Verbundvorhaben „StörTief" - Die Rolle von tiefreichenden Störungszonen bei der geothermischen Energienutzung - Teilprojekt C Südwestdeutschland*.

Schmittbuhl, J., Steyer, A., Jouniaux, L., and Toussaint, R. (2008). "Fracture morphology and viscous transport." In: *International Journal of Rock Mechanics and Mining Sciences* 45.3, pp. 422–430. ISSN: 13651609. DOI: 10.1016/j.ijrmms.2007.07.007.

Schmittbuhl, J., Gentier, S., and Roux, S. (1993). "Field measurements of the roughness of fault surfaces." In: *Geophysical Research Letters* 20.8, pp. 639–641. ISSN: 00948276. DOI: 10.1029/93GL00170.

Schrauf, T. W. and Evans, D. D. (1986). "Laboratory Studies of Gas Flow Through a Single Natural Fracture." In: *Water Resources Research* 22.7, pp. 1038–1050. ISSN: 00431397. DOI: 10.1029/WR022i007p01038.

Schwartz, F. W., Smith, L., and Crowe, A. S. (1983). "A stochastic analysis of macroscopic dispersion in fractured media." In: *Water Resources Research* 19.5, pp. 1253–1265. ISSN: 00431397. DOI: 10.1029/WR019i005p01253.

Segura, J. M. and Carol, I. (2004). "On zero-thickness interface elements for diffusion problems." In: *International Journal for Numerical and Analytical Methods in Geomechanics* 28.9, pp. 947–962. ISSN: 0363-9061. DOI: 10.1002/nag.358.

Serdengecti, S. and Boozer, G. D. (1961). "The Effects of Strain Rate and Temperature on the Behavior of Rocks Subjected to Triaxial Compression." In: *Fourth Symposium on Rock Mechanics*. Pennsylvania, pp. 83–97.

Settari, A., Al-Ruwaili, K., and Sen, V. (2013). "Upscaling of Geomechanics in Heterogeneous Compacting Reservoirs." In: *SPE Reservoir Simulation Symposium*. Society of Petroleum Engineers. DOI: 10.2118/163641-MS.

Shook, G. M. (2003). "A simple, fast method of estimating fractured reservoir geometry from tracer tests." In: *GRC Transactions*, pp. 407–411.

Shook, G. M. (2005). *A systematic method for tracer test analysis: An example using Beoware tracer data: PROCEEDINGS Thirtieth Workshop on Geothermal Reservoir Engineering*. Stanford, California.

Siena, M., Iliev, O., Prill, T., Riva, M., and Guadagnini, A. (2019). "Identification of Channeling in Pore–Scale Flows." In: *Geophysical Research Letters* 46.6, pp. 3270–3278. ISSN: 00948276. DOI: 10.1029/2018GL081697.

Silliman, S. E. (1989). "An interpretation of the difference between aperture estimates derived from hydraulic and tracer tests in a single fracture." In: *Water Resources Research* 25.10, pp. 2275–2283. ISSN: 00431397. DOI: 10.1029/WR025i010p02275.

Smith, L. and Chapman, D. S. (1983). "On the thermal effects of groundwater flow: 1. Regional scale systems." In: *Journal of Geophysical Research* 88.B1, p. 593. ISSN: 0148-0227. DOI: 10.1029/JB088iB01p00593.

Snow, D. (1965). "A parallel plate model of fractured permeable media." Dissertation. Berkeley, California.

Sposito, G. (2008). *Scale dependence and scale invariance in hydrology*. Cambridge: Cambridge University Press. ISBN: 978-0521571258.

Stober, I. and Bucher, K. (2015). "Hydraulic and hydrochemical properties of deep sedimentary reservoirs of the Upper Rhine Graben, Europe." In: *Geofluids* 15.3, pp. 464–482. ISSN: 14688115. DOI: 10.1111/gfl.12122.

Stober, I. (2014). "Hydrochemical properties of deep carbonate aquifers in the SW German Molasse basin." In: *Geothermal Energy* 2.1, p. 108. ISSN: 2195-9706. DOI: 10.1186/s40517-014-0013-1.

Stober, I. and Bucher, K. (2007). "Hydraulic properties of the crystalline basement." In: *Hydrogeology Journal* 15.2, pp. 213–224. ISSN: 1431-2174. DOI: 10.1007/s10040-006-0094-4.

Stober, I. and Bucher, K. (2012). *Geothermie*. Springer Geology. Berlin, Heidelberg: Springer Berlin Heidelberg. ISBN: 9783642243301. DOI: 10.1007/978-3-642-24331-8.

Tang, Y. B., Li, M., Liu, X. J., Zhang, W. S., Qi, T., and Wei, M. J. (2019). "Pore-scale heterogeneity, flow channeling and permeability: Network simulation and comparison to experimental data." In: *Physica A: Statistical Mechanics and its Applications* 535, p. 122533. ISSN: 03784371. DOI: 10.1016/j.physa.2019.122533.

Taron, J., Elsworth, D., and Min, K.-B. (2009). "Numerical simulation of thermal-hydrologic-mechanical-chemical processes in deformable, fractured porous media." In: *International Journal of Rock Mechanics and Mining Sciences* 46.5, pp. 842–854. ISSN: 13651609. DOI: 10.1016/J.IJRMMS.2009.01.008.

Tembe, S., Lockner, D., and Wong, T.-f. (2009). "Constraints on the stress state of the San Andreas Fault with analysis based on core and cuttings from San Andreas Fault Observatory at Depth (SAFOD) drilling phases 1 and 2." In: *Journal of Geophysical Research* 114.B11. ISSN: 0148-0227. DOI: 10.1029/2008JB005883.

Terzaghi, K. (1943). *Theoretical Soil Mechanics*. Hoboken, NJ, USA: John Wiley & Sons, Inc. ISBN: 9780470172766. DOI: 10.1002/9780470172766.

Tollefson, J. (2018). "IPCC says limiting global warming to 1.5 °C will require drastic action." In: *Nature* 562.7726, pp. 172–173. DOI: 10.1038/d41586-018-06876-2.

Torabi, A. and Berg, S. S. (2011). "Scaling of fault attributes: A review." In: *Marine and Petroleum Geology* 28.8, pp. 1444–1460. ISSN: 02648172. DOI: 10.1016/j.marpetgeo.2011.04.003.

Tsang, C.-F. and Neretnieks, I. (1998). "Flow channeling in heterogeneous fractured rocks." In: *Reviews of Geophysics* 36.2, pp. 275–298. ISSN: 87551209. DOI: 10.1029/97RG03319.

Tsang, C.-F., Neretnieks, I., and Tsang, Y. (2015). "Hydrologic issues associated with nuclear waste repositories." In: *Water Resources Research* 51.9, pp. 6923–6972. ISSN: 00431397. DOI: 10.1002/2015WR017641.

Tsang, Y. W. (1992). "Usage of "Equivalent apertures" for rock fractures as derived from hydraulic and tracer tests." In: *Water Resources Research* 28.5, pp. 1451–1455. ISSN: 00431397. DOI: 10.1029/92WR00361.

Tsang, Y. W. and Tsang, C. F. (1987). "Channel model of flow through fractured media." In: *Water Resources Research* 23.3, pp. 467–479. ISSN: 00431397. DOI: 10.1029/WR023i003p00467.

Tsang, Y. W., Tsang, C. F., Neretnieks, I., and Moreno, L. (1988). "Flow and tracer transport in fractured media: A variable aperture channel model and its properties." In: *Water Resources Research* 24.12, pp. 2049–2060. ISSN: 00431397. DOI: 10.1029/WR024i012p02049.

Valley, B. and Evans, K. F. (2007). *Stress State At The Soultz-Sous-Forrêts To 5 km Depth From Wellbore Failure And Hydraulic Observations: PROCEEDINGS Thirdy-Second Workshop on Geothermal Reservoir Engineering*. Stanford, California.

Vallier, B., Magnenet, V., Schmittbuhl, J., and Fond, C. (2019). "Large scale hydrothermal circulation in the deep geothermal reservoir of Soultz-sous-Forêts (France)." In: *Geothermics* 78, pp. 154–169. ISSN: 03756505. DOI: 10.1016/j.geothermics.2018.12.002.

Vidal, J. and Genter, A. (2018). "Overview of naturally permeable fractured reservoirs in the central and southern Upper Rhine Graben: Insights from geothermal wells." In: *Geothermics* 74, pp. 57–73. ISSN: 03756505. DOI: 10.1016/j.geothermics.2018.02.003.

Vogt, C., Marquart, G., Kosack, C., Wolf, A., and Clauser, C. (2012). "Estimating the permeability distribution and its uncertainty at the EGS demonstration reservoir Soultz-sous-Forêts using the ensemble Kalman filter." In: *Water Resources Research* 48.8, p. 393. ISSN: 00431397. DOI: 10.1029/2011WR011673.

Vutukuri, V. S., Lama, R. D., and Saluja, S. S. (1974). *Handbook on mechanical properties of rocks: Testing Techniques and Results*. 1. Vol. 1, No. 1. Clausthal: Trans Tech Publications.

Wagner, W. and Pruß, A. (2002). "The IAPWS Formulation 1995 for the Thermodynamic Properties of Ordinary Water Substance for General and Scientific Use." In: *Journal of Physical and Chemical Reference Data* 31.2, pp. 387–535. ISSN: 0047-2689. DOI: 10.1063/1.1461829.

Walder, J. and Nur, A. (1984). "Porosity reduction and crustal pore pressure development." In: *Journal of Geophysical Research* 89.B13, pp. 11539–11548. ISSN: 0148-0227. DOI: 10.1029/JB089iB13p11539.

Wang, L., Cardenas, M. B., Slottke, D. T., Ketcham, R. A., and Sharp, J. M. (2015). "Modification of the Local Cubic Law of fracture flow for weak inertia, tortuosity, and roughness." In: *Water Resources Research* 51.4, pp. 2064–2080. ISSN: 00431397. DOI: 10.1002/2014WR015815.

Wang, Z., Xu, C., Dowd, P., Xiong, F., and Wang, H. (2020). "A Nonlinear Version of the Reynolds Equation for Flow in Rock Fractures With Complex Void Geometries." In: *Water Resources Research* 56.2. ISSN: 00431397. DOI: 10.1029/2019WR026149.

Watanabe, N., Ishibashi, T., and Tsuchiya, N. (2015). *Predicting the Channeling Flows through Fractures at Various Scales: PROCEEDINGS World Geothermal Congress 2015*. Melbourne.

Watanabe, N., Blöcher, G., Cacace, M., Held, S., and Kohl, T. (2017). *Geoenergy Modeling III*. Cham: Springer International Publishing. ISBN: 978-3-319-46579-1. DOI: 10.1007/978-3-319-46581-4.

Watanabe, N. and Kolditz, O. (2015). "Numerical stability analysis of two–dimensional solute transport along a discrete fracture in a porous rock matrix." In: *Water Resources Research* 51.7, pp. 5855–5868. ISSN: 00431397. DOI: 10.1002/2015WR017164.

Whitaker, S. (1986). "Flow in porous media I: A theoretical derivation of Darcy's law." In: *Transport in Porous Media* 1.1, pp. 3–25. ISSN: 0169-3913. DOI: 10.1007/BF01036523.

Willis-Richards, J., Watanabe, K., and Takahashi, H. (1996). "Progress toward a stochastic rock mechanics model of engineered geothermal systems." In: *Journal of Geophysical Research* 101.B8, pp. 17481–17496. ISSN: 0148-0227. DOI: 10.1029/96JB00882.

Witherspoon, P. A., Wang, J. S. Y., Iwai, K., and Gale, J. E. (1980). "Validity of Cubic Law for fluid flow in a deformable rock fracture." In: *Water Resources Research* 16.6, pp. 1016–1024. ISSN: 00431397. DOI: 10.1029/WR016i006p01016.

Wong, T.-f. and Baud, P. (2012). "The brittle-ductile transition in porous rock: A review." In: *Journal of Structural Geology* 44, pp. 25–53. ISSN: 01918141. DOI: 10.1016/j.jsg.2012.07.010.

Wong, T.-f., David, C., and Zhu, W. (1997). "The transition from brittle faulting to cataclastic flow in porous sandstones: Mechanical deformation." In: *Journal of Geophysical Research: Solid Earth* 102.B2, pp. 3009–3025. ISSN: 21699313. DOI: 10.1029/96JB03281.

Zang, A., Oye, V., Jousset, P., Deichmann, N., Gritto, R., McGarr, A., Majer, E., and Bruhn, D. (2014). "Analysis of induced seismicity in geothermal reservoirs – An overview." In: *Geothermics* 52, pp. 6–21. ISSN: 03756505. DOI: 10.1016/j.geothermics.2014.06.005.

Zhang, J., Wong, T.-f., and Davis, D. M. (1990). "Micromechanics of pressure-induced grain crushing in porous rocks." In: *Journal of Geophysical Research* 95.B1, p. 341. ISSN: 0148-0227. DOI: 10.1029/JB095iB01p00341.

Zhao, Z., Jing, L., and Neretnieks, I. (2010). "Evaluation of hydrodynamic dispersion parameters in fractured rocks." In: *Journal of Rock Mechanics and Geotechnical Engineering* 2.3. ISSN: 16747755. DOI: 10.3724/SP.J.1235.2010.00243.

Ziegler, P. A. and Dèzes, P. (2005). "Evolution of the lithosphere in the area of the Rhine Rift System." In: *International Journal of Earth Sciences* 94.4, pp. 594–614. ISSN: 1437-3254. DOI: 10.1007/s00531-005-0474-3.

Ziegler, P. A., Schumacher, M. E., Dèzes, P., van Wees, J.-D., and Cloetingh, S. (2004). "Post-Variscan evolution of the lithosphere in the Rhine Graben area: Constraints from subsidence modelling." In: *Geological Society, London, Special Publications* 223.1, pp. 289–317. ISSN: 0305-8719. DOI: 10.1144/GSL.SP.2004.223.01.13.

Zimmerman, R. W. (2000). "Coupling in poroelasticity and thermoelasticity." In: *International Journal of Rock Mechanics and Mining Sciences* 37.1-2, pp. 79–87. ISSN: 13651609. DOI: 10.1016/S1365-1609(99)00094-5.

Zimmerman, R. W., Al-Yaarubi, A., Pain, C. C., and Grattoni, C. A. (2004). "Non-linear regimes of fluid flow in rock fractures." In: *International Journal of Rock Mechanics and Mining Sciences* 41, pp. 163–169. ISSN: 13651609. DOI: 10.1016/j.ijrmms.2004.03.036.

Zimmerman, R. W. and Bodvarsson, G. (1996). "Hydraulic conductivity of rock fractures." In: *Transport in Porous Media* 23.1. ISSN: 0169-3913. DOI: 10.1007/BF00145263.

Zoback, M. D. (2011). *Reservoir geomechanics*. 5. print. Cambridge: Cambridge Univ. Press. ISBN: 978-0521146197.

Zou, L., Jing, L., and Cvetkovic, V. (2017). "Modeling of Solute Transport in a 3D Rough-Walled Fracture–Matrix System." In: *Transport in Porous Media* 116.3, pp. 1005–1029. ISSN: 0169-3913. DOI: 10.1007/s11242-016-0810-z.

DECLARATION OF AUTHORSHIP

CHAPTER 4: STOCHASTIC 3D NAVIER-STOKES FLOW IN SELF-AFFINE FRACTURE GEOMETRIES CONTROLLED BY ANISOTROPY AND CHANNELING

Egert, R., Nitschke, F., Gholami Korzani, M. and Kohl, T. (2021). "Stochastic 3D Navier-Stokes Flow in Self-Affine Fracture Geometries Controlled by Anisotropy and Channeling." In: *Geophysical Research Letters* 48.9. issn: 00948276. doi: 10.1029/2020GL092138.

This study was conducted within the Helmholtz topic 'Geothermal Energy Systems' in the program 'Renewable Energies' and was supported by Energie Baden-Wuerttemberg (EnBW), Germany.

In this study, I developed the numerical code for solving the local cubic law and using spatially varying apertures within the TIGER application, and linked TIGER to the Navier-Stokes module of MOOSE. The rough surfaces were generated using the Safft software. I developed an Matlab algorithm to shear two opposing rough surfaces and transfer the resulting fracture geometry to 3D finite element meshes and 3D printable STL-files. In addition, the algorithm allows the calculation of local vertical and effective apertures to transfer the geometry to a 2D FE mesh. I have created concept for numerical modeling. I created the post-processing workflow to identify spatial differences between the flow laws. I visualized and interpreted the numerical results. Finally, I wrote the manuscript.

CHAPTER 5: SPATIAL CHARACTERIZATION OF CHANNELING PROCESSES IN SELF-AFFINE ROUGH-WALLED FRACTURES IN THE TRANSITION TO A NONLINEAR FLOW REGIME

Egert, R., Gholami Korzani, M., Nitschke, F., and Kohl, T. (2021). "Spatial characterization of channeling processes in self-affine rough-walled fractures in the transition to a nonlinear flow regime." – In preparation for submission.

This study was conducted within the Helmholtz topic 'Geothermal Energy Systems' in the program 'Renewable Energies' and and was supported by Energie Baden-Wuerttemberg (EnBW), Germany.

This study is based on the previously described workflow for generating 3D numerical models of rough fracture geometries. In addition, I developed a universally applicable Matlab workflow to identify and quantify the channeling processes within an arbitrary flow structure (e.g. single fracture or fracture network) on a stochastic basis. I analyzed and visualized the results. I discussed the results in terms of large-scale reservoir flow. I prepared the manuscript.

CHAPTER 6: TRIAXIAL TESTING AND HYDRAULIC-MECHANICAL MODELING OF SANDSTONE RESERVOIR ROCK IN THE UPPER RHINE GRABEN

Egert, R., Seithel, R., Kohl, T., and Stober, I. (2018). "Triaxial testing and hydraulic–mechanical modeling of sandstone reservoir rock in the Upper Rhine Graben." In: *Geothermal Energy* 6.1. issn: 2195-9706. doi: 10.1186/s40517-018-0109-0.

This research has been funded by the project 'Geofaces-SD' of the German Federal Ministry for Economic Affairs and Energy (BMWi, no. 0324025C), implemented by the Project Management Jülich (PtJ).

In this study, I did the conceptual design of the entire manuscript. The laboratory experiments were performed by Robin Seithel. I selected and analyzed the raw data from the laboratory experiments (triaxial and permeameter measurements) and created the workflow for the numerical modeling. I evaluated and interpreted all data, as well as visualized them. I discussed the linkage of experimental and numerical data. Finally, I wrote the manuscript.

CHAPTER 7: IMPLICATIONS ON LARGE-SCALE FLOW OF THE FRACTURED EGS RESERVOIR SOULTZ INFERRED FROM HYDRAULIC DATA AND TRACER EXPERIMENTS

Egert, R., Korzani, M. G., Held, S., and Kohl, T. (2020). "Implications on large-scale flow of the fractured EGS reservoir Soultz inferred from hydraulic data and tracer experiments." In: *Geothermics* 84. issn: 03756505. doi: 10.1016/j.geothermics.2019.101749.

This research has been funded by the project 'Geofaces-SD' of the German Federal Ministry for Economic Affairs and Energy (BMWi, no. 0324025C), implemented by the Project Management Jülich (PtJ).

In this study, I reanalyzed the raw data from the various well logs. The borehole logs are courtesy of GEIE Soultz and BRGM. Sebastian Held created the initial structural model of the Soultz reservoir, which I modified and significantly extended. I incorporated all numerical equations needed to simulate non-reactive solute transport and temporally varying boundary conditions into the TIGER application. I conducted the simulations. I prepared and presented the modeling results and correlated them with the experimental data. Finally, I wrote the manuscript.

CHAPTER 8: THERMO-HYDRAULIC MODELING OF AN ENHANCED GEOTHERMAL SYSTEM IN THE UPPER RHINE GRABEN USING MOOSE/TIGER

Egert, R., Gholami Korzani, M., Held, S., and Kohl, T. (2021). "Thermo-hydraulic Modeling of an Enhanced Geothermal System in the Upper Rhine Graben using MOOSE/TIGER" - *PROCEEDINGS World Geothermal Congress 2020+1*. Reykjavik.

This research has been partly funded by the project 'Geofaces-SD' of the German

Federal Ministry for Economic Affairs and Energy (BMWi, no. 0324025C), implemented by the Project Management Jülich (PtJ). This study was conducted within the Helmholtz topic 'Geothermal Energy Systems' in the program 'Renewable Energies' and was supported by Energie Baden-Wuerttemberg (EnBW), Germany.

This study is based on the numerical and hydraulic model of Soultz reservoir that I described in the previous chapter. This has been extended to include the heat transport within. I collected the material parameters. I wrote the numerical code for the simulations and conducted them. I prepared and wrote the manuscript.

PUBLICATIONS

PUBLICATIONS IN PEER-REVIEWED JOURNALS

Egert, R., Gholami Korzani, M., Held, S., and Kohl, T. (2020). "Implications on large-scale flow of the fractured EGS reservoir Soultz inferred from hydraulic data and tracer experiments." In: *Geothermics* 84, p. 101749. ISSN: 03756505. DOI: 10.1016/j.geothermics.2019.101749.

Egert, R., Gholami Korzani, M., Held, S., and Kohl, T. (2021a). "Thermo-hydraulic Modeling of an Enhanced Geothermal System in the Upper Rhine Graben using MOOSE/TIGER." In: *PROCEEDINGS World Geothermal Congress 2020+1*.

Egert, R., Nitschke, F., Gholami Korzani, M., and Kohl, T. (2021b). "Stochastic 3D Navier–Stokes Flow in Self–Affine Fracture Geometries Controlled by Anisotropy and Channeling." In: *Geophysical Research Letters* 48.9. ISSN: 00948276. DOI: 10.1029/2020GL092138.

Egert, R., Seithel, R., Kohl, T., and Stober, I. (2018). "Triaxial testing and hydraulic–mechanical modeling of sandstone reservoir rock in the Upper Rhine Graben." In: *Geothermal Energy* 6.1. ISSN: 2195-9706. DOI: 10.1186/s40517-018-0109-0.

Stricker, K., Grimmer, J. C., Egert, R., Bremer, J., Gholami Korzani, M., Schill, E., and Kohl, T. (2020). "The Potential of Depleted Oil Reservoirs for High-Temperature Storage Systems." In: *Energies* 13.24, p. 6510. ISSN: 1996-1073. DOI: 10.3390/en13246510.

PRESENTATIONS WITH ABSTRACTS

Egert, R., Gholami Korzani, M., Held, S., and Kohl, T. (2021). *Thermo-hydraulic Modeling of an Enhanced Geothermal System in the Upper Rhine Graben using MOOSE/TIGER: Oral presentation*. World Geothermal Congress, Reykjavik.

Egert, R., Gholami Korzani, M., Held, S., Kohl, T., and Stober, I. (2018a). *Hydrothermal modeling of a deep fault-related fracture system in the Upper Rhine Graben (URG). Poster presentation*. The Geological Society of America 130th Annual Meeting, Indianapolis. DOI: 10.1130/abs/2018AM-316951.

Egert, R., Gholami Korzani, M., Held, S., Stober, I., and Kohl, T. (2018b). *Thermo-hydraulic modeling of a deep fault-related fracture system in the Upper Rhine Graben using MOOSE/TIGER. Poster presentation*. 6th European Geothermal Workshop, Straßburg.

Egert, R., Nitschke, F., Gholami Korzani, M., and Kohl, T. (2019). *Linear vs. Nonlinear flow laws in sheared and rough self-affine fractures. Poster presentation*. 7th European Geothermal Workshop, Karlsruhe.

Egert, R., Nitschke, F., Gholami Korzani, M., and Kohl, T. (2020a). *Statistische Evaluierung von nichtlinearen Effekten auf rauen und gescherten Kluftoberflächen. Oral presentation*. Der digitale Geothermiekongress, Essen.

Egert, R., Nitschke, F., Gholami Korzani, M., and Kohl, T. (2020b). *Stochastic evaluation of the flow regime on rough and sheared fractures: Oral presentation*. 8th European Geothermal Workshop, Straßburg.

Egert, R., Seithel, R., Peters, M., and Stober, I. (2017a). *Numerical simulation and evaluation of triaxial tests of reservoir rocks of the Upper Rhine Graben: Poster presentation*. 5th European Geothermal Workshop, Karlsruhe.

Egert, R., Seithel, R., Peters, M., and Stober, I. (2017b). *Numerische Simulation von Triaxialversuchen an Reservoirgesteinen des Oberrheingrabens: Oral presentation*. Der Geothermiekongress, München.

Kohl, T., Egert, R., and Nitschke, F. (2020). *Flow regime in self-affine fractures inferred from field observations and statistical analysis: Oral presentation*. GSA 2020 Connects Online. DOI: 10.1130/abs/2020AM-358827.

Nitschke, F., Egert, R., Marchand, S., and Kohl, T. (2020). *Numerische und experimentelle Untersuchungen der Hydraulik auf gescherten rauen Klüften bei hohen Geothermie-typischen Fließraten: Oral presentation*. Der digitale Geothermiekongress, Essen.

ACKNOWLEDGMENTS

So many different people have supported me during my PhD and have contributed to this work. I would like to say thank you to all of them. Furthermore, I would like to explicitly mention some people who have a major contribution to this thesis.

First of all, I would like to thank my supervisor Thomas Kohl for providing me the opportunity to work on this subject. Thank you for your support during the creation of this thesis. He has played a major role in my personal and scientific development and has always supported me even in complicated times.

Thank you to Florian Amann, who gratefully agreed to be the co-supervisor of this thesis.

I would like to thank Ingrid Stober for giving me the opportunity to start my PhD within the project 'GeoFaces-SD' and introducing me to the fundamentals of scientific work.

Another big thank you goes to the entire team of the Geothermal Working Group. Your working atmosphere has always motivated me even in difficult times of my work and influenced the progress through your fruitful (more or less) scientific discussions. However, a few people should also be given extra thanks here.

Thank you, Maziar for your great support on all kinds of numerical issues and the debates resulting from them.

Many thanks also to Basti, Fabian and Roman for your contribution to solve innumerable small and big challenges. I could always drop by for a fast coffee and a brief question.

The rest of the coffee group also deserves a big thank you for the almost daily discussions about science, but also about everyday life.

A big thank you also to Silke, who always helped me with administrative questions and the pitfalls of the KIT bureaucracy.

I would like to thank my parents for their unconditional support all the journey.

Last but not least, I would like to thank my wife, Bianca, for being there for me the whole time and motivating me so much throughout my PhD.